POLARIZATION FIELD ENHANCED TRANSPORT IN GALLIUM NITRIDE HETEROSTRUCTURES FOR ENERGY HARVESTING AND SENSING

A DISSERTATION
SUBMITTED TO THE DEPARTMENT OF MECHANICAL ENGINEERING
AND THE COMMITTEE ON GRADUATE STUDIES
OF STANFORD UNIVERSITY
IN PARTIAL FULFILLMENT OF THE REQUIREMENTS
FOR THE DEGREE OF
DOCTOR OF PHILOSOPHY

Ananth Saran Yalamarthy

March 2019

© 2019 by Ananth Saran Yalamarthy. All Rights Reserved.
Re-distributed by Stanford University under license with the author.

This work is licensed under a Creative Commons Attribution-Noncommercial 3.0 United States License.
http://creativecommons.org/licenses/by-nc/3.0/us/

This dissertation is online at: http://purl.stanford.edu/hf621yn0502

I certify that I have read this dissertation and that, in my opinion, it is fully adequate in scope and quality as a dissertation for the degree of Doctor of Philosophy.

Debbie Senesky, Primary Adviser

I certify that I have read this dissertation and that, in my opinion, it is fully adequate in scope and quality as a dissertation for the degree of Doctor of Philosophy.

Kenneth Goodson, Co-Adviser

I certify that I have read this dissertation and that, in my opinion, it is fully adequate in scope and quality as a dissertation for the degree of Doctor of Philosophy.

Eric Pop

Approved for the Stanford University Committee on Graduate Studies.

Patricia J. Gumport, Vice Provost for Graduate Education

This signature page was generated electronically upon submission of this dissertation in electronic format. An original signed hard copy of the signature page is on file in University Archives.

Abstract

Over the past decade, we have witnessed a renaissance in power and RF electronics – enabled by breakthroughs in wide-band gap semiconductors made using III-nitride materials. Yet, an exciting but emerging application of these materials is their use in extreme temperature environments such as oil/gas, combustion and space, where traditional silicon electronics do not operate. In this thesis, I discuss how polarization fields in gallium nitride on silicon (GaN-on-Si) can be used to make thermoelectric energy harvesting and sensing devices to achieve this ambitious goal of "extreme environment" operation. In the first part of this thesis, I discuss measurements of the thermoelectric properties of the aluminum gallium nitride/gallium nitride (AlGaN/GaN) two-dimensional electron gas (2DEG) from room temperature to 300°C. Our experiments demonstrate state-of-the-art thermoelectric power factors (4-7 $\mathrm{mW{\cdot}m^{-1}K^{-2}}$ at room temperature) and thermoelectric figures of merit ∼4x better than doped III-nitride materials. These properties can enable a monolithic GaN-on-Si micro-thermoelectric generator with a power density of ∼1 $\mathrm{mW{\cdot}cm^{-2}}$, which can be used to power an extreme environment IoT node. I follow this with a brief digression on the thermoelectric properties of AlGaN/GaN films on a pyramidal Si substrate, a strategy that can increase power density in micro-thermoelectric generators.

Switching gears, I next discuss how the transfer of momentum from lattice phonons to electrons, a phenomenon called phonon drag, can be used to boost the low temperature thermoelectric performance in the AlGaN/GaN 2DEG. The measurements of the phonon drag Seebeck coefficient are conducted by varying the thickness of the underlying GaN layer. For large GaN thickness (∼1.2 µm), we find that ∼32% of Seebeck coefficient at room temperature can be attributed to phonon drag. At 50 K, the drag component increases significantly to ∼88%.

In the last part of my thesis, I discuss how manipulation of the polarization fields in the AlGaN/GaN 2DEG can be used for high-performance sensing applications. I first discuss a model for studying electronic transport in AlGaN/GaN transistors under small applied strains, which may find

use in pressure sensing and device packaging. Then, I present measurements of a novel ultraviolet (UV) photodetector employing the 2DEG formed at the AlGaN/GaN interface as an interdigitated transducer. This photodetector exhibits a record high normalized photocurrent-to-dark current ratio ($\sim 6 \times 10^{14}$), which enables highly sensitive detection of UV optical stimuli. Overall, the techniques explored in this thesis are an important step towards the maturation of the AlGaN/GaN-on-Si platform as an extreme environment IoT node.

Acknowledgments

A PhD thesis is, in many ways, a team effort. First and foremost, I would like to thank my advisor, Prof. Debbie G. Senesky, for allowing me to pursue my interests and decide my own path. I have learned a lot about microfabrication, electronic devices and MEMS from her. She has been very supportive during my stay at Stanford and was very influential in fostering the positive atmosphere I had at XLab. I would like to thank my labmates, who were always ready to help and were above all, really fun to work with. Special thanks to Ateeq, Karen, Cailtin, and Hongyun, who gave me plently of valuable feedback when I was new to the lab. One of the perks of being an early Ph.D. student in the XLab was the opportunity to interact and work closely with most of the other members in the lab. To this regard, I would like to thank Hannah, Peter, Saleh, Sambhav, Minmin and Ruth. I would also like to thank some of the newer students, especially Max, Savannah and Anand for fruitful discussions. The social atmosphere in XLab is one of the most exciting parts of being in this lab. Perhaps the biggest highlight was our trip to Japan, where I was accompanied by Tom and Ruiqi, who were loads of fun. Another unique aspect of XLab was the influx of REUs in the summer, where I gained valuable mentoring and teaching experience. Laura, Alex, and Lige, you have all been wonderful to work with and I hope our interactions helped shape your early career.

My thesis would not have been possible without help from several other research groups on campus. Firstly, Prof. Eric Pop and his group were like a second family to me. Miguel, who was then a postdoc in Eric's group and is now faculty at Twente University in the Netherlands, worked closely with me on many aspects of this thesis. My knowledge on experimental techniques for thermal characterization and general life advice are due to him, and I greatly value his time and effort. I would also like to thank Michelle and Victoria, who were part of the NSF POETS collaboration, and were great to work with. I would also like to thank Prof. Kenneth E. Goodson for agreeing to be my co-advisor. I have benefited greatly from his class on microscale heat conduction and from close interactions with many people in his research group, particularly Tanya Liu and Aditya Sood. All

the fabrication work in this thesis was done in the Stanford Nanofabrication Facility (SNF). This thesis would not have been possible without support from SNF staff, particularly Dr. Xiaoqing Xu who oversaw all the MOCVD growth.

Lastly, outside of research, I would like to acknowledge many wonderful moments with my friends. Amongst these, some of my old undergraduate friends, particularly Vivek, Nithin, Nitin, Varsha, Sneha, Athreya, Eddy, and Nandita have always been great fun to hangout with. I would also like to thank Anmol, Arushi, Nandita, and Pravallika for all the good times we spent together - I hope we will continue to have fun together in the years to come.

Finally, I would like to thank my family and my cousins in the Bay area, who have been a great source of stress relief (especially the good food!) in the weekends. My mom and dad have always been very supportive of my education from the earliest days and are the reason why I came to Stanford. My brother has been a constant moral support for me throughout and I hope he will pursue a graduate career as well. This thesis is dedicated to my family.

Contents

List of Tables

List of Figures

Chapter 1

Introduction

1.1 Electronics for Extreme Temperature Environments

Semiconductor devices based on silicon (Si) are the focal point of today's information revolution. One of the major themes of this revolution is the integration of billions of cheap, low cost sensor nodes with renewable power sources, which, coupled with advancements in artificial intelligence, enable automation at an unprecedented scale. This phenomenon is often referred to as the Internet of Things (IIoT), and is expected to grow to ~91.4 billion US dollars by 2023 [1]. Most IIoT is focused on applications within silicon's mil-spec temperature range (-55°C to 125°C). However, many applications, which function in "extreme environments" as depicted in Figure 1.1, could benefit from low-power IoT outside this temperature range. Although extreme environment could refer to me-

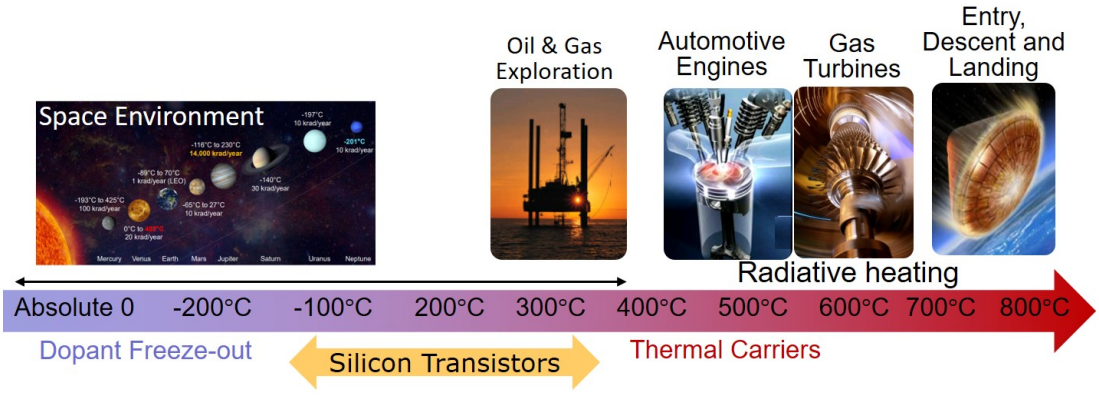

Figure 1.1: Applications for extreme temperature electronics.

chanical forces, pressures, radiation levels, or chemical environments, in this thesis, we are primarily concerned with temperature. For example, combustion engines in aircraft systems require sensors which measure temperature and pressure above 350°C [2]. Automobiles often require chemical/gas sensors at the exhaust, which should withstand temperatures from 350°C to 600°C [3, 4]. Other examples of high-temperature applications include furnaces, geothermal [3], oil and gas [3], as well as atmospheric re-entry during planetary space missions. On the other extreme, cryogenic electronics are required for space applications [5], highly-sensitive detectors and sensors [6], and remote sensing. In this thesis, we are largely concerned with cryogenic electronics above the liquid nitrogen temperature (77 K).

Modern consumer electronics used today incorporate many sensors, microprocessors and communication techonologies (such as wireless chipsets). However, in extreme environment, no such system exists till date, with the only existing technology being a few simple sensing devices [7]. In addition to the lack of microprocessors, traditional power sources, such as batteries, do not exist at high temperatures (above 250 °C) [8]. Furthermore, most devices used in extreme high temperature environments today require some form of active cooling (often bulky) to keep device temperatures low, however, this is not challenging when the ambient itself is an extreme environment (such as downhole oil/gas applications). In this scenario, it is necessary to overcome fundamental material limitations to enable extreme environment electronic systems.

An electronic material's fundamental limitation to work at high temperature is related to its temperature-dependent intrinsic carrier concentration, which is a function of its bandgap (E_G). The intrinsic carrier concentration can be expressed as [9]:

$$n_i = \sqrt{N_c N_v} e^{-\frac{E_G}{k_B T}} \tag{1.1}$$

where N_c and N_v are the conduction and valence band density-of-states, k_B is the Boltzmann constant and T is the temperature. The temperature dependent intrinsic carrier concentration for Si is plotted in Figure 1.2 up to 800°C. Traditionally, silicon devices are doped in the range of 10^{14} to 10^{19} cm^{-3}. It can be seen that n_i for Si reaches $\sim 10^{15}$ cm^{-3} at a temperature of 300°C, at which point, it is comparable to the doped charge concentration, and starts to adversely impact device operation. The plot also includes the intrinsic carrier concentration for gallium nitride (GaN), a wide-bandgap semiconductor (E_G of 3.4 eV), where the intrinsic carrier concentration ($\sim 10^5$ cm^{-3} at 300°C) does not limit operation up to temperatures as high as 1000°C. This suggests that a wide-bandgap material, such as GaN, when mature enough to make microprocessors, sensing technologies,

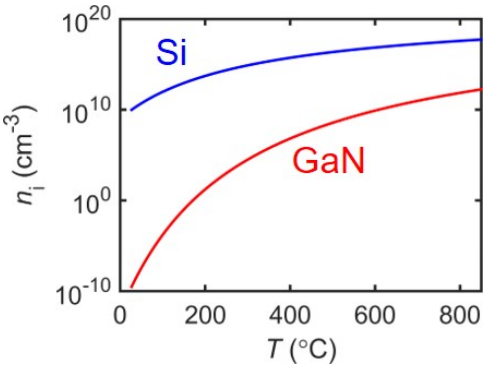

Figure 1.2: Temperature-dependent intrinsic carrier concentration in Si and GaN.

and dedicated power delivery, could be used to realize an extreme environment electronic platform for a range of industrial and space applications.

1.2 Gallium Nitride as an Extreme Environment Electronic Material

Gallium nitride (GaN) is a wide-bandgap (∼3.4 eV) semiconductor with a direct bandgap, and has a Wurtzite crystal structure [10]. It is part of the larger family of III-nitride devices, which also include aluminum nitride (AlN, $E_G \sim 6.2$ eV) and indium nitride (InN, $E_G \sim 1.97$ eV) [10]. GaN, AlN and InN can be alloyed to form semiconductors with tunable direct bandgap. GaN first emerged as an important semiconductor in the late 1980s and the early 1990s due to breakthroughs in the growth of InGaN on sapphire, which eventually lead to the commercialization of the blue light-emitting diode (LED). Due to its opto-electronic properties, InGaN is today (early 2019) the second most important semiconductor after Si [7]. In a parallel line of work, the growth of high quality GaN on sapphire led to the demonstration of the AlGaN/GaN high electron mobility transistor (HEMT) in 1993 [11]. In such a transistor, the AlGaN layer is very thin (∼20-30 nm) and a two-dimensional sheet of electrons (2DEG) at the AlGaN/GaN interface forms the channel for the transistor. The high mobility of the electrons in the 2DEG (∼2000 cm^2·V^{-1}s^{-1} [7]), coupled with the high breakdown field of GaN (∼5 MV·cm^{-1} [7]) paved the way for the development of high-power and RF electronics. Today, high-power and RF HEMTs have been commercialized. Further, GaN devices are now grown on 8" Si substrates which enables low cost [7].

Table 1.1: Properties of Si and GaN.

Parameter	Si	GaN
Bandgap (E_G, eV)	1.1 [17]	3.4 [17]
Melting Point (°C)	1415 [17]	2500 [17]
Electrical Failure (°C)	300 [3]	1000 [12]
Yield strength (MPa)	∼10 (at 600°C) [18]	∼200 (at 600°C) [18]
Tensile strength (GPa)	∼7 [19]	∼10 [20]
Atomic bond energy (eV)	2.34 [15]	8.92 [15]

Gallium nitride is also very suitable for harsh environment applications, because of its wide-bandgap, high melting point, high radiation hardness, and most notably high temperature electronic operation (table 1.1). In particular, InAlN/GaN HEMTs with a 2DEG at the InAlN/GaN interface have shown operation up to 1000°C [12], while AlGaN/GaN HEMTs have shown operation up to 600°C [13]. For comparison, the best silicon devices, which are based on the silicon-on-insulator (SOI) technology, have demonstrated operation up to 300°C. The mechanical properties of GaN are also favorable in comparison to silicon, which leads to reliable MEMS devices. For example, the yield strength of GaN, at 200 MPa, is about 20 times the value of Si (table 1.1). Finally, GaN (and other III-nitride materials) are robust to high levels of radiation exposure and have a high atomic bond energy [14, 15, 16], which supports their use in the space environment.

1.3 AlGaN/GaN-on-Si Platform

When a heterostructure of AlGaN/GaN is grown on top of Si, it becomes a versatile platform for extreme environment IoT. In particular, growth on top of Si allows the fabrication of microelectromechanical (MEMS) devices, by releasing the silicon via etching. Both topside etching (using a vapor phase XeF_2 etch) and backside etching (using a deep reactive ion etch) have been demonstrated. Some important sensing devices that take advantage of the released substrate include pressure sensors [21], MEMS resonators [22], micro-hotplates [23], fast recovery UV photodetectors [23]. Other sensors, such as chemical sensors [24, 25, 26] and UV photodetectors [27, 28] do not need a released substrate. In a parallel line of work, researchers have been actively trying to build integrated circuits using AlGaN/GaN transistors, with basic circuits (such as an inverter) demonstrated up to 375°C [29]. Instead of complementary p-type and n-type transistors, these circuits use enhancement mode (E-mode) and depletion mode (D-mode) HEMTs as the basic building blocks [29]. This constraint is due to the poor hole mobility in GaN (below ∼30 $cm^2 \cdot V^{-1} s^{-1}$ at room temperature [30, 31]).

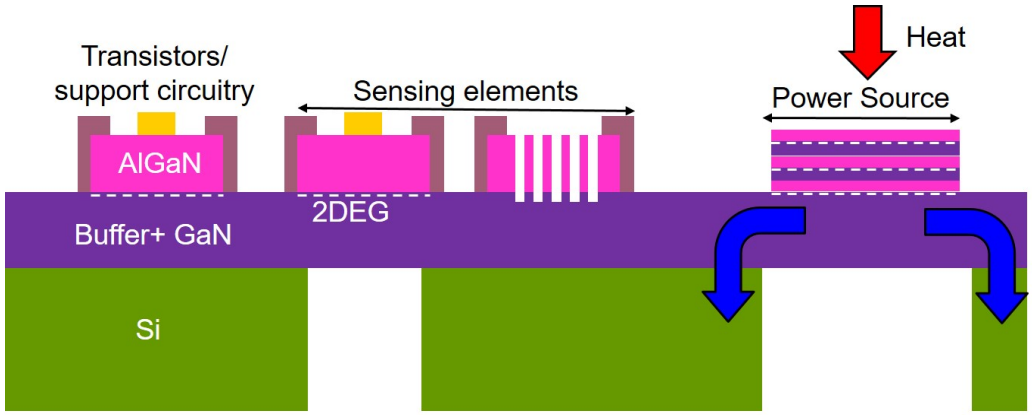

Figure 1.3: Monolithic integration of electronics, sensors and power sources on an AlGaN/GaN-on-Si platform.

Finally, GaN transistors can also be used as the building blocks in RF and power conversion circuits. Although further maturation of sensing technology is required, in particular, the high temperature operation capability, current progress in sensing, power delivery, and wireless communication suggest that a monolithic IoT platform using GaN-on-Si is feasible. An example of such a platform is depicted in Figure 1.3.

1.3.1 Energy Harvesting

Beyond the development of electronics for sensing, processing, and transmitting information, one of the key challenges with extreme environments is power delivery. Current battery technology is not functional above a temperature of 250°C. Although cabled wiring from a different location is possible, this is very challenging if the ambient itself is an extreme environment. Further, wiring would increase the footprint of the system, and make system integration complex. In this scenario, the only viable option to have a local energy harvesting module integrated with the electronics system, as depicted in Figure 1.3. The total power requirement for a wireless sensor node is on the order of a few µW to mW [32], which is sufficiently low enough to be met by an on-chip energy harvesting module. A prototypical IoT node which uses energy harvesting is depicted in Figure 1.4. Many energy harvesting mechanisms exist, such as thermoelectric harvesters, solar cells, vibration, thermionic emission, and alpha/beta voltaic devices [33].

Although solar cells are traditionally used in energy harvesting systems, they are not suitable for high temperatures because of the large decrease in open circuit voltage at high temperatures.

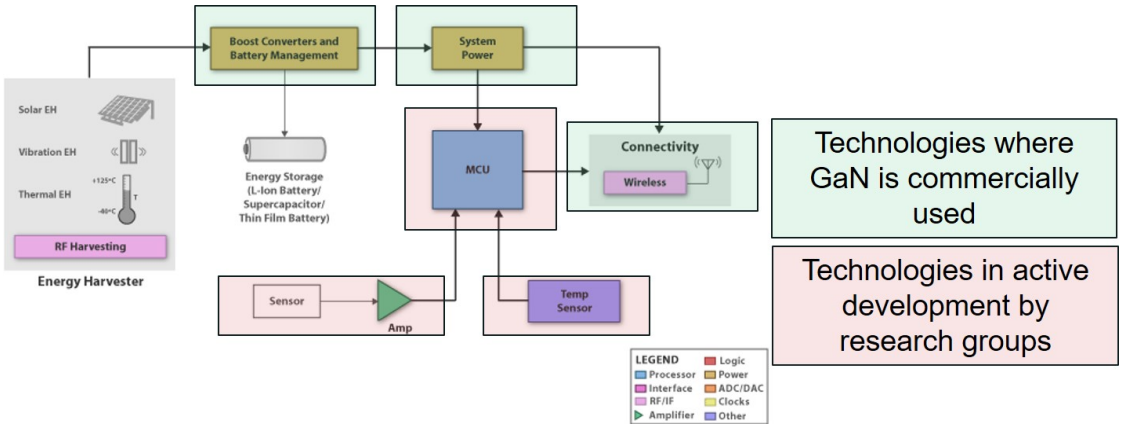

Figure 1.4: A prototypical energy harvesting system. Original image credit: Texas Instruments.

In order to use a solar cell for terrestrial energy harvesting, the bandgap needs to be small (∼1 to ∼1.7 eV). A solar cell that is 25% efficient at room temperature with a bandgap of 1.4 eV (made of InGaP) will have a theoretical efficiency 5% at a temperature of 600°C [34]. Practically, the efficiency drops much faster, and falls below 5% at 300-400°C [34]. On the other hand, thermionic energy harvesters are suitable for extreme environment energy harvesting, but need very high temperatures (>1000°C) for operation [35], making their usage challenging. Most alpha/betavoltaic sources suffer from a large decrease in efficiency due to a drop in open circuit voltage at high temperatures, similar to solar cells [33].

Specifically, most high-temperature energy harvesting solutions use thermoelectric devices [36, 37], which become more efficient at high temperatures if they have a wide-bandgap [10]. One such commercially available device is a thermoelectric powered temperature sensor with a RF transmitter from Micropelt, which operates up to 100°C. In this thesis, we focus on the use of the AlGaN/GaN-on-Si platform for designing an integrated thermoelectric energy harvester for a range of extreme temperature environments, as depicted in Figure 1.1. A power output of 10-100 µW is sufficient power for typical sensing elements (Figure 1.5, but not sufficient to make an IoT node. As a representative target, an output power of a few mW on a footprint of 1 cm × 1 cm should satisfy the requirements for sensing and wireless transmission, as can be seen from Figure 1.5.

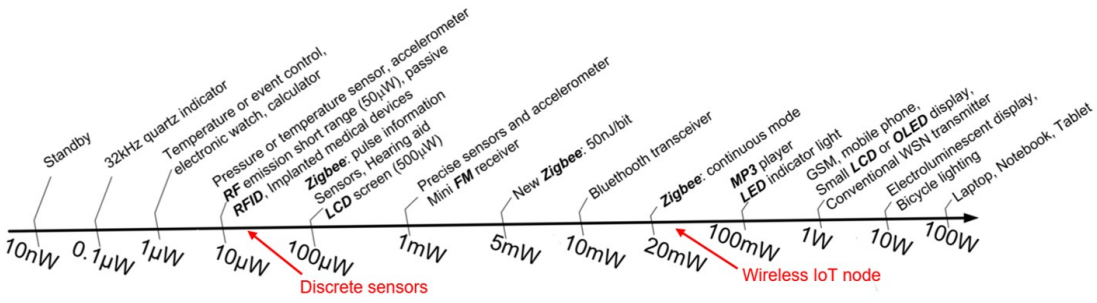

Figure 1.5: Power consumption requirements for a myriad of electronic devices, from sensors, to wireless nodes, to compact systems. Adapted from [38].

1.3.2 Thermoeletric Energy Harvesting

Thermoelectrics are solid state energy conversion devices which generate electrical power from a temperature gradient (Seebeck effect), and vice-versa, generate a temperature gradient from electrical power (Peltier effect). These devices have the advantage of no moving parts, no maintenance, and high reliability, which makes them a suitable power source in harsh environments. These devices are currently utilized for a variety of energy harvesting applications, such as power sources for deep-space missions, as well as waste-heat recovery from automobile engines [39].

Upon the application of a heat flux, the majority carriers diffuse along the direction of the temperature gradient. As the carriers diffuse, an opposing electric field is set up from the concentration gradient, which eventually limits further diffusion. For a given material, the voltage produced per unit temperature gradient is referred to as its Seebeck coefficient, in units of $\mu\text{V}\cdot\text{K}^{-1}$. The fundamental architecture of a thermoelectric device consists of sets of n-and-p-type material in series. Since the Seebeck coefficient for the p-type material is positive, while it is negative for the n-type materials, the voltages add up for each p-and-n-pair.

The maximum efficiency of a thermoelectric generator (assuming identical properties for the p-and n-type legs and a temperature drop of ΔT) can be written as [40]:

$$\eta_{max} = \frac{\Delta T}{T_h}\frac{\sqrt{1+zT}-1}{\sqrt{1+zT}+1}, \quad zT = \frac{S^2\sigma T}{\kappa} \tag{1.2}$$

In this expression, we assume that zT is typically evaluated at the mean of the hot-and-cold side temperature, $T_{ave} = \frac{T_h+T_c}{2}$. Note from (1.2) that η_{max} is scaled relative to the Carnot efficiency $\Delta T/T_h$, which is the maximum thermodynamic efficiency that a heat engine can achieve. In the

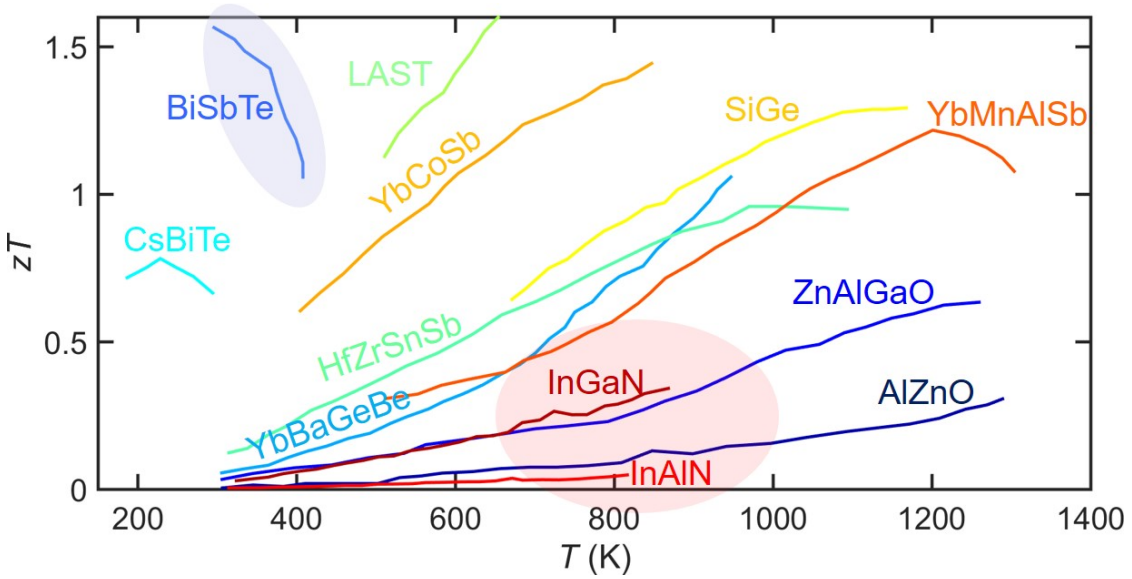

Figure 1.6: Energy harvesting within extreme high temperature environments. Data shown is for n-type materials and is compiled from Lu et al [10].

expression for zT, k is the thermal conductivity of the material, and σ is the electrical conductivity of the material. High values of zT for a material translate to a high conversion efficiency. For example, a zT of 3 is equivalent to a third of the Carnot efficiency, as per (1.2). As can be seen in Figure 1.6, the zT for even state-of-the-art thermoelectric devices is around 1-2 [39], which translates to a poor conversion efficiency. Thus, while thermoelectrics not suitable for for large-scale power generation (powerplants), they are suitable for scenarios where the ease of fabrication, integration, no moving parts, small size footprint and low power requirements outweigh efficiency considerations. Figure 1.6 shows the zT for several materials suitable for energy harvesting in extreme temeperature environments [10]. The temperature-dependent zT peak for materials depends on the bandgap. Beyond a certain temperature, the promotion of intrinsic minority carriers across the bandgap shifts the Fermi level to intrinsic, which results in a decreased Seebeck coefficient [10]. Wide-bandgap semiconductors, thus, are especially suited to high temeperature operation. We can make a few general observations based on Figure 1.6 as follows:

- Bi, Te, and Sb based compounds (such as BiSbTe) are standard thermoelectric materials for room temperature applications. However, their thermoelectric performance is heavily degraded at temperatures above 200°C [40], suggesting that alternative materials need to be explored.

- With the exception of SiGe, other promising high temperature thermoelectric materials (such

as LAST, YBCoSb, YbMnAlSb, PbTe, GeTe, and SnTe) utilize rare-earth and toxic materials, making them difficult to use for practical, commercial thermoelectric applications [10].

- Most thermoelectric materials have poor efficiencies at low temperature, making them (typically) unsuitable for such environments.

Finally, while thermoelectric generators using these complex materials have been developed commercially, they have large footprints (several cm) and are not compatible with typical semiconductor fabrication processes. These modules also cost over ∼1000$, making their use prohibitive for distributed sensing nodes. In such a scenario, a micro-thermoelectric generator that can be fabricated within an existing electronics/logic process is desirable. As of today, Si, SiGe and Bi/Te based compounds have been used for making micro-thermoelectric generators, but they are not desirable for extreme environment applications [32], with the exception of SiGe. While SiGe is one possible solution, electronics based on this material platform have only been demonstrated up to 300°C [41], as the bandgap of SiGe is less than 1.12 eV. As previously discussed, GaN-based electronics are stable to 1000°C [12] because of the much larger bandgap. Furthermore, GaN is extensively used today for commercial applications in high-power and RF electronics [7]. Thus, the development of a thermoelectric energy harvester with the existing fabrication pipeline for GaN is highly desirable.

Figure 1.6 also highlights the thermoelectric performance of some III-nitride materials that have been measured over the last few years. Efforts in this area began after the demonstration of a micro-thermoelectric generator made from doped GaN in 2009 [42]. The best performance to date has been recorded in InGaN with a zT as high as 0.34 at ∼600°C [43] (also highlighed in Figure 1.6), which shows that III-nitrides could potentially be good candidates for thermoelectric energy harvesting in high-temperature environments. As will be shown later in Chapter 2, the thermoelectric power density that we can obtain with an InGaN thermoelectric is below 0.3 mW per cm^2 of area footprint. On the other hand, a power density of a few mW per cm^2 is sufficient to power a sensor and wirelessly transmit the information from such a sensor elsewhere, as seen in Figure 1.5. In order to reach such power densities, we can take inspiration from the use of 2DEGs as thermoelectric elements, as they can have much higher thermoelectric performance from improved charge carrier mobility in comparison to the bulk. Such thermoelectric devices, often termed as a modulation-doped thermoelectrics, were first introduced in the seminal work by Ohta et al. [44] using $SrTiO_3$ as the material platform. In this thesis, we take inspiration from this approach and demonstrate a new polarization-based AlGaN/GaN 2DEG architecture with a large improvement in thermoelectric performance when compared to InGaN. The primary reason for this improvement is the high electron

mobility in the AlGaN/GaN 2DEG; the details are discussed later in Chapter 2.

1.4 Thesis Contributions

The major contributions of this thesis are the following:

- A micro-fabrication process to study the thermoelectric properties of the AlGaN/GaN 2DEG.
- Measurement and modeling of the thermoelectric properties of the AlGaN/GaN 2DEG over a wide temperature range (25 K to 600 K). These results show that the high temperature thermoelectric performance of AlGaN/GaN 2DEGs can exceed those of bulk GaN by a factor of ∼4x. Measurement of the low temperature thermoelectric properties show the existence of phonon drag in this material system for the first time, and how it can tuned to improve thermoelectric performance at cyrogenic temperatures.
- A novel thermoelectric architecture that uses AlGaN/GaN on top of pyramidal Si substrate to increase the output power and decrease the footprint of thermoelectric devices.
- A model to understand the behavior of AlGaN/GaN HEMTs under applied strain, with the context of its use in pressure/force sensors.
- Development of a novel, record-high performance UV photodetector using 2DEG interdigitated finger electrodes.

1.5 Thesis Outline

- Chapter 2 reviews some of the fundamentals of energy harvesting and AlGaN/GaN heterostructures. The chapter first discusses the growth of GaN on foreign substrates, which is followed by a discussion of quantum wells that can be formed in III-nitride heterostructures. After this, we review some of the basics of thermoelectrics and micro-thermoelectric generators. Finally, the fabrication methods to make the structures in this thesis are reviewed.
- Chapter 3 describes the measurement and modeling of the thermoelectric properties of the AlGaN/GaN 2DEG for a variety of buffer configurations. This is followed by a discussion of a novel pyramidal architechture which can lead to large improvements in the thermoelectric power output in lateral devices.

- Chapter 4 discusses a novel phenomenon called phonon drag, which leads to a large increase the thermoelectric performance of the AlGaN/GaN 2DEG at low temperatures. In particular, this chapter discusses a way to separate out the phonon drag component of the thermoelectric performance by comparing the Seebeck coefficient from multiple buffer configurations.

- Chapter 5 discusses novel sensors using the AlGaN/GaN 2DEG. In the first part of this chapter, the combined effect of applied strain and temperature on the device characteristics of AlGaN/GaN HEMTs is investigated. The developed model is a useful tool for predicting the response of HEMTs used in sensing and under the influence of packaging in extreme environments, especially when temperature fluctuation and strain coupling is of concern. The second part of this chapter discusses a novel photodetector that uses the AlGaN/GaN 2DEG for its electrodes, which leads to record signal-to-noise performance.

- Chapter 6 concludes the thesis and discusses further extensions of the work presented that can advance the field.

Chapter 2

Background

2.1 Gallium Nitride Heterostructures

Most III-nitride Heterostructures (GaN, AlN, InN and their alloys) that are found are grown via gas phase deposition of single crystal epitaxial layers onto substrates such as Si(111), Sapphire and SiC [45, 46]. The technique is specifically called metal organic chemical vapor deposition (MOCVD). Ways to grow III-nitride materials without epitaxy, such as ammonothermal growth exist [47]. However, they are very cost prohibitive (∼$800 for a 1 cm by 1 cm piece at the time of writing this thesis) and are limited to a maximum substrate size of 2“. In the MOCVD technique, vapor phase metal organic precursors are introduced into a reactor while the substrate is at a high temperature [46]. Typical precursors for Ga and Al are trimethylgallium (TMGa), trimethylaluminum (TMAl), while ammonia (NH_3) is used as the precursor for nitrogen gas [46]. In MOCVD, it is crucial to manage both strain due to CTE mismatch and defects due to lattice constant mismatch, as illustrated in Figure 2.1a. In particular, the best substrates for GaN growth have both low lattice mismatch and thermal coefficient mismatch, such as sapphire, SiC and AlN and Si(111). Although sapphire and SiC have been traditionally used for most power device applications, GaN-on-Si(111) is especially popular today due to low cost and reasonably low dislocation densities (10^8 cm^{-2}) [48]. In this thesis, we will exclusively use GaN-on-Si(111) heterostructures.

Because of the large lattice mismatch of GaN with Si (∼17%), a variety of transition structures, such as graded $Al_xGa_{1-x}N$, superlattices of AlN/GaN [49], and step-graded $Al_xGa_{1-x}N$ [50] are required. In this thesis, we will employ step-graded $Al_xGa_{1-x}N$ for growth of GaN layers on a Si substrate. Further details about this step-graded MOCVD recipe can be found elsewhere [50].

It should be noted that even with MOCVD, the growth of III-nitride layers is limited to a few micrometers due to limitations arising from cost and strain. When GaN/AlN is grown on Si, the crystal structure is wurtzite, with Ga(Al)-face [51]. This means that the termination of the crystal is with Ga(Al) atoms. Due to the ionic nature of the Ga-N bond and the noncentrosymmetric nature of the wurtzite crystal, a strong spontaneous polarization field develops in these crystals [51]. In addition, the application of an external strain leads to additional piezoelectric polarization charge in these crystals [52]. These effects can be used to make heterostructures with quantum wells, as we shall discuss next.

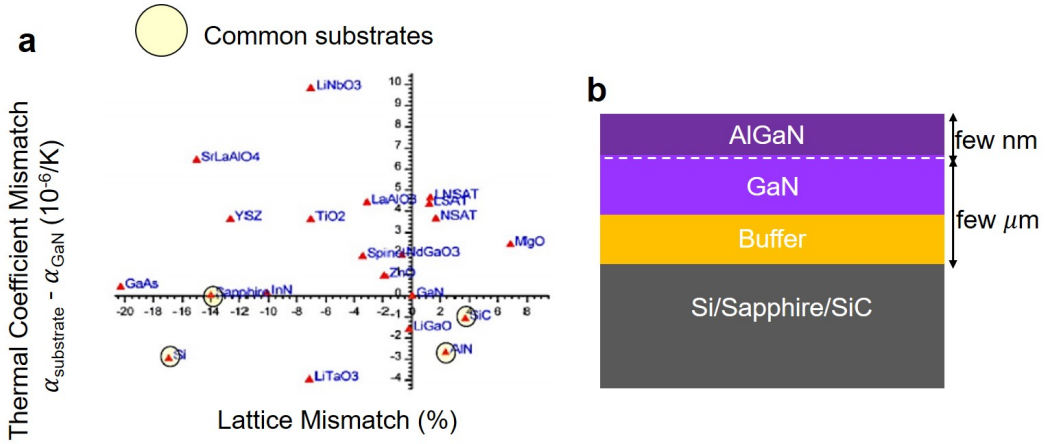

Figure 2.1: (a) Choice of substrate for GaN growth. (b) Typical cross-section of a gallium nitride heterostructure.

2.2 The Two-Dimensional Electron Gas

In III-nitride heterostructures, a two-dimensional electron gas (2DEG) can be formed when a thin (∼10-30 nm) barrier layer of a ternary nitride, such InGaN, AlGaN, or InAlN is deposited on top of a thick GaN layer (usually ∼1-3 µm) [51, 52]. In this thesis, we are concerned exclusively with AlGaN/GaN heterostructures and we will discuss this specific scenario. An example of such a heterostructure is depicted in Figure 2.1b. In these heterostructures, the barrier layer is regarded as being undoped (or unintentionally doped), thus the 2DEG is not formed from modulation doping, unlike traditional heterojunctions such as AlGaAs/GaAs. The 2DEG charge density is closely related to the imbalance of the spontaneous (P_{sp}) and piezoelectric (P_{pz}) bound polarization charges between

the barrier layer and the GaN layer [51]. Typically, the AlGaN layer is assumed to be pseudomorphic to GaN and hence develops a tensile strain which leads to the piezoelectric polarization charge in the AlGaN layer. The GaN substrate layer does not develop any piezoelectric polarization charge as it is assumed to not have any in-built strain.

Since these polarization charges are bound charges (not mobile), they only aid the formation of the 2DEG via surface traps or deep level donors present in the AlGaN layer [53]. In the limit of large AlGaN thickness (>20 nm), the experimental 2DEG density is found to be the difference in the polarization charge between AlGaN and GaN [53]. This value is usually around 10^{13} cm^{-2} for a 30 nm thick $Al_{0.25}Ga_{0.75}N$ layer, which is a standard experimental composition we will use in this thesis. However, at smaller AlGaN thickness, the 2DEG charge density is found to reduce below this value, eventually disappearing below ∼6 nm. Many models have been proposed to explain this phenomenon, and there still remains considerable debate in the community as to the correct physical model [53]. The standard model that explains this thickness dependence of AlGaN relies on the ionization of a discrete donor state at 1.65 eV from the top of conduction band at the AlGaN surface [54]. Excellent discussions of the different models can be found elsewhere [53, 54]. An in-depth discussion of the physics of AlGaN/GaN heterostructure is also discussed later in Section 5.1 of this thesis.

In order to accurately understand the properties of the AlGaN/GaN 2DEG, we rely on a commercial Schrödinger-Poisson solver (NextNano [55]) in this thesis. NextNano is optimized for III-nitrides and can incorporate the strain-dependent polarization fields present in these materials into the calculation of the band structure. As a representative, example, the band diagram of a GaN (3 nm)/AlN (1 nm)/$Al_{0.25}Ga_{0.75}N$ (30 nm)/GaN heterostructure is illustrated in Figure 2.2 at room temperature. The barrier height at the GaN cap surface is set to 1 eV [56] in the band diagram in Figure 2.2a. The 2DEG is visible at the AlGaN/GaN interface as a triangular quantum well. The integrated volumetric charge density corresponding to the triangular well, depicted in Figure 2.2b, leads to a sheet density of ∼10^{13} cm^{-2}. The calculated subband energy levels further reveal that the majority of charge (>90%) is present in the bottom subband of the triangular quantum well, which is important while calculating the mobility of the electrons in the quantum well. Although these calculations are for the sheet density at room temperature, measured sheet densities for the AlGaN/GaN 2DEG remain stable across a wide range of temperatures, from 50 K to 573 K [57], which is the range of test conditions for the devices described in this thesis.

The electron mobilites in the AlGaN/GaN 2DEG are an order of magnitude better than doped

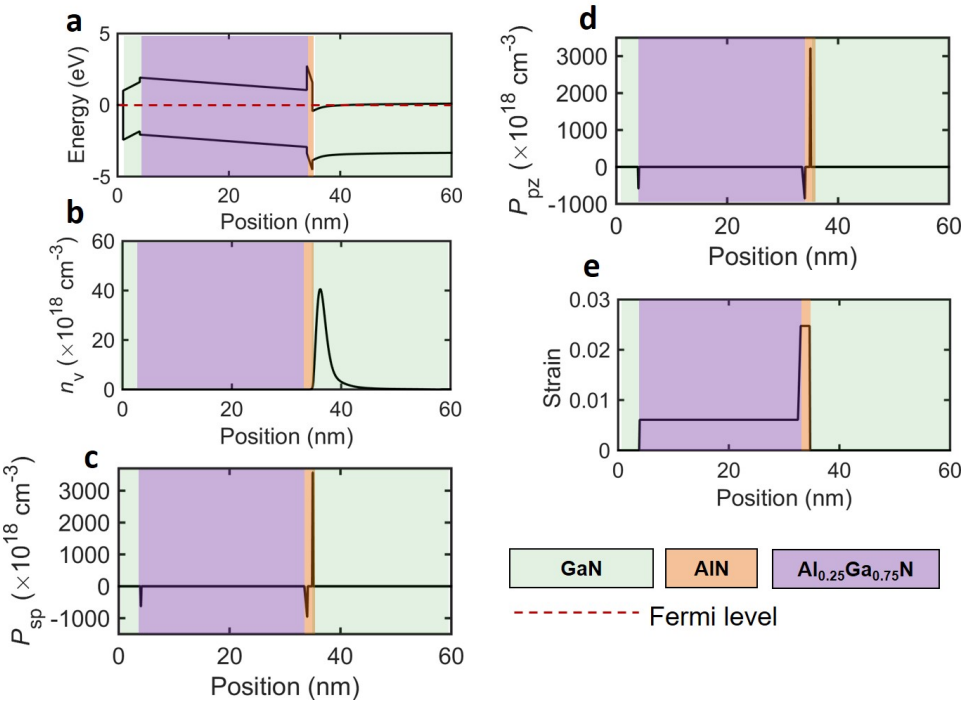

Figure 2.2: **A GaN/AlGaN/AlN/GaN heterostructure.** (a) Band diagram with Fermi level (red line), showing the 2DEG at the AlN/GaN interface. (b) Volumetric charge density. (c,d) Spontaneous and piezoelectric polarization charges as the interfaces. Note that at each interface the charge shown includes the contribution from both materials on either side of the interface. (e) Strain distribution in the heterostructure, showing tensile strain in the AlGaN and AlN layers. The tensile strain is used to calculate the piezoelectric polarization charge.

GaN at comparable volumetric densities. This is illustrated in Figure 2.3a, where the 2DEG mobility ($\sim$1800 cm^2·V^{-1}s^{-1} at room temperature) is from samples grown at Stanford with a $Al_{0.25}Ga_{0.75}N$ (30 nm) barrier layer. The mobility data for bulk GaN is taken from Mnatsakanov et al [58]. The dominant mechanisms which contribute to the scattering of 2DEG charge carriers include polar optical phonon scattering, roughness scattering at the AlGaN/GaN interface and acoustic phonon scattering (in the form of deformation potential scattering and piezoelectric scattering) [59]. Optical phonon scattering and roughness scattering are the most important of these scattering mechanisms. A model for the 2DEG mobility that we will use in this thesis, which accurately accounts for the different mechanisms can be found **Appendix A**.

It is important to note that scattering from remote ionized impurities is negligible because the barrier layer is undoped (unlike doped GaN) which leads to the high mobility. This can also be observed from the plot of the temperature dependence of mobility in Figure 2.3. For all the doped

samples, the mobility falls below a certain temperature, as ionized impurity becomes the dominant scattering mechanism at low temperatures. The 2DEG mobility, in comparison, increases to value close to ~10,000 $cm^2 \cdot V^{-1}s^{-1}$. Further, it is worth noting that the mobility of the 2DEG remains higher than the doped samples across the entire temperature range measured (from 50 K to 873 K). The values of the 2DEG samples and the bulk doped samples converge at high temperatures because polar optical phonon scattering becomes the dominant mechanism which limits the electron mobility.

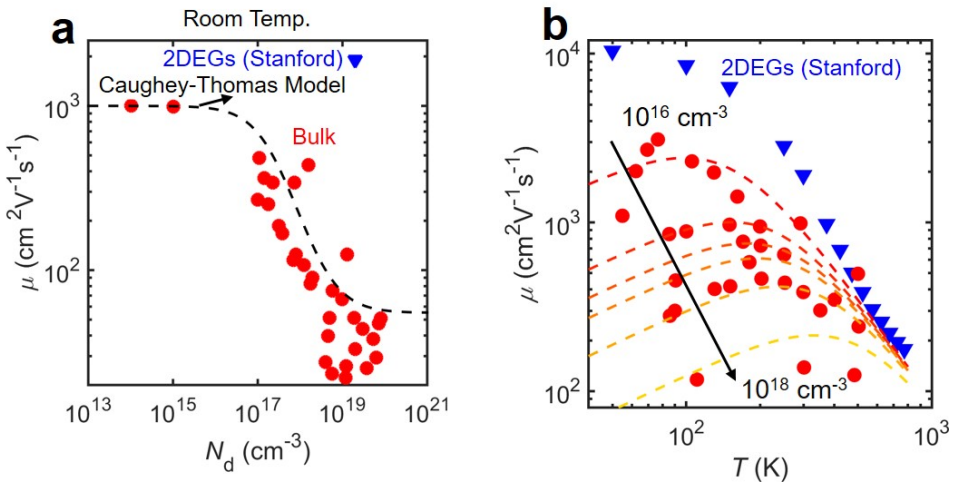

Figure 2.3: (a) Electron mobility in the AlGaN/GaN 2DEG in comparison with doped GaN [58]. (b) Temperature dependence of 2DEG mobility in comparison to doped samples.

2.3 Thermoelectric Properties

Excellent overviews of both the fundamentals of thermoelectric properties and their measurement techniques can be found elsewhere [60, 61, 62]. Here, we briefly review some of the key fundamental concepts that serve as groundwork for Chapter 3 and Chapter 4.

2.3.1 Thermoelectric Effects

Thermoelectric effects represent the coupling between heat and electric current flow, and can be fundamentally understood from the Onsager relations [63]. These relations express the current flux (J_e) and the heat flux (J_q) to gradients in the temperature (T) and voltage (V), and are written as

[63]

$$J_e = L_{11}\left(-\frac{dV}{dx}\right) + L_{12}\left(-\frac{dT}{dx}\right) \tag{2.1}$$

$$J_q = L_{21}\left(-\frac{dV}{dx}\right) + L_{22}\left(-\frac{dT}{dx}\right) \tag{2.2}$$

where L_{ij} represents a transport coefficient and x is the one-dimensional coordinate along the structure. Some of the transport coefficients are well known, for example, L_{11} is the electrical conductivity, σ. If there is no temperature gradient along the material (i.e., it is isothermal), we can derive a relation between J_q and J_e,

$$J_q = \frac{L_{21}}{L_{11}} J_e = \Pi J_e, \tag{2.3}$$

where Π is commonly known as a Peltier coefficient. This equation directly suggests a unique amount of heat flow (J_q) that occurs in every material when a current J_e flows through it. Thus, if two dissimilar materials, labelled 1 and 2, are connected and a current J_e is driven through them, heating and cooling will occur at the two junctions because of the difference in their Peltier coefficients ($\Pi_2 - \Pi_1$). The heating and cooling is then $(\Pi_2 - \Pi_1)I$, where I is the current flow in the material. In this thesis, we are more concerned with the generation of power, which is the current flow, J_e that is produced when a temperature gradient is imposed in the material. This is the opposite scenario to the Peltier effect. The open circuit voltage produced in a material due to a temperature gradient can be obtained by setting $J_e = 0$ in (2.1), and leads to the definition of the Seebeck coefficient,

$$S = -\frac{dV}{dT} = -\frac{V}{\Delta T} = \frac{L_{12}}{L_{11}}. \tag{2.4}$$

The Peltier coefficient is related to the Seebeck coefficient as $\Pi = ST$, where T is the temperature. The transport coefficients L_{ij} are fundamentally related to the band structure of the electronic material. Using a Boltzmann transport equation (BTE) formalism under the relaxtion time approximation (RTA), for a single band material, they can be expressed as [61]

$$L_{11} = -\frac{e^2}{3}\int v^2 \tau(E) \frac{\partial f_0}{\partial E} g(E) dE \tag{2.5}$$

$$L_{12} = \frac{e}{3T}\int v^2 \tau(E)(E - E_F) \frac{\partial f_0}{\partial E} g(E) dE \tag{2.6}$$

$$L_{12} = -\frac{1}{3T}\int v^2 \tau(E)(E - E_F)^2 \frac{\partial f_0}{\partial E} g(E) dE \tag{2.7}$$

$$\tag{2.8}$$

where E is the energy, $g(E)$ is the density of states, $f_0(E)$ is the Fermi-Dirac distribution, E_F is the Fermi level and $\tau(E)$ is the energy dependent scattering time for the charge carriers. Based on

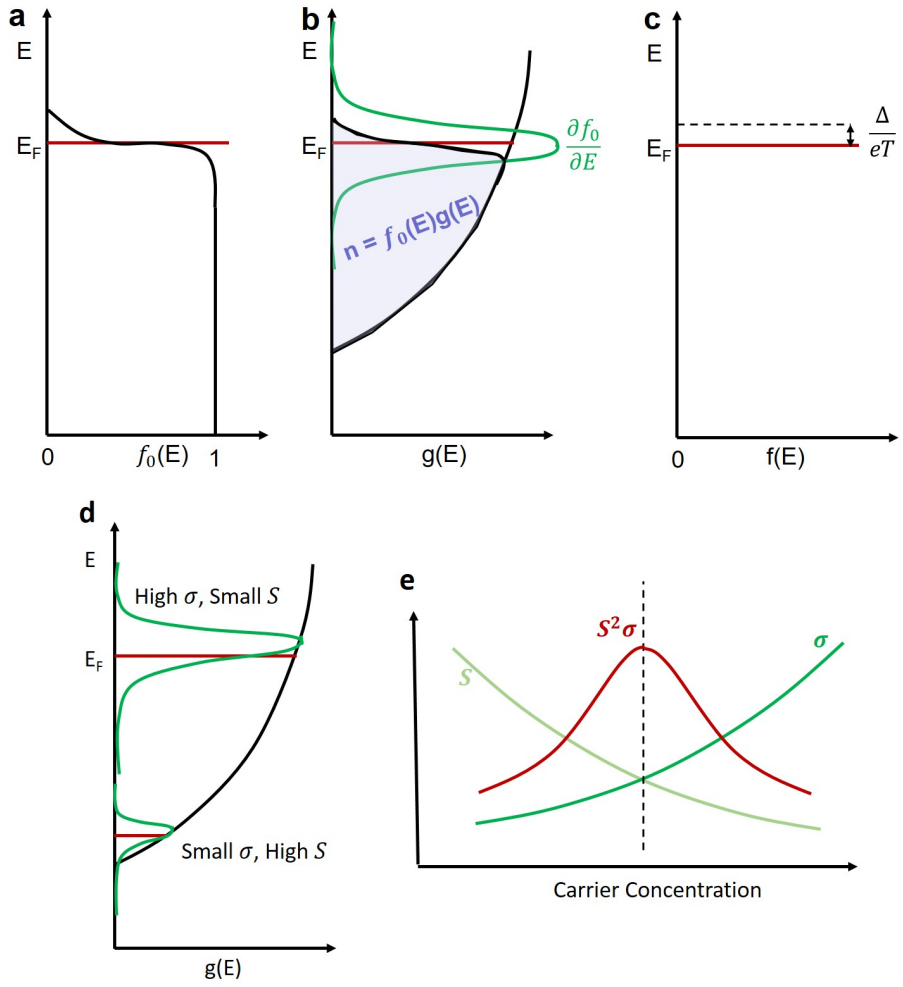

Figure 2.4: **Fundamentals of Thermoelectricity.** (a) Fermi-Dirac distribution at a finite temperature. (b) Conduction band showing the Fermi level, the derivative of the Fermi-Dirac distribution and the charge carrier distribution. (c) Conceptual diagram to show that only a small band Δ around E_F matters for both electrical conductivity and Seebeck coefficient. (d) Metals vs. semiconductors. (e) Optimization of the thermoelectric power factor ($S^2\sigma$) as a function of the charge carrier concentration.

these transport coefficients, we can now express the Seebeck coefficient as:

$$S = -\frac{1}{eT}\frac{\int v^2\tau(E)(E-E_F)\frac{\partial f_0}{\partial E}g(E)dE}{\int v^2\tau(E)\frac{\partial f_0}{\partial E}g(E)dE} \tag{2.9}$$

which shows that the Seebeck coefficient is fundamentally related to the average electron energy within the Fermi window. These concepts are illustrated in Figure 2.4, with the window (Δ) illustrated in Figure 2.4c. Thus, the Seebeck coefficient is related to how different the electron scattering time, $\tau(E)$ and the density of states, $g(E)$ are around the Fermi level. On the other hand, the electrical conductivity is directly related to L_{11}, and hence is determined by how large $g(E)$ is. Thus, metals usually have high σ but small S, while semiconductors with E_F near the edge of the conduction band usually have high S and small σ. This concept is illustrated in Figure 2.4d. As the position of the Fermi level is changed, the power factor $S^2\sigma$ can be optimized for maximum thermoelectric power conversion, as depicted in Figure 2.4e. Usually, degenerate semiconductors have the highest power factors. In this thesis, we are primarily concerned with the thermoelectric properties of 2DEG quantum wells, for which (2.9) applies with a few key differences:

1. The occupation of the 2DEG electrons in multiple subbands needs to be considered.
2. The density of states corresponds to the 2D case.
3. The scattering mechanisms corresponding to the 2DEG electrons need be individually calculated and summed up to obtain $\tau(E)$.

These points are discussed in detail in the later chapters. Finally, the Onsager relations, (2.1) and (2.2), can also be rearranged to express the heat flux (by eliminating the voltage) as

$$J_q = \Pi J_e - \kappa_e \frac{dT}{dx} \tag{2.10}$$

where $k_e = L_{22} - \frac{L_{12}L_{21}}{L_{11}}$ represents the electronic contribution to the thermal conductivity. In this thesis, this contribution is very small, and most the thermal conductivity is from lattice phonons, which we discuss next.

2.3.2 Thermal Conductivity

As discussed, reduction in thermal conductivity is a key component to optimizing thermoelectric performance. The phonon contribution to the thermal conductivity can be calculated via the BTE using the RTA [63]:

$$k = \sum_{LA,TA} \frac{1}{3} \int C(\omega) v(\omega) \lambda(\omega) d\omega = \sum_{LA,TA} \frac{1}{3} \int C(\omega) (v(\omega))^2 \tau(\omega) d\omega \tag{2.11}$$

where $C(\omega)$ is the phonon-mode specific volumetric carrier heat capacity, $v(\omega)$ is the phonon-mode specific velocity, and $\lambda(\omega)$ is the mode specific phonon mean free path. The integration is performed till the cutoff phonon energy, corresponding to the Debye wave vector. Further, the summation is performed for the two transverse phonon modes (TA) and the longitudinal phonon mode (LA). In our calculations, we assume a constant phonon velocity across the entire range of phonon frequencies, and also assume that a Debye relationship ($v = \frac{\omega}{k}$) holds for the phonons [63]. The mode specific scattering time is obtained by summing the scattering rates for the phonons via Mathiessen's rule [63]. The specific scattering mechanisms of interest to us are discussed later on in Chapter 3 and Chapter 4.

2.4 Micro-Thermoelectric Generators

2.4.1 Working Principle

A simplified thermal and electrical schematic of a thermoelectric generator is depicted in Figure 2.5a, with a thermal resistance diagram in Figure 2.5b. The n-and-p-type thermoelectric elements are electrically connected in series, while they are thermally connected in parallel. The electrical resistance of the thermoelectric generator is denoted as R_g, while the load resistor, across which the current (denoted by I) flows is denoted by R_l. In the analysis of micro-thermoelectric generators, it is typical to assume that the heat capacities of the ambient and the substrate to which the TEG is connected is large enough that their temperature does not change, even with heat flow through the TEG [64]. Thus, we can assume fixed temperatures T_h and T_c for the hot and cold side. The temperature drop across the TEG is **less** than $T_h - T_c$ because of the presence of of other thermal resistances, for example the substrate, heat sinks, ambient heat loss from convection and radiation, etc. We denote these resistances as $R_{t,h}$ and $R_{t,c}$ on the hot and cold side, respectively. The thermal resistance of the TEG is denoted as $R_{t,g}$. The space between the thermoelectric elements is usually occupied by a filler material (e.g. vacuum, air, or a dielectric), whose thermal resistance can be denoted as $R_{t,f}$. The fill factor, denoted by FF, represents the fraction of the area occupied by the thermoelectric elements. This is visually depicted in the top view of the thermoelectric generator,

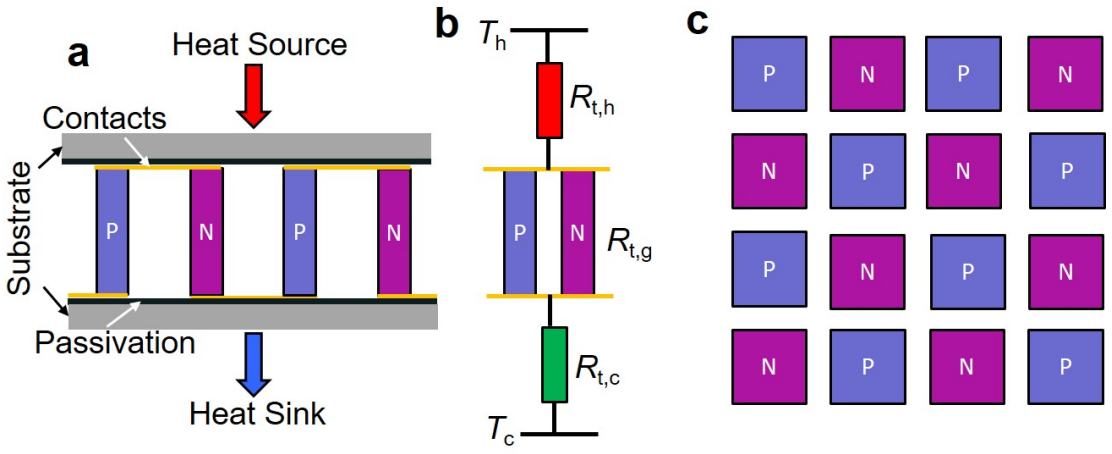

Figure 2.5: (a) Architecture of a typical vertical µTEG. (b) Simplified thermal resistance network of the µTEG. (c) Top view of the µTEG, illustrating the array of n-and-p-type thermoelements.

as seen in Figure 2.5c. The thermal resistances can be written as:

$$R_{t,g} = \frac{l_{t,g}}{k_{t,g}A(FF)}, \tag{2.12}$$

$$R_{t,f} = \frac{l_{t,g}}{k_{t,f}A(1-FF)}. \tag{2.13}$$

The actual temperature drop across the hot and cold sides of the TEG can then be written as $T_{g,h}$-$T_{g,c}$. The output voltage of the TEG can be expressed as:

$$V_{out} = N(S_p - S_n)(T_{g,h} - T_{g,c}), \tag{2.14}$$

where S_p and S_n represent the Seebeck coefficient of the p-type and n-type material, respectively, and N represents the number of thermocouple pairs. For simplicity, we will denote $S_{pn} = S_p - S_n$ Due to the current flow across R_l, Peltier cooling and heating occur at the hot and cold side (denoted by $Q_{p,h}$ and $Q_{p,c}$), respectively. The Peltier term can be calculated as:

$$Q_p = NS_{pn}IT, \tag{2.15}$$

where the temperature T could be either $T_{g,h}$ or $T_{g,c}$. In addition, Joule heating ($Q_j = I^2R_g$) due to current flow occurs in the TEG, which can be assumed to be equally distributed on the hot and cold side. Now, performing a nodal energy balance at the hot and cold junction, we get the main

relations which govern heat flow in a µTEG [64]:

$$Q_h = NS_{pn}IT_{g,h} + \frac{T_{g,h} - T_{g,c}}{R_{t,g}} + \frac{T_{g,h} - T_{g,c}}{R_{t,f}} - 0.5I^2R_g, \tag{2.16}$$

$$Q_c = NS_{pn}IT_{c,h} + \frac{T_{g,h} - T_{g,c}}{R_{t,g}} + + \frac{T_{g,h} - T_{g,c}}{R_{t,f}} + 0.5I^2R_g, \tag{2.17}$$

$$Q_h = \frac{T_h - T_{g,h}}{R_{t,h}}, \tag{2.18}$$

$$Q_c = \frac{T_{g,c} - T_c}{R_{t,c}}. \tag{2.19}$$

These equations can be used to understand the performance of the thermoelectric generator, as we discuss next.

2.4.2 Efficiency and Themoelectric Figure of Merit

The efficiency of the thermoelectric generator can be defined as the fraction of the input heat (Q_h) that is converted into usable electric power (P_{out}). Assuming that the temperature gradient is fully across the thermometric generator, using (2.14), (2.16) and (2.17), the efficiency, η can we written as [32]:

$$\eta = \frac{P_{out}}{Q_h} = \frac{V_{out}^2}{R_l Q_h} = \eta_c \frac{m}{(m+1) + \frac{(m+1)^2}{ZT_h} - \frac{\eta_c}{2}} \tag{2.20}$$

with

$$\eta_c = \frac{T_h - T_c}{T_h}, \tag{2.21}$$

$$m = R_l/R_g, \tag{2.22}$$

$$Z = \frac{S_{pn}^2}{k\rho}. \tag{2.23}$$

Here, (2.21) refers to the Carnot efficiency. In a typical thermoelectric system, the largest efficiency is obtained under a special choice of the thermoelectric and load resistors [32]:

$$m = \sqrt{1 + ZT_h(1 - \frac{\eta_c}{2})} \tag{2.24}$$

Under this choice of m, the maximum thermoelectric efficiency is [32]:

$$\eta_{max} = \eta_c \frac{\sqrt{1 + ZT_m} - 1}{\sqrt{1 + ZT_m} + \frac{T_c}{T_h}} \tag{2.25}$$

Equation (2.25) clearly states that in order to maximize the efficiency of conversion, one should focus on maximizing Z. Indeed, this is why ZT is often denoted as the thermoelectric figure of merit, and improving ZT has been the major focus of the thermoelectric community over the past few decades. It must be noted that the uppercase ZT is used when referring to system level thermoelectric performance, while lowercase zT is used to describe individual materials. Equation (2.25) also shows us that the efficiency of thermoelectric power conversion is limited by the Carnot efficiency, which is approached as $ZT \rightarrow \infty$. Large-scale (bulk) thermoelectric generators are usually optimized for maximum efficiency (usually less than 5%). However, in the design of micro-thermoelectric generators, it is usual to optimize the power output per area (power factor) instead of the maximum efficiency, as discussed below.

2.4.3 Power Density

The power density of a micro-thermoelectric generator is the output power per unit area per unit temperature difference [32]:

$$PD = \frac{P_{out}}{A(\Delta T)^2} \tag{2.26}$$

The full expression of the PD including the Peltier and the Joule heating terms can be found elsewhere [32]. The temperature drop across the thermoelectric elements, including the parasitic thermal resistors $R_{t,h}$ and $R_{t,c}$ is:

$$\Delta T_g = \left(\frac{R_{t,g}}{R_{t,h} + R_{t,g} + R_{t,c}}\right)\Delta T \tag{2.27}$$

Using Equation (2.27), the simplified expression for the power density excluding the Peltier and Joule terms is:

$$PD = \frac{N^2 S_{pn}^2 \left(\frac{R_{t,g}}{R_{t,h}+R_{t,g}+R_{t,c}}\right)^2}{4R_g A} \tag{2.28}$$

Equation (2.28) encompasses the most important features that are necessary to build a good micro-thermoelectric generator. In particular, it is necessary to ensure that most of the temperature drop is across the TEG and not the parasitic resistors, since this ensures that $\Delta T_g \rightarrow \Delta T$.

2.4.4 Conventional versus Hybrid TEGs

Conventional III-Nitride TEGs

As discussed previously in Section 2.1, III-nitride devices are grown by epitaxy with thicknesses limited to a few microns. Thus, if we were to make a traditional thermoelectric device from III-nitrides, as illustrated in Figure 2.5, with the hot side on top of the III-nitride and the cold side below the substrate, the performance of the device will be limited by the parastic thermal resistors $R_{t,h}$ and $R_{t,c}$. To confirm this, we can calculate the load-matched PD, as described in (2.28), accounting for realistic temperature drops across the parasitic thermal resistors. Using the defined thermal resistances, an approximate closed form solution for the actual temperature drop across the TEG can be written as [64]:

$$T_{g,h} - T_{g,c} = \left(\frac{(\frac{1}{R_{t,g}} + \frac{1}{R_{t,f}})^{-1}}{R_{t,h} + (\frac{1}{R_{t,g}} + \frac{1}{R_{t,f}})^{-1} + R_{t,c}} \right) (T_h - T_c) \tag{2.29}$$

To obtain practical values for the PD, we choose the thermoelectric properties corresponding to III-nitride material with the best cross-plane zT (InGaN) [43]. The values for the simulation parameters are listed in Table 2.1. Note that the properties listed here are at room temperature, with a temperature gradient ΔT of 10 K across the generator. Further, the resistance of the metal lines and the contact resistance of the metal lines to thermoelements are neglected. The values for $R_{t,h}$ and $R_{t,c}$ include a thermal resistance due to a 525 µm silicon substrate on the hot and cold side. For simplicity, both the p and n type thermoelements are assumed to have the same thermoelectric properties (with the p-type Seebeck coefficient having the opposite sign to the n-type Seebeck coefficient). In this simulation, we have assumed air to be the filler material. Figure 2.6 shows the results of these calculations. There are few key observations we can make from these Figures:

- As the leg length ($l_{t,g}$) increases, the power density first increases as a larger fraction of ΔT is dropped across the thermoelectric legs, but eventually decreases since the electrical resistance scales linearly with leg length.
- For small thermoelectric leg lengths that are of interest to us (Figure 2.6b), very small fill fractions (FF) produce the highest power density.

Within practical limits, these calculations clearly show that the output power will be limited below ~0.5 mW·cm^{-2}. This can be seen in Figure 2.6b with $FF = 0.01$ and $l_{t,g} \approx 3$ µm. In a practical scenario, the output power will be much lower because of un-optimized p-type material and parastic

Table 2.1: Simulation parameters for vertical InGaN µTEG shown in Figure 2.5.

Parameter	Value
Net Seebeck coefficient, S_{pn}	250 μV·K^{-1}[43]
InGaN thermal conductivity, $k_{t,g}$	4 W·m^{-1}K^{-1}[43]
InGaN electrical resistivity, $\rho_{t,g}$	5×10^{-5} Ω·m [43]
Cold reservoir temperature, T_c	300 K
Hot reservoir temperature, T_h	310 K
Total device area, A_{total}	10^{-5} m^2
Individual leg cross-sectional area, A_{leg}	2.25×10^{-10} m^2
Area-specific thermal resistance to heat source, $R_{t,h} \times A_{total}$	1.35×10^{-5} m^{2}K·W^{-1}
Area-specific thermal resistance to heat sink, $R_{t,c} \times A_{total}$	1.035×10^{-4} m^{2}K·W^{-1}
Silicon substrate thickness	525 µm

contact effects. It is clear the the small thickness of the III-nitride elements will limit thermoelectric performance, which motivates a different approach: hybrid µTEGs.

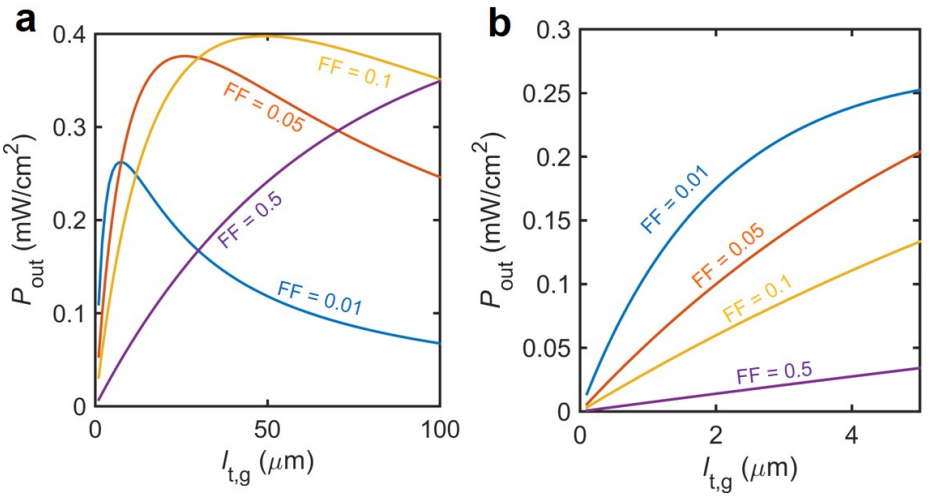

Figure 2.6: Simulations of the thermoelectric power density for a vertical InGaN µTEG at room temperature. The p and n elements are assumed to have the same thermoelectric properties. (a) Simulated power density with leg thickness from 1 to 100 µm for a variety of fill factors. (b) zoom-in of panel (a) and short leg lengths.

Hybrid TEGs

In a hybrid µTEG, the heat flow is still vertically in and out of the structure, but the current flow is lateral. This is because the thermoelements are laid laterally on top a suspended substrate, as shown in Figure 2.7a. Several hybrid TEGs have been developed because of compatibility with CMOS

(planar) processes, the details of which can be found in an excellent review elsewhere [32]. Here, we point out that a hybrid architecture is especially suitable for III-nitride based thermoelectrics. The key point to note is that because the the temperature gradient is lateral along the thermoelements (which can be long) their small thickness no longer limits the thermoelectric performance. In order to study these hybrid thermoelectrics, a simple finite element simulation (using COMSOL) was carried out. Figure 2.7b shows the simulation model to study thermoelectric performance in a hybrid TEG.

In the simulated architecture, we chose silicon as the substrate material, because III-nitrides can be grown with transition layers (buffer) on it. Further, Si can be easily released from the backside via a process such as deep reactive ion etching (DRIE), to direct heat flow along the thermoelements and into the substrate. It must be noted that we have included a thin metal plate on top of the thermoelements to contact the hot side, while the cold side is the bottom of the Si substrate. In our simulation, we included a buffer layer with a thickness of 3.25 µm. For the purpose of simluation, the buffer is considered electrically inactive and does not contribute to thermoelectric transport. Further, our thermoelements (both p-and-n-type) are 3 µm thick, which is a feasible limit for MOCVD growth. The thermoelectric properties of the thermoelements correspond to an AlGaN/GaN superlattice consisting of in-plane 2DEGs [65]. This is chosen because it has been shown to have the best thermoelectric properties in the III-nitride family, and is also uniquely suited to an in-plane geometry since the electron transport in the 2DEGs is planar. Although thermoelectric properties have only been measured for n-type superlattices to date, we still set the properties of the p-type element to be the same as that of the n-type element, with the opposite (positive) sign for the Seebeck coefficient. A thorough experimental investigation of the thermoelectric properties of AlGaN/GaN 2DEGs is also discussed in Chapter 3 and Chapter 4. The thermoelements are electrically insulated from the top plate by means of an dielectric. In our simulation, the dielectric (SiO_2) thickness is 3.25 µm. Some of the other parameters in the simulation are listed in Table 2.2. For simplicity, both the buffer and the thermoelements are assumed to have the same thermal conductivity. To study the power density, we performed a parameteric sweep of the thermal conductivity from 5 to 200 $W{\cdot}m^{-1}K^{-1}$. The results from this simulation are plotted in Figure 2.8, assuming a temperature gradient of 10 K from the top contact to the bottom of the silicon substrate. The simulated result is shown via the blue line. In calculating the output power density, the electrical properties of the contacts are neglected. Further, the inactive areas (suspension) legs also need to be accounted for in the calculation of power density. Here, we assume that the inactive area is equal to the active area. There are a couple of key observations we can make from this Figure:

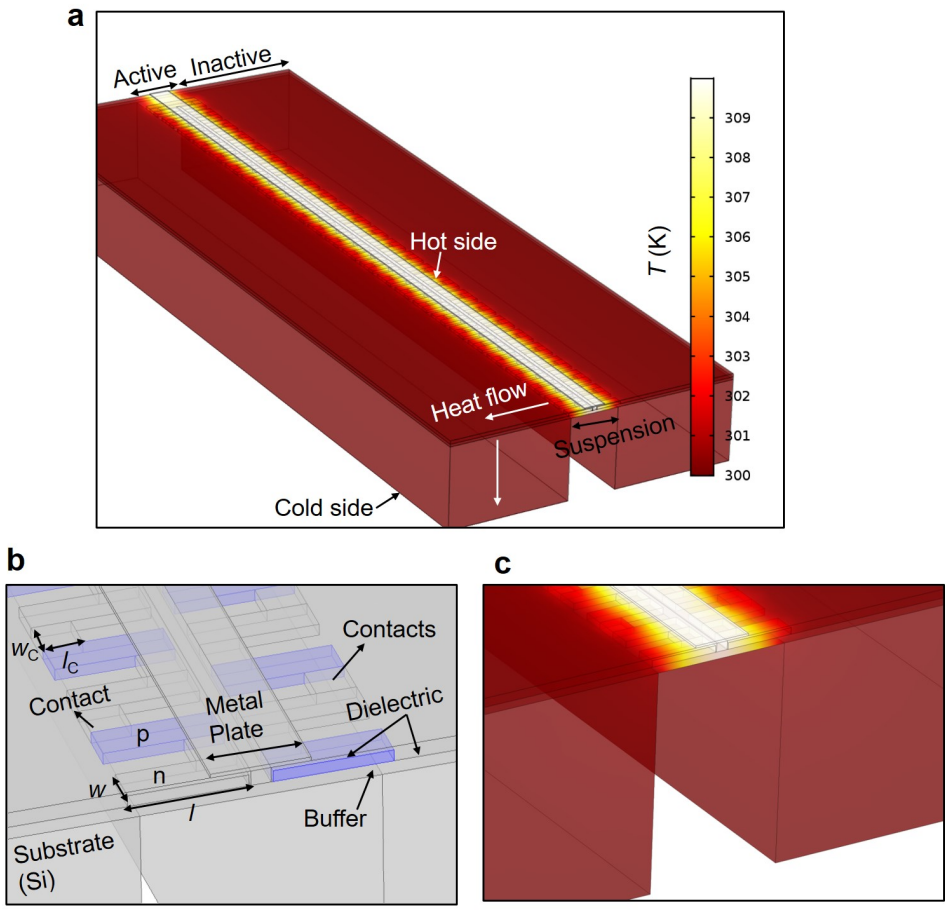

Figure 2.7: **Simulation of hybrid TEGs**. (a) Heat flow profile in a hybrid TEG. The active area refers to the region where the thermoelements are laid out, while the inactive area has the silicon substrate underneath. (b) Zoom-in showing the thermoelements, contacts, buffer, substrate, oxide and the top contact. (c) Close up heat profile, with same scale bar as in (a).

- The power density does not scale with the inverse of the thermal conductivity. To make this point clear, we have plotted the power density curve if it were to scale inversely with the thermal conductivity (orange line) in Figure 2.8. It is seen that while larger thermal conductivity does lower the power density, the drop is more gradual than suggested from a simple zT scaling. This suggests that it is more important to optimize for the thermoelectric power factor first ($S^2\sigma$) and consequently the thermal conductivity (k).

- The power densities are significantly higher than the vertical architecture. Even for the worst case scenario depicted in Figure 2.8 with $k = 200$ W·m^{-1}K^{-1}, the power density of 2 mW·cm^{-2}

Table 2.2: Simulation parameters for a hybrid TEG.

Parameter	Value
Net Seebeck coefficient, S_{pn}	400 μV·K^{-1} [65]
Buffer and thermoelement thermal conductivity	Varied in simulation
Oxide thermal conductivity	1.4 W·m^{-1}K^{-1}
Electrical resistivity of thermoelements $\rho_{t,g}$	2.0833×10^{-5} Ω·m[65]
Cold reservoir temperature, T_c	300 K
Hot reservoir temperature, T_h	310 K
Thermoelectric leg length, l	30 µm
Thermoelectric leg width, w	10 µm
Thermoelectric contact width, w_c	10 µm
Thermoelectric contact length, l_c	10 µm
Top plate width, w_{plate}	25 µm
Top plate thickness, t_{plate}	10 µm
Total area of thermoelements	60000 µm^2
Number of thermoelement pairs	49

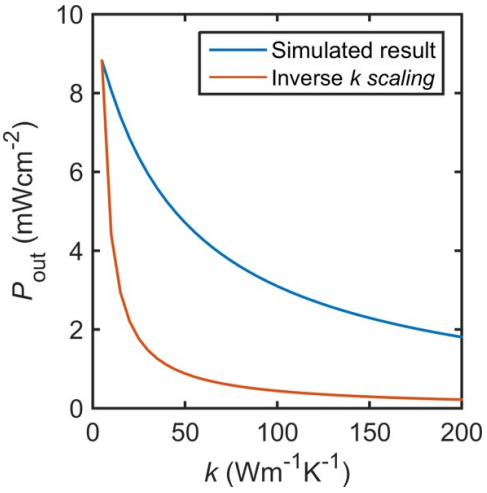

Figure 2.8: Power density from a simulated hybrid TEG with the thermal conductivity of the buffer and thermoelements varied for a temperature gradient of 10 K.

is 4x higher than the best case estimate of 0.5 mW·cm^{-2} that we estimated from the vertical InGaN architecture.

Both these points suggest that a hybrid thermoelectric architecture with a high thermoelectric power factor is a viable route to a practical III-nitride thermoelectric device. As further discussed in Chapter 3 and Chapter 4, AlGaN/GaN 2DEG quantum wells on top of a Si substrate achieve these specific aims.

2.5 Fabrication Process for GaN-on-Si MEMS

All the devices described in this thesis use an AlGaN/GaN-on-Si platform, with specific choices of metallization, passivation, and release processes. We discuss a typical fabrication flow to illustrate these choices. In our devices, fabrication usually begins with MOCVD growth or purchase of an AlGaN/GaN-on Si(111) wafer. The AlGaN barrier layer is usually 30 nm thick with 25% AlN. The 2DEG is present at the the AlGaN/GaN interface. It must be noted that the film thickness of the various MOCVD layers can be varied to tune device parameters, such as the thermal conductivity and electron mobility in the 2DEG.

2.5.1 Mesa etch

The first step in our fabrication process is the the isolation of 2DEG region. This is typically achieved by etching the AlGaN, and is referred to as a mesa etch process, as shown in Figure 2.9a. It is typical to overetch the AlGaN to ensure isolation. In the devices described in this thesis, the etch depth is ∼60-100 nm. We use an inductively coupled plasma (ICP) with chlorine/boron trichloride (Cl_2/BCl_3) to achieve this. The plasma power is low during etching (the forward inductive power is 250 W, while the RF power is 80 W) to ensure a small etch rate (∼10s of nm/min). Further details of this etching step can be found elsewhere [66]. In order to protect the regions where the 2DEG needs to be preserved, a standard 1 µm SPR 3612 photoresist mask is sufficient because of the relatively low etch rate (∼100 nm/min).

2.5.2 Metallization

Ohmic Contacts

The Ohmic contacts to the 2DEG in our devices consist of a Ti/Al/Pt/Au (20/100/40/80 nm) followed by a rapid thermal anneal (RTA) in N_2 ambient at 850°C for 35 seconds. This step is illustrated in Figure 2.9c. This particular recipe is a popular Ohmic contact metallization scheme used in the GaN community and is stable up to 500°C [67]. The theory behind the formation of an Ohmic contact using this metallization scheme can be found elsewhere [68]. The contact resistance from this metallization scheme is relatively high (∼10^{-5}-10^{-6} Ω·cm^2) and lower resistance contacts may be achieve by other means such as re-growth techniques [69, 70]. The devices in this thesis are several 10s of µm in dimension and the contact resistance is a small fraction of the channel resistance, hence, this metallization scheme is satisfactory.

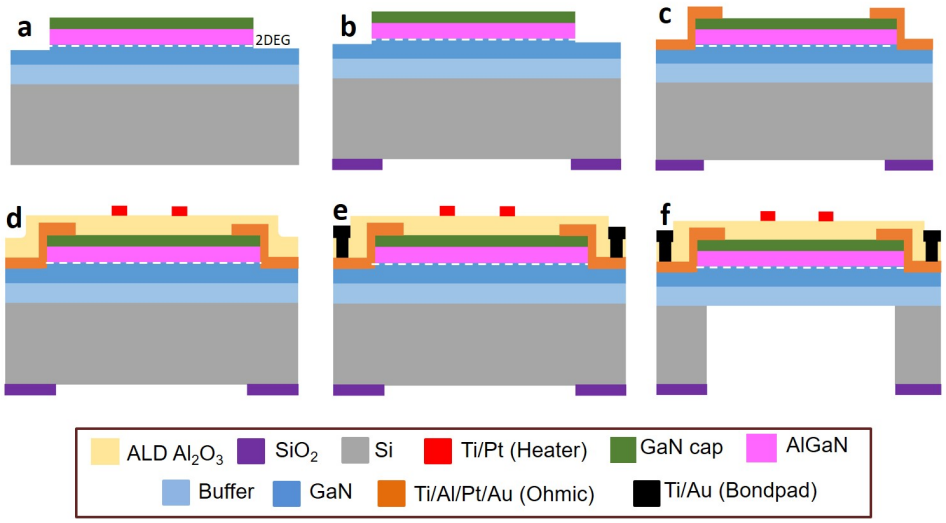

Figure 2.9: Outline of a GaN-on-Si MEMS fabrication process used at Stanford.

Schottky Contacts

A wide variety of metals (Ni, Au, Pt, Mo, Ir) have been used as a Schottky (gate) contact for the AlGaN/GaN 2DEG [71, 72, 73]. Typical metals chosen for Schottky contacts have high a high workfunction ($>$ 5 eV) and are stable at high temperatures. In this thesis, Ni, Pt and Au are used as Schottky contacts (e.g., gate metallization) for the AlGaN/GaN 2DEG.

On-chip heaters and temperature sensors

In the thermoelectric devices described in this thesis, on-chip heater and sensor elements are used to induce temperature gradients and to measure local temperature. A Ti/Pt (10/100 nm) metallization scheme is used specifically for this purpose. This step is illustrated in Figure 2.9d. Pt is chosen because of its high temperature coefficient of resistance (TCR) of $\sim 4\times10^{-3}$ and high electrical resistivity of $\sim 10.6\times10^{-8}$ Ω·m, which enables high sensitivity temperature measurements.

2.5.3 Passivation and Isolation

Atomic layer deposition (ALD) is used to deposit the dielectric films for passivation and isolation in this thesis. In particular, all the devices in this thesis use thermal ALD alumina (Al_2O_3) deposited at a temperature of 200°C, which is chosen because it was previously shown to be a stable, low-leakage dielectric for AlGaN/GaN MIS-HEMTs even at high temperatures up to 600°C [74]. Further, ALD

Al_2O_3 can easily be wet-etched in regions where contacts (vias) need to be deposited using a 20:1 Buffered Oxide Etch (BOE) solution. In the depicted fabrication flow, the alumina layer serves the purpose of electrical insulation between the current flowing in the heater and sensor metals and the 2DEG (Figure 2.9d).

2.5.4 Release Process

In this thesis, the suspended AlGaN/GaN devices are fabricated by a backside etch of the Si using deep reactive ion etching (DRIE). Our wafers typically have ∼500 µm of Si, which needs to be etched through completely. In our devices, we use deposit 4 µm of PECVD SiO_2 to protect the backside of the wafer in regions where release is not desired, which was chosen based on the the typical selectivity of the deep silicon etch chemistry is (>200:1). This step is shown in Figure 2.9b. The III-nitrides act as a natural etch stop to the silicon etch chemistry, enabling the creation of diaphragms with uniform thickness.

Chapter 3

Thermoelectric Properties of AlGaN/GaN 2DEGs

3.1 Tuning Thermoelectric Transport in AlGaN/GaN Heterostructures via Buffer Layer Engineering

In this section, we explore the thermoelectric properties of the AlGaN/GaN 2DEG from room temperature to 300°C. Portions of this section can also be found in our our paper [75].

3.1.1 Introduction

GaN thin films are being considered in the design of thermoelectric devices because of their high-temperature operation and potential for on-chip energy harvesting and sensing [42]. As a result, the electro-thermal transport in various GaN-based materials is being investigated [42, 43, 76, 77, 78]. The best performance to date has been recorded in InGaN with a zT as high as 0.34 at ∼600°C [43]. As discussed in Chapter 2, 2DEG heterostructures [79, 65] and GaN-based superlattices have attracted great attention in the design of thermoelectric devices as bulk doped materials are limited by very low mobilities when they are degenerately doped [58] (below 100 $cm^2 \cdot V^{-1}s^{-1}$). For example, recent experiments showed ∼10x improvement in power factor ($S^2\sigma$) over bulk doped GaN (as high as 2×10^{-3} $W \cdot m^{-1}K^{-2}$ using an AlGaN/GaN superlattice [65]), as well as simultaneous increase in Seebeck coefficient (S) and electrical conductivity (σ) for the 2DEG [79], contrary to bulk doped

materials. The primary contributor in the power factor enhancement is the improved 2DEG mobility [65], yet, the overall thermoelectric efficiency is limited by the high thermal conductivity [80] of its underlying GaN buffer (confinement) layer. To date, researchers have overlooked the ability to modify the GaN buffer layer to a reduced size in order to significantly scatter the phonons in it, while simultaneously preserving the electrical integrity of the 2DEG. Furthermore, the thermoelectric properties of material systems where the interfacial charge is caused by polarization fields (e.g., AlGaN/GaN) have not been investigated to date over a wide range of temperature and buffer configurations.

In this section, we present this remarkable ability to independently manipulate electrical transport separately from thermal transport in AlGaN/GaN heterostructures. This tuning behavior is possible as it arises from polarization fields, the electrons are tightly confined at the interface, while the phonons are in the material system [65]. Our device test platform is composed of a fully-suspended, microfabricated device architecture that enables characterization of the in-plane thermal and electrical transport in AlGaN/GaN heterostructures with varying buffer layer thickness. Figure 3.1 shows a conceptual schematic of the aims of this study. Transport properties are studied over a wide temperature range from 25°C to 300°C. Notably, we show that ∼100 nm thin GaN layers can considerably impede heat flow without significant electrical transport degradation, and that a large improvement (∼4x) in the thermoelectric figure of merit over externally doped GaN is observed in 2DEG based heterostructures. Furthermore, our experiments also demonstrate state-of-the-art [81] thermoelectric power factors (4-7$\times 10^{-3}$ W·m^{-1}K^{-2} at room temperature) observed in the 2DEG of this material system. As discussed in Chapter 2, high power factors are key to designing a good micro-thermoelectric generator. This remarkable tuning behavior and thermoelectric enhancement, elucidated here for the first time in the AlGaN/GaN 2DEG heterostructure, demonstrates how tuning the polarization fields at material interfaces can be used for thermal sensing and energy harvesting applications.

3.1.2 Test Structures

In order to measure the thermoelectric properties of the AlGaN/GaN 2DEG, we fabricated on-chip testing platforms. Figure 3.2a and Figure 3.2b are microscope images of our two fully-suspended heterostructure platforms for the measurement of in-plane thermal conductivity of the heterostructure stack and Seebeck coefficient of the 2DEG. A scanning electron microscope (SEM) image of a cross-section of the suspension region is shown in Figure 3.2c. These structures are based on the

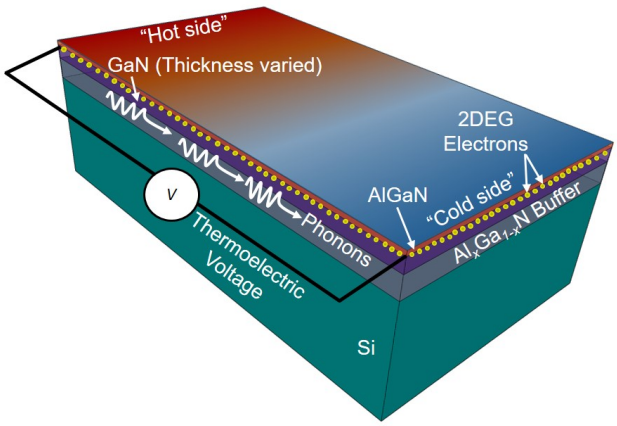

Figure 3.1: Conceptual schematic showing thermoelectric voltage generation via a lateral temperature gradient in the AlGaN/GaN 2DEG. The high mobility electrons in the 2DEG can lead to high thermoelectric power factors across the 2DEG. In this study, we explore how the thickness of the underlying GaN and buffer layers can be designed to preserve the thermoelectric power factor of the 2DEG but significantly reduce the in-plane thermal conductivity. This allows for a large improvement in the thermoelectric figure of merit in comparison with bulk doped GaN. Note that in our case we use the in-plane thermal conductivity of the GaN and the buffer (but not Si), since only these are necessary for 2DEG formation. ©2018 Wiley.

well-known central line heater method used in thermal characterization [62, 82]. The suspended platform was micro-fabricated using a seven-mask process, with deep reactive ion etching (DRIE) used as the final processing step to remove the Si(111) below the heterostructure, as seen in Figure 3.2c. The details of the fabrication process are in Appendix **B**. Two parallel, ∼5 µm wide Ti/Pt metal lines separated by 75 µm are used as heater and sensor thermometers, patterned on a ∼47 nm thick amorphous Al_2O_3 layer that provides electrical isolation from the heterostructure. For Seebeck coefficient measurement, only a heater thermometer is patterned adjacent to a 2DEG mesa with Ohmic contacts extending to the substrate, as illustrated in Figure 3.2b. We used an in-house metal organic chemical vapor deposition (MOCVD) system (Aixtron, Inc.) to deposit the AlGaN/GaN/buffer heterostructure layers on top of p-type Si(111) substrates with resistivity of 0.1 to 1 Ω·cm. Additional details about the growth process can be found in our former work [50]. The buffer layers ($Al_xGa_{1-x}N$, $0 \leq x \leq 1$) are unintentionally doped below 10^{16} cm^{-3}. Current-voltage (I-V) measurements after etching the 2DEG mesa were below the measurement resolution of our system (∼10 pA), which supports the assumption of $R_{buffer} \gg R_{2DEG}$, where R is the resistance. Thus the buffer layers can be considered semi-insulating. Forming of the 2DEG was accomplished

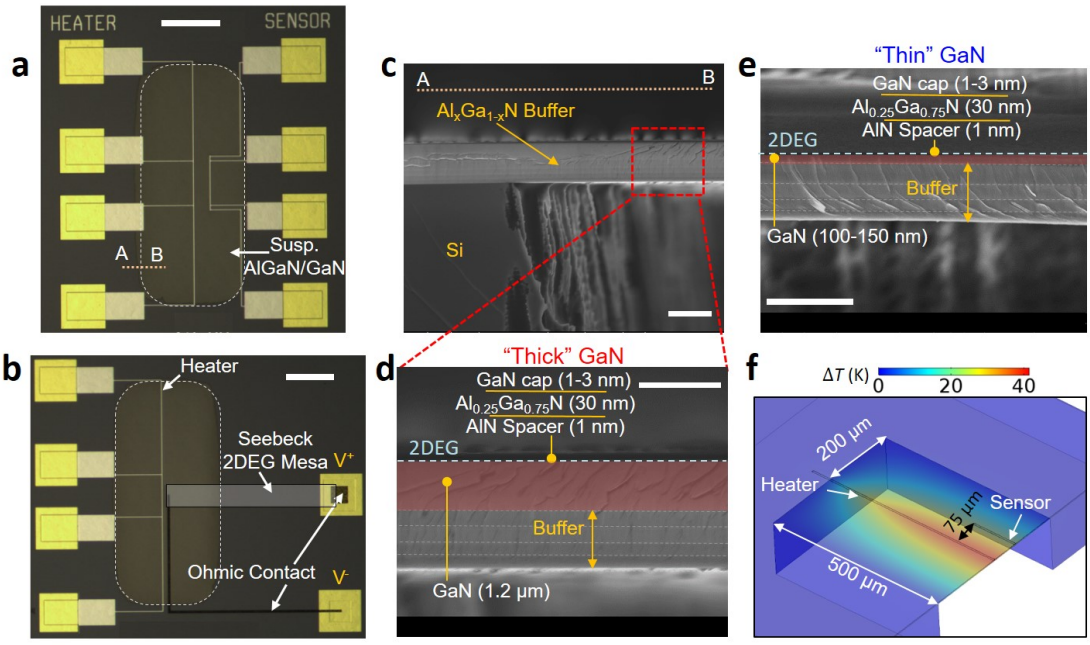

Figure 3.2: (a) Microscope image of the fully-suspended AlGaN/GaN heterostructure used for in-plane thermal conductivity measurements. The separation between the heater and sensor lines is ∼75 µm. A thin ∼47 nm ALD Al_2O_3 layer provides electrical isolation between the metal lines and the AlGaN/GaN heterostructure underneath. (b) Microscope image of the suspended AlGaN/GaN heterostructure to measure the Seebeck coefficient of the 2DEG. The 2DEG mesa is contacted via Ohmic Ti/Al/Pt/Au contacts. The Seebeck 2DEG mesa is shaded white for clarity. (c) Cross-section SEM image (of the A-B section in panel A) of the suspended heterostructure, with the Si substrate selectively etched out from the backside via DRIE.(d) SEM image of the thick GaN structure. The GaN thickness is ∼1.2 µm and false colored. The buffer structure, starting from the Si interface is composed of AlN (300 nm)/$Al_{0.8}Ga_{0.2}N$ (300 nm)/$Al_{0.5}Ga_{0.5}N$ (400 nm)/$Al_{0.2}Ga_{0.8}N$ (500 nm). (e) SEM image of the thin GaN structure, showing the 2DEG at the AlGaN/GaN interface and the buffer layers. The GaN thickness is ∼100-150 nm and is false colored. The other buffer layers are identical to the thick GaN structure. (f) Half-symmetric finite-element simulation of experimental structure, showing sample temperature profile when current is applied through the heater. Scale bars of (a)-(e) 200 µm, 200 µm, 3 µm, 2 µm, 2 µm. ©2018 Wiley.

by depositing ∼30 nm of unintentionally doped $Al_{0.25}Ga_{0.75}N$ barrier layer on the GaN layer in both heterostructure variants. A thin GaN capping layer of ∼3 nm was grown on top of the AlGaN barrier layer, and a 1 nm thick AlN spacer was inserted between the AlGaN and the GaN layers for 2DEG mobility enhancement [83]. Two variants of the heterostructure with GaN thicknesses of 1.2 µm and ∼100–150 nm are grown and called the "thick GaN" (Figure 3.2d) and "thin GaN" (Figure 3.2e) samples, respectively. The "thick GaN" heterostructure is a still a thin film, and reflects the heterostructure thicknesses that are typical for AlGaN/GaN power devices [48]. The thermal

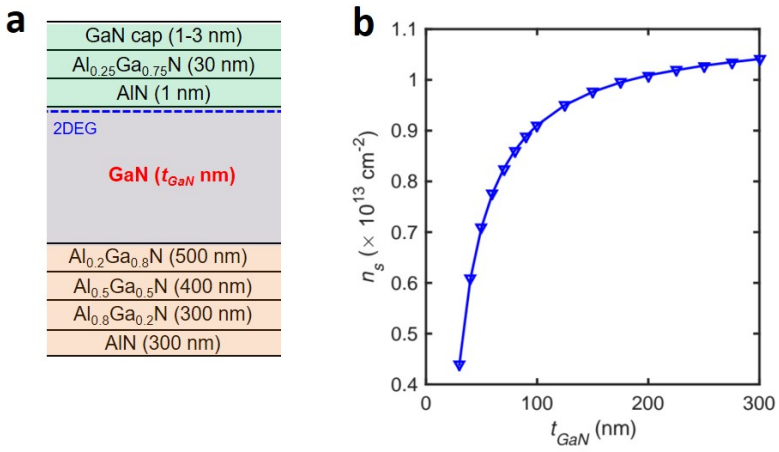

Figure 3.3: (a) Schematic of grown AlGaN/GaN heterostructure, along with the different buffer layers. (b) Schrödinger-Poisson simulation of decrease in 2DEG charge density (n_s) with reducing the thickness of the GaN buffer layer. ©2018 Wiley.

conductivity of the AlGaN/GaN/buffer hetero-structure is typically determined by the thermal conductivity of the GaN buffer layer. The thickness of the GaN (t_{GaN}) layer in the thin GaN sample was designed to lower the thermal conductivity of the buffer layer structure due to size effect, while preserving the charge density n_s of the 2DEG. This effect is shown in Figure 3.3b, which depicts the rapid decline in n_s with t_{GaN} due to band bending in the AlGaN and GaN layers from a Schrödinger Poisson model of the structure, which we discuss later. As the GaN layer thickness decreases below 100 nm, the decline is much sharper as the strain difference in the AlGaN/GaN layers decreases, leading to the GaN layer becoming pseudomorphic with the buffer layers beneath.

3.1.3 Thermal Conductivity Measurement

Measurement of the in-plane thermal conductivity is conducted as follows. The sample is attached to a temperature controlled chuck (Signatone Inc.) via a vacuum-compatible thermal grease (Apiezon Inc.) with air as the ambient. We pass a range of DC currents through the heater metal line to induce a temperature gradient in the heterostructure (Figure 3.2f) and simultaneously measure the electrical resistance of the metal electrodes. Typical current values are chosen to induce a maximum $\Delta T \approx 20$ K referenced to the substrate temperature, which varies from 25°C to 300°C. The placement of the sensor electrode was carefully designed to allow for a one-dimensional (1-D) in-plane heat transfer approximation in the diaphragm [62]. The electrical resistance of the electrodes was calibrated

over the entire temperature range using sufficiently low currents to avoid self-heating. Figure 3.4a

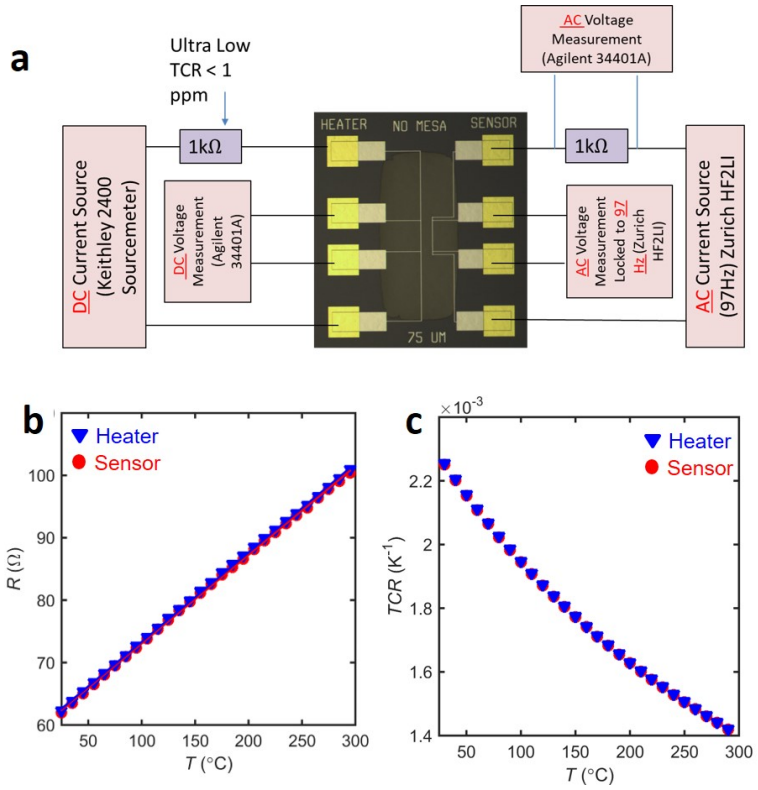

Figure 3.4: (a) Schematic of test setup. We measured the resistance of the heater electrode using a DC multimeter and voltage source with a calibration current of 50 µA. For the sensor side, we used an AC lock-in amplifier with frequency of 97 Hz to minimize self-heating effects. (b) Resistance-temperature calibration for the heater and sensor lines showing linear behavior. (c) TCR for heater and sensor lines. ©2018 Wiley.

shows the test setup used to measure the in-plane thermal conductivity of the AlGaN/GaN heterostructure. In order to ensure accuracy in the thermal conductivity measurements, we performed careful resistance versus temperature calibration for the Ti/Pt heater and sensor lines. For the heater line, a DC current source (Keithley 2400) and a DC voltage source (Agilent 34401) were used to measure the resistance of the Ti/Pt trace. To measure the resistance of the sensor line, we used an AC voltage lock-in amplifier (Zurich Instruments HF2LI) with a lock-in frequency of 97 Hz. AC voltage measurement across a fixed resistor (1 kΩ, ultra-low TCR of less than 1 ppm) was used to infer the AC current from the applied AC voltage. The lock in-amplifier was chosen for the sensor side to minimize self-heating effects and block environmental noise. In order to calibrate the resistances of both lines, the substrate of the suspended membrane was attached to a temperature

controlled chuck using high vacuum thermal grease (Apiezon, Inc.). A current value of ∼100 µA was carefully chosen for the purpose of resistance calibration to avoid self-heating effects.

Figure 3.4b and Figure 3.4c show the calibration curves of resistance (R) and temperature coefficient of resistance (TCR) till 300°C. Initially, we obtained a non-linear resistance-temperature calibration curve due to the effects of alloying in the Ti/Pt metal. In order to alleviate this problem, the entire sample was heated to ∼400°C and held for ∼10 minutes to anneal the Ti/Pt metals. Upon annealing, the resistance calibration curve is found to be extremely linear as can be seen in Figure 3.4b ($R^2 \approx 0.998$), and this is later used to extract the temperature of the heater line when heating power is applied to it to extract the thermal conductivity of the AlGaN/GaN heterostructure. The fitted slope is ∼0.148 $\Omega \cdot K^{-1}$, as can be seen in Figure 3.4b. Note that the plotted resistance values are obtained by averaging over 20 measurements spaced by 2 seconds at each substrate temperature. In each case, the error bar (defined as the range) for the resistance measurement is smaller than the size of the markers in Figure 3.4b and Figure 3.4c, with steadily increasing error bar as the temperature increases. Typical values for the error bars are ∼1.5 mΩ at 25°C with a steady increase to ∼50 mΩ at 300°C. Using the fitted slope, this implies an error of $< \pm 0.5$°C for the measured temperature even at 300°C, which is accounted for in the extraction of thermal conductivity.

The calibration allows us to convert the electrical resistance into corresponding temperature values using the measured temperature coefficient of resistance (TCR). From the collected temperature data, we can infer the in-plane thermal conductivity of the heterostructure given the heater power (P_H), after accounting for errors due to heat spreading into the Al_2O_3 and external losses. In order to understand the errors associated with the measurement and extract the thermal properties of the AlGaN/GaN/buffer heterostructure, a 3-D finite-element model using a commercial software (COMSOL) was implemented. Figure 3.2f shows a half-symmetric finite-element simulation of experimental structure, showing sample temperature profile when current is applied through the heater with the substrate fixed 25°C. The heater and sensor lines have a width (W) of 5 µm, and are spaced by a distance (D_{HS}) of 75 µm. The location of the heater and sensor resistances on the suspended membrane (R_H and R_S) are chosen such that the heat transfer can be well approximated as 1-D [62], which facilitates the extraction of the thermal conductivity. The typical variation of temperature along the length of these resistors is estimated to be <0.01% from the simulation model, which supports this assumption. Figure 3.5a shows a cross-section schematic of the thermal resistance network with the different pathways for heat sinking when current is applied to the heater metal. In the absence of external convective and radiative losses and negligible contribution of the alumina

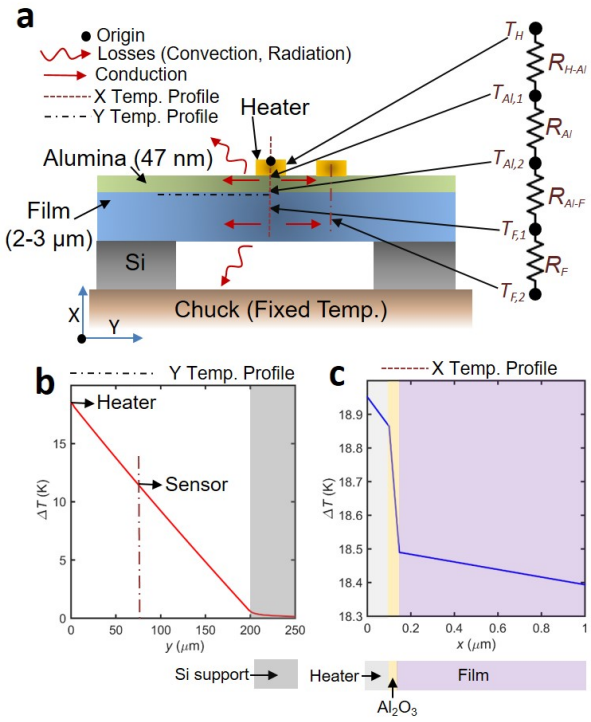

Figure 3.5: a) Thermal resistance network with the different pathways for heat sinking when current is applied to the heater metal. (b) Simulated lateral temperature profile in the AlGaN/GaN/buffer film with ∼14 mA heater current. The substrate fixed at 25°C (for the thick GaN film). (c) Simulated vertical temperature drop across the heater/Al_2O_3/AlGaN/GaN/buffer film for the same conditions in (b). ©2018 Wiley.

film to the in-plane heat conduction, the thermal resistance of the film (R_F) can be estimated as:

$$R_F = \frac{2(T_H - T_S)}{P_H} - 2R_{Al} - \frac{2(R_{mox} + R_{oxg})}{A_H} \tag{3.1}$$

where T_H and T_S are the heater and sensor line temperatures, P_H is the input power to the heater and R_{Al} is the thermal resistance of the Al_2O_3 layer, A_H is the projected area of the heater electrode (5 µm × 200 µm), R_{mox} is the thermal boundary resistance of the heater/Al_2O_3 interface and R_{oxg} is the thermal boundary resistance of the Al_2O_3/GaN interface. The thermal conductivity of the film can be extracted from R_F and the known film dimensions. The simulated temperature drop from the heater to the sensor in the GaN film is linear, as can be seen along the Y direction in Figure 3.5b. Equation (3.2) suggests that the thermal conductivity of the film can be measured accurately

in the limit of $R_F \gg R_{Al+Interfaces}$. The resistance ratio is analytically estimated as:

$$\frac{R_{Al+Interfaces}}{R_F} = \frac{T_{Al}k_F T_F}{k_{Al} W D_{HS}} + \frac{(R_{mox} + R_{oxg})k_F T_F}{W D_{HS}} \tag{3.2}$$

where T_{Al} and T_F are the thicknesses of the alumina and AlGaN/GaN/buffer film, respectively. We used a thermal boundary resistance of 2.8×10^{-8} $\mathrm{m^2KW^{-1}}$ for R_{mox} [84]. Although data for the thermal boundary resistance across the Al_2O_3/GaN film interface is not available, we estimated $R_{oxg} \approx 1\times10^{-8}$ $\mathrm{m^2KW^{-1}}$ based on measurements across amorphous dielectric/Si interfaces [85], since GaN and Si have similar Debye temperatures [86, 77]. At room temperature for the thick GaN film, using $T_F \approx 3$ µm, $T_{Al} \approx 47$ nm, $k_{Al} \approx 2$ $\mathrm{W{\cdot}m^{-1}K^{-1}}$ [84] and $k_F \approx 115$ $\mathrm{W{\cdot}m^{-1}K^{-1}}$, we estimate a thermal resistance ratio of ∼5.7%. For the thin GaN film, since $T_F \approx 2$ µm and $k_F \approx 45$ $\mathrm{W{\cdot}m^{-1}K^{-1}}$, the thermal resistance ratio is ∼1.48%, thus the error due to loss in Al_2O_3 is smaller than the thick GaN film. Note that these values also support the assumption in (3.2) that alumina does not contribute to the in-plane heat conduction, since $k_{Al}T_{Al} \ll k_F T_F$. At higher temperatures, the error due to this effect is less pronounced as k_{Al} is found to increase [84], while k_F further decreases. The loss via the Al_2O_3 and the interfaces can also be observed via the COMSOL model, as can be seen in Figure 3.5c (thick GaN film, substrate at 25°C). In the model, in addition to using $k_{Al} \approx 2$ $\mathrm{W{\cdot}m^{-1}K^{-1}}$, The temperature drops by ∼0.47 K in Al_2O_3 and interfaces on either side relative to ∼7.4 K in the GaN film (across D_{HS}), giving an error of ∼6.35%.

Figure 3.6 shows the typical thermal conductivity measurement procedure for our films. These plots are from experiments with the thick GaN sample. In this experiment, the substrate is held at 25°C. The sensor is maintained at the calibration current of ∼100 µA (Figure 3.6f), while the heater current is ramped up in a half-sinusoid from its initial calibration value (Figure 3.6b). Before each resistance measurement, we wait for 2 seconds after the current ramp to allow the system to equilibrate. The waiting interval of 2 seconds was chosen based on an estimation of a thermal time constant of ∼2 milli-seconds for the suspended membrane from COMSOL simulations. The heater and sensor temperature (converted from the resistance via the calibration curve in Figure 3.4b) track the current pattern, with the initial temperature equal to the substrate temperature, as seen in Figure 3.6c and Figure 3.6d. The extracted temperature difference can be used to calculate the in-plane film thermal conductivity via (3.2), after accounting for the Al_2O_3 temperature drop and external losses, which are discussed later. In addition, we also ensured that hysteresis did not occur in our heater and sensor lines. This is clear from observing the temperature versus power lines in Figure 3.6a and Figure 3.6e.

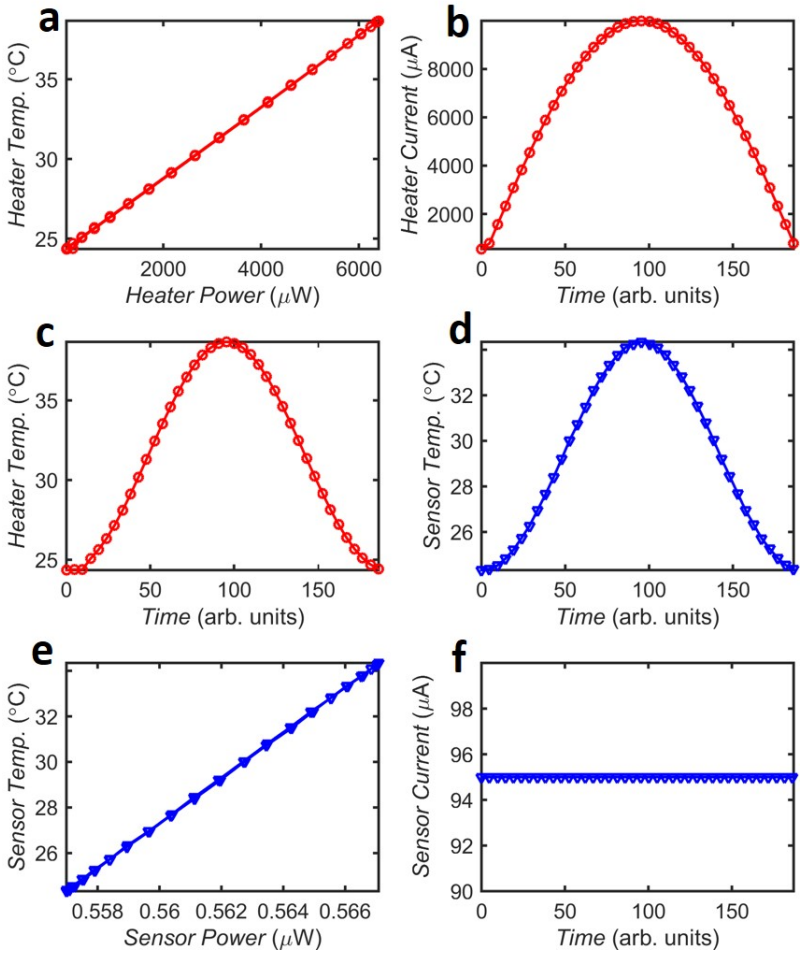

Figure 3.6: Thermal conductivity measurement. Panels (a)-(c) are for the heater line, while (d)-(f) are for the sensor line. These panels are for the thick GaN sample with the substrate held at 25°C. ©2018 Wiley.

In the model, we also included estimated values of the thermal contact resistance between the electrode, insulation and heterostructure interfaces. Overall, the errors due the insulation are found to be less than ∼6%, while errors due to external convective and radiative losses progressively increase to ∼10% at a substrate temperature of 300°C.

3.1.4 Seebeck Coefficient Measurement Procedure

The calibration procedure for the heater line in the Seebeck coefficient measurement platform for the thick and thin GaN samples is identical to the method described for thermal conductivity

measurement. The measurement of the Seebeck coefficient also follows a similar procedure; a current passed through the heater electrode induces a temperature gradient in the diaphragm, resulting in a Seebeck voltage across the 2DEG mesa that spans the suspension and the substrate regions (Figure 3.2b). Figure 3.7 shows a typical Seebeck coefficient measurement procedure. Similar to the thermal

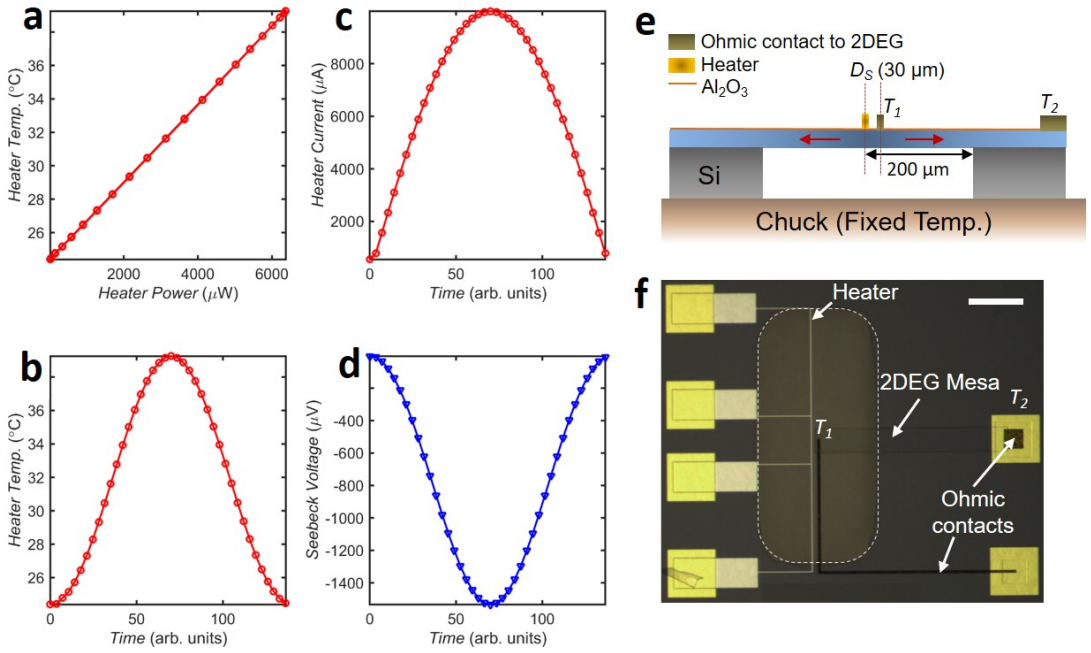

Figure 3.7: Seebeck coefficient measurement. Panels (a)-(c) are for the heater line, while (d) shows the Seebeck voltage measured in the 2DEG mesa. These panels are for the thick GaN sample with the substrate held at 25°C. (e,f) Cross-section and top view showing the different electrodes for Seebeck coefficient measurement. Scale bar of (f) 200 μm. ©2018 Wiley.

conductivity measurement, the heater current is ramped up from its calibration value, setting up a lateral temperature gradient along the 2DEG mesa which translates to a measurable Seebeck voltage (Figure 3.7d). The measured Seebeck voltage includes a minor contribution from the temperature drop across the Ti/Al/Pt/Au Ohmic contacts to the 2DEG (visualized in Figure 3.7f). At room temperature, we measured the Seebeck voltage across the 2DEG mesa and the Ohmic metal line for an identical temperature gradient. Using this, we estimated the contribution of the Ohmic metal line to be less than 2% of the overall Seebeck voltage, and thus neglected its effect in subsequent measurements. The Seebeck coefficient of the 2DEG is given as $S_{2DEG} = \frac{V_{2DEG}}{T_1 - T_2}$, as depicted in Figure 3.7e and Figure 3.7f. Note that the measured Seebeck coefficient corresponds to the 2DEG contribution exclusively since the III-V buffer layers are semi-insulating. The temperature at the

contact outside the suspended region (T_2) is assumed to be at the substrate temperature. The temperature drop in the silicon supported region is <1% of the total temperature drop ($T_1 - T_2$) (Figure 3.5b), thus, the contribution to the Seebeck coefficient from the supported region can be ignored. T_1 is related to the heater temperature T_H as:

$$\frac{T_H - T_1}{P_H} = R_{Al} + \frac{R_F}{2} + \frac{R_{mox} + R_{oxg}}{A_H} \tag{3.3}$$

where R_F is calculated using the measured film thermal conductivity and a length of 30 µm (D_S, depicted in Figure 3.7e) and R_{Al} is calculated as discussed earlier.

3.1.5 Note on High Temperature Losses

External losses from convection are significant at high temperatures which lead to errors in the thermal conductivity measurement. This can be seen in Figure 3.8a, which shows the temperature profile when no current is applied through the heater with bottom fixed at 200°C for the thick GaN film. Notice the cooling in the suspended membrane due to external convection, leading to a relative temperature difference between the heater and the sensor line. This underestimates the ΔT between the heater and the sensor line, leading to a higher measured thermal conductivity than the true value. The actual temperature gradient can be expressed as $\Delta T_{real} = \Delta T_{meas} + \Delta T_{corr}$, where ΔT_{corr} is the temperature gradient from the heater to the sensor with no current applied. The prominence of this effect is seen in Figure 3.8b and Figure 3.8c, which shows the simulated true and estimated measurements of the thermal conductivity for the normal GaN and thin GaN film. The error in the measured thermal conductivity is estimated to be ∼4% and ∼10% for the normal and thin GaN films from simulations, using an external convection coefficient of 10 $\mathrm{Wm^{-2}K^{-1}}$. The correction factor ΔT_{corr} can be estimated from the natural convection coefficient (h). At progressively higher temperatures, a non-zero Seebeck voltage is observed when no current is applied in the heater line due to the effect shown in Figure 3.8a. Then, using the most recently corrected thermal conductivity value, we estimated the value of h required to produce the observed non-zero Seebeck voltage using our knowledge of the Seebeck coefficient from the COMSOL model. Following this, we obtained the correction factor ΔT_{corr} for the current thermal conductivity value. Typical values for h estimated using this procedure are in the range of 12-14 $\mathrm{Wm^{-2}K^{-1}}$, which are reasonable coefficients for natural convection. The correction factors (ΔT_{corr}) we obtained for the normal GaN and thin GaN films for the different substrate are tabulated in Table 3.1.

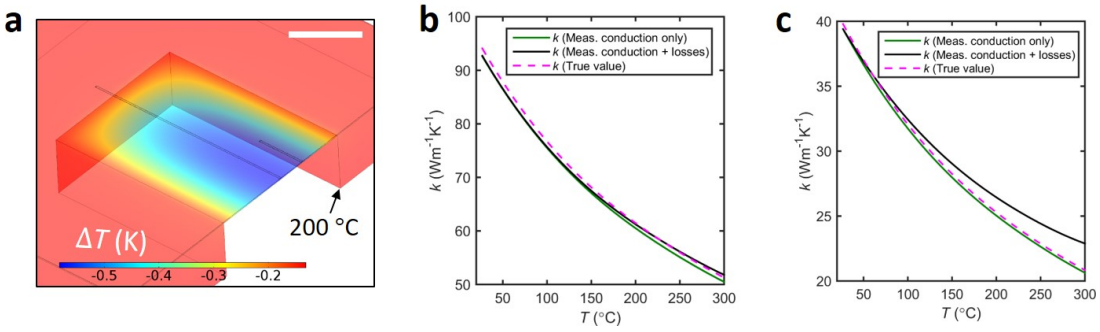

Figure 3.8: (a) Temperature profile when no current is applied through the heater with bottom fixed at 200°C. Notice the cooling in the suspended membrane due to external convection. This effect becomes prominent at temperatures above ∼100°C. (b,c) Thermal conductivity measurements predicted from finite-element model for thick and thin GaN samples, respectively. At higher temperatures, the measured thermal conductivity is higher than the actual thermal conductivity due to the cooling losses described in Figure 3.8a. The scale bar of panel (a) is 200 µm. ©2018 Wiley.

Table 3.1: Estimated thermal conductivity correction factors.

T(°C)	Bulk GaN	Thin GaN
75°C	–	0.055
100°C	–	0.097
150°C	0.096	0.19
200°C	0.17	0.31
250°C	0.32	0.62
300°C	0.63	1.1

3.1.6 Electrical Conductivity Measurement

Circular transfer length method (CTLM) test structures with gap spacing (d) varying from 20-70 µm (Figure 3.9a) were used to measure the sheet resistance of the 2DEG and the contact resistance for the thin and thick GaN samples. The inner radius (L) of the circular test structures was designed to be 500 µm, such that the approximation $L \geq d$ is valid. In the regime where $L \geq d$, the total resistance R_T between the inner and outer contact can be expressed as [87]:

$$R_T = \frac{R_{sh}(d + 2L_T)}{2\pi d} \log(1 + \frac{d}{L}) \tag{3.4}$$

where L_T is the transfer length and R_{sh} is the sheet resistance of the 2DEG. Here, L_T is related to R_{sh} and the contact resistance ρ_c as:

$$L_T = \sqrt{\frac{\rho_c}{R_{sh}}} \tag{3.5}$$

Figure 3.9b illustrates the variation of the total resistance R_T with gap spacing d (via (3.4)) for the thin and thick GaN samples at 25°C, which is used to extract R_{sh} and ρ_c. Using the 2DEG thickness, t_{2D}, the extracted R_{sh} is used to extract the 2DEG conductivity. The values of R_{sh} for the thick and thin GaN sample are also shown in Figure 3.9d. The contact resistance values are noted to be in the right range for typical 2DEG Ohmic contacts [88] (10^{-5}–10^{-6} Ω· cm^2) and decreasing with increasing temperature due to enhanced thermionic field emission across the GaN/AlGaN layers [68, 89], as observed in Figure 3.9c. A similar magnitude of decrease has also been observed in former work [90]. Lastly, electrical conductivity of the 2DEG for the thick and thin GaN samples

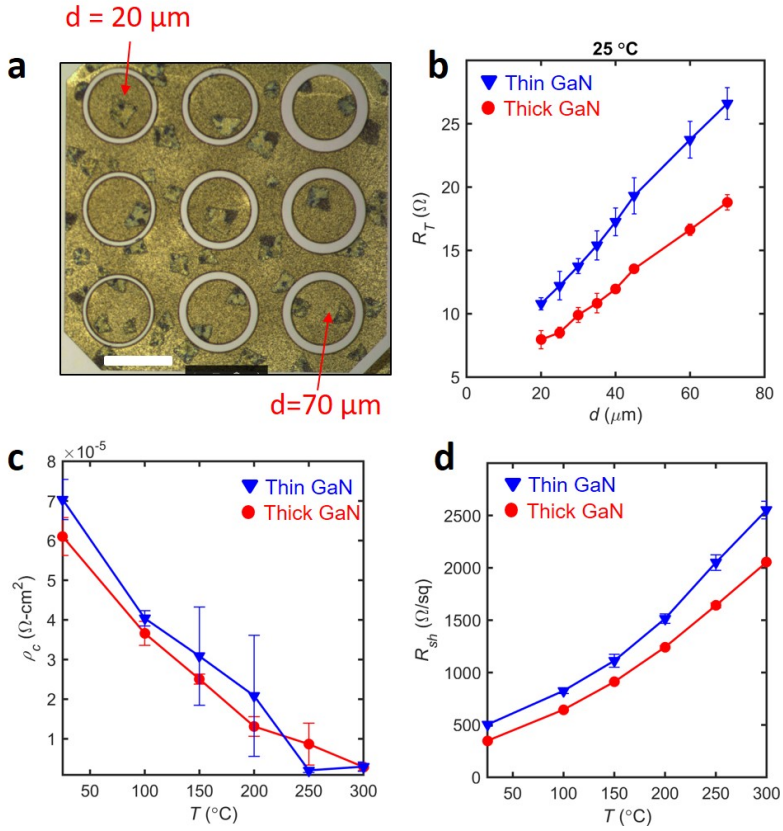

Figure 3.9: CTLM Measurements. (a) CTLM test array for measurement of contact sheet resistance with gap spacing varying from 20 µm to 70 µm. (b) Transfer resistance versus gap spacing for the thin and thick GaN samples to extract sheet contact resistance at 25°C. (c) Temperature dependent contact resistance for the thin and thick GaN samples. (d) Temperature dependent sheet resistance for the thin and thick GaN samples. Error bars are obtained from measurements across 4 identical CTLM test arrays. Scale bar of (a) 500 µm. ©2018 Wiley.

is obtained using the data from the CTLM measurements with the aid of simulations to obtain the

thickness of the 2DEG triangular potential (t_{2D}) well, as discussed next.

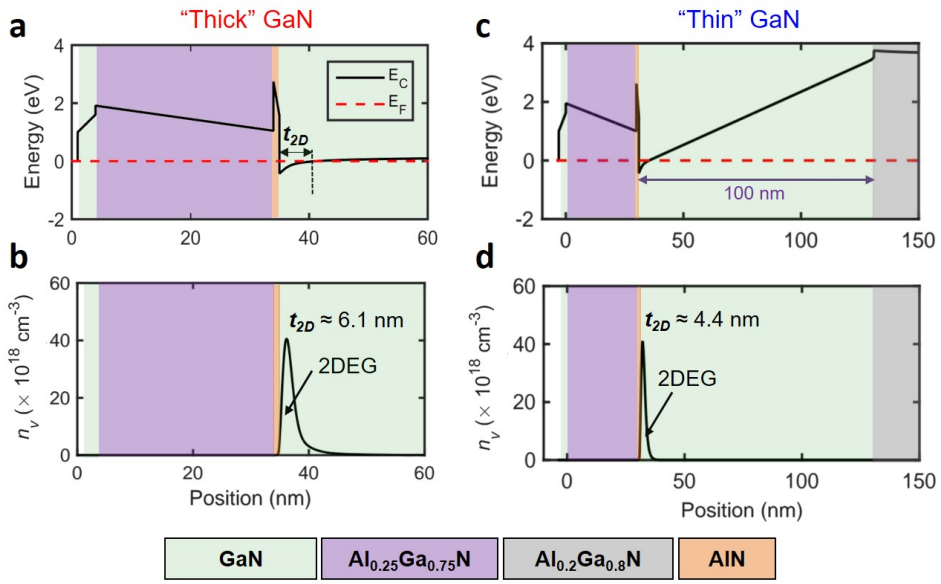

Figure 3.10: (a) Schrödinger-Poisson model of the energy band diagram for the thick GaN structure with AlGaN thickness is 30 nm. The thickness of the 2DEG region, t_{2D}, is shown in the region where GaN is degenerate. (b) Volumetric charge density, n_v, versus position, depicting the approximately triangular charge profile, with $t_{2D} \approx 6.1$ nm. (c) Simulated energy band diagram for the thin GaN structure with AlGaN thickness of 30 nm. Note that the GaN layer is 100 nm. (d) Volumetric charge density, n_v, versus position, depicting the approximately triangular charge profile, with $t_{2D} \approx 4.4$ nm for the thin GaN structure. ©2018 Wiley.

3.1.7 Charge Profiles

The thickness and charge density of the 2DEG for the thick and thin GaN heterostructures are simulated using a commercially-available Schrödinger-Poisson solver (NextNano GmbH [55]). The simulated band structures and volumetric charge density profiles for the thick and thin GaN heterostructures are illustrated in Figure 3.10. All the heterostructure layers are assumed to be undoped and the barrier height for the GaN capping layer is set to 1 eV [56]. The entire structure is simulated using a 1-D grid size of 0.5 nm, except in the region where the 2DEG quantum well forms, where we used a finer grid of 0.1 nm. In both cases, the simulation requires a substrate to determine the strain in the heterostructure. For the thick GaN model, we used a thick 500 nm GaN layer as the substrate to converge the 2DEG sheet density (n_s). However, for the thin GaN model, the GaN layer was set to 100 nm, while the thick layer below it, $Al_{0.2}Ga_{0.8}N$, was used as the substrate to

determine the strain level. A 500 nm thick $Al_{0.2}Ga_{0.8}N$ layer was sufficient to converge the charge density in the thin GaN model. A lattice temperature of 300 K was used for the both models. The source code for both models is available in Appendix **C**. In both cases, the 2DEG region is visible as a triangular potential well near the AlGaN/AlN/GaN interface, as seen in Figure 3.10. From the simulation, we found $n_s = 1.06 \times 10^{13}$ cm^{-2} and $n_s = 0.91 \times 10^{13}$ cm^{-2} for the thick and thin GaN heterostructures, respectively. The Schrödinger-Poisson model is validated by comparing the sheet

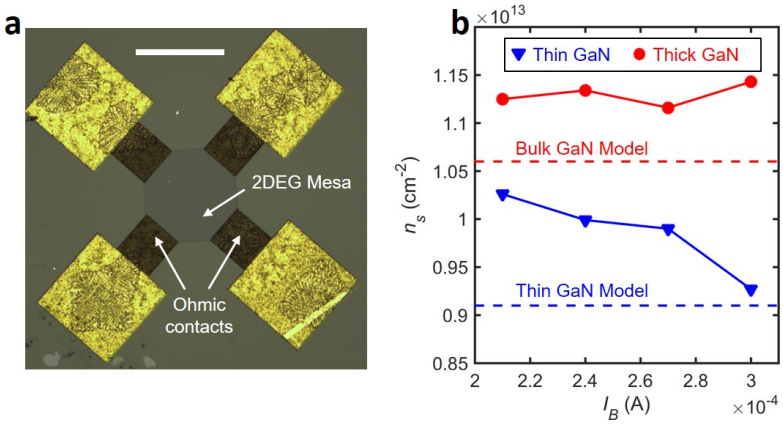

Figure 3.11: Room temperature Hall-effect Measurements. (a) Van der Pauw structure used for Hall-effect measurements. An octagonal 2DEG mesa region is used. These devices are co-fabricated with the other electrical and thermal transport test structures described in this section. (b) Extracted sheet density (n_s) for a range of applied bias currents (I_B) at room temperature. The estimates from the Schrödinger-Poisson model are shown using dashed lines. Scale bar of (a) 200 µm. ©2018 Wiley.

densities obtained from the model with the values obtained from Hall-effect measurements. The sheet density is ∼16% lower for the thin GaN sample due the reduced 2DEG quantum well depth (t_{2D}), but has a similar peak volumetric charge density as the thick GaN sample, as discussed in Figure 3.10. A simple, 4-contact Van der Pauw structure was used to characterize the sheet density via Hall-effect measurements. The structure is shown in Figure 3.11a. The conducting 2DEG area for each Hall-effect plate was 200 µm × 200 µm. Using a range of bias current levels (I_B), an external magnetic field (B) of ≈1 mT, n_s is related to the Hall voltage V_H as

$$n_s = \frac{I_B B}{q V_H} \tag{3.6}$$

where q is the electronic charge. The results from these experiments performed at room temperature are depicted in Figure 3.11b. Good match between the sheet densities obtained from the experiments

and the model is observed. The values from the experiments are about 5-10% higher than those predicted from the Schrödinger-Poisson model, however, we note that the average difference in the sheet densities of the thin and thick GaN samples from experiments (∼14.3%) and the model (∼16.5%) is predicted accurately, which serves as a validation for the model, in particular, the thin GaN heterostructure. The fluctuation in the experimentally observed n_s values for different bias currents (I_B) could arise from non-linearity in the current-voltage characteristics and other sources such as offset voltage from thermal effects [91].

The physical thickness of the 2DEG region, t_{2D}, can be extracted as the region where GaN is degenerate [79]. From simulation, these thickness values were obtained to be ∼6.1 nm and ∼4.4 nm for the thick and thin GaN heterostructures, respectively, which can be used to obtain the 2DEG conductivity σ from the sheet resistance (R_{sh}) extracted via CTLM measurements. Finally, we note that an average 2DEG volumetric density can be estimated as $n_v = \frac{n_s}{t_{2D}}$ for the thick GaN (1.73×10^{19} cm^{-3}) and thin GaN (2.07×10^{19} cm^{-3}) heterostructure. We note that the higher n_v for the thin GaN sample reflects the smaller 2DEG quantum well thickness.

3.1.8 Electrical and Thermal Property Measurements

The measurements of R_{sh} averaged over four samples up to 300°C via CTLM measurements can be combined with the 2DEG thickness t_{2D} to obtain the average electrical conductivity [$\sigma = \frac{1}{R_{sh} t_{2D}}$] of the electrons in the 2DEG. At room temperature, we obtained R_{sh} values of ∼350 Ω·sq^{-1} and ∼500 Ω·sq^{-1} for the thick and thin GaN samples, respectively. We note that these values are amongst the lowest reported R_{sh} values for AlGaN/GaN 2DEGs, which highlights the quality of our samples [50]. The average conductivity in the thin GaN sample is observed to be similar to the thick GaN sample due to simultaneous reduction in the sheet density and quantum well depth, as seen in Figure 3.12a. Sheet densities in this temperature range are approximately constant due to negligible strain relaxation in the heterostructure layers [68], stable piezoelectric coefficients [92], and minimal intrinsic carrier concentration change due to the wide-bandgap. Thus, the decrease of σ at high temperatures is mainly determined by the 2DEG mobility, μ. The dependence is well described by a temperature power law $\sim T^{-2.5}$ that arises from electron-optical phonon scattering, which further supports this fact. We also note that our exponent is consistent with former exponent ranges (from -2.2 to -3.4) reported in the literature [68]. Temperature dependent in-plane thermal conductivity measurements for the thick and thin GaN samples are shown in Figure 3.12b. Room temperature thermal conductivity dropped from ∼115 W·m^{-1}K^{-1} for the thick GaN sample to ∼45

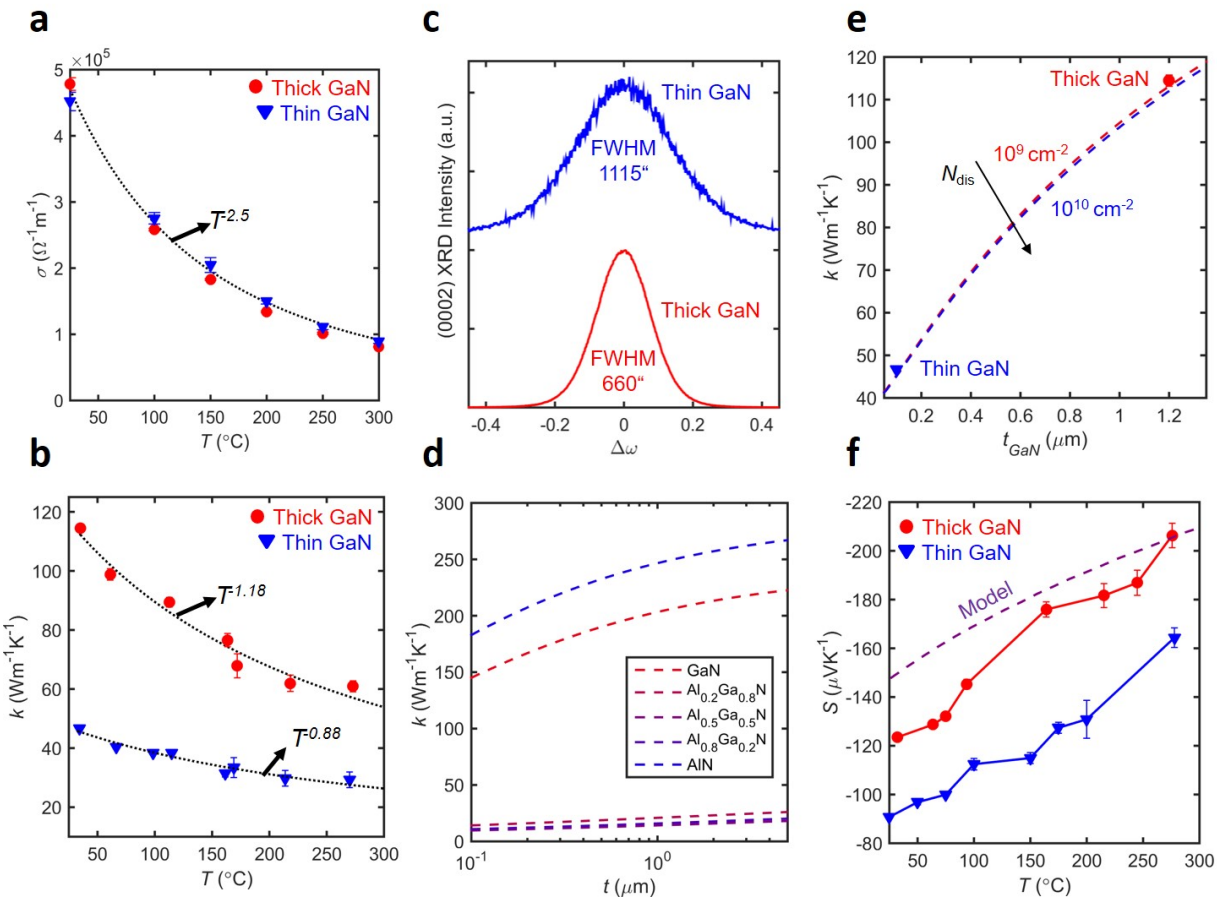

Figure 3.12: (a) Temperature dependent electrical conductivity of the 2DEG for the thin and thick GaN samples, extracted via CTLM measurements. (b) Temperature dependent thermal conductivity measurements for the thick and thin GaN samples. Fits are shown with black, dotted lines. (c) XRD rocking curve scan of the (0002) lattice plane in GaN, to investigate the density of screw-type dislocations. (d) Modeled in-plane thermal conductivities of the layers in our composite stack as a function of thickness using a dislocation density of 10^9 cm^{-2}. (e) Thermal conductivity reduction due to size effect at 25°C. The model corresponds to the dashed lines with increasing dislocation densities (N_{dis}) and the data points are the experimental measurements. (f) Measured Seebeck coefficient versus temperature for thin and thick GaN samples. The model uses $n_v \approx 2{\times}10^{19}$ cm^{-3}, which is estimated from the Schrödinger-Poisson simulation. ©2018 Wiley.

W·m^{-1}K^{-1} for the thin GaN sample due to phonon boundary scattering, i.e. the size effect [82]. The measurements for the thick GaN sample follow a $T^{-1.18}$ fit. This is consistent with a similar temperature exponent observed in measurements of cross-plane thermal conductivity measurements of GaN films of thickness of ~0.7 µm [80, 93]. However, for the thin GaN sample, we note that the measured thermal conductivity values follow a T$^{-0.88}$ fit, indicating that Umklapp scattering is less

prominent for long wavelength phonons which are suppressed due to size effect.

In-plane thermal conductivity data in these films are limited, with little data available on the size effect and temperature dependence [80]. Since our suspended film is a composite consisting of an AlN layer, $Al_xGa_{1-x}N$ transition layers and a GaN layer, the overall thermal conductivity (k) can be estimated as $\frac{\sum k_i t_i}{\sum t_i}$, where k_i and t_i refer to the thermal conductivities and thicknesses of individual layers. For each multilayer, we used a Boltzmann Transport Equation (BTE) model to quantify k_i with layer thickness (t_i). Using a simple Debye approximation for the phonon dispersion with an average velocity over the acoustic phonon modes (v_{ac}), the in-plane thermal conductivity for each layer can be written as [94]

$$k_i = \frac{3k_B^3T^3}{8\pi^3\hbar^3v_{ac}^3}\int_0^{\theta_D/T}\int_0^{2\pi}\int_0^{\pi} c_{ph}\sin(\theta)\tau_C(x)x^2v_g^2 d\theta d\phi dx \tag{3.7}$$

where k_B is the Boltzmann constant, θ_D is the Debye temperature for the multilayer [77], T is the temperature, $\hbar$ is the reduced Planck's constant, c_{ph} is the mode specific volumetric heat capacity, evaluated as $3k_B\frac{T^3}{\theta_D^3}\int_0^{\theta_D/T}\frac{x^4e^x}{(e^x-1)^2}dx$ and $x = \frac{\hbar\omega}{k_BT}$. Here, ω is the phonon frequency. The integration is performed over the angular directions (θ and ϕ) using a direction dependent group velocity $v_g = v_{ac}\sin(\theta)\cos(\phi)$.

The total scattering time τ_C is calculated by Mathiessen's rule with contributions from Umklapp (τ_U), impurity (τ_I), alloy (τ_A), boundary (τ_B) and defect scattering (τ_D), respectively. The Umklapp scattering term is evaluated via the Callaway relationship, $\tau_U = \frac{A}{\omega^2}$. We evaluated constant A in the bulk limit as $\frac{2\pi^2v_{ac}k_\infty}{c_{ph}\omega_D}$, where k_∞ in the bulk thermal conductivity of layer and ω_D is the Debye frequency. For instance, k_∞ values of 240 $W{\cdot}m^{-1}K^{-1}$ and 285 $W{\cdot}m^{-1}K^{-1}$ are used for GaN and AlN at room temperature, respectively [95, 96]. The Debye frequencies are extracted from the known Debye temperatures of these material layers [77]. Scattering with impurities is neglected since its effect is found to be negligible for unintentionally doped films [95]. For the underlying transition layers, all the material parameters (e.g. v_{ac}, θ_D, k_∞) are averaged over the AlN and GaN fractions, in context of the virtual crystal model [97]. Alloy scattering severely reduces the thermal conductivity of the transition layers and is evaluated as a point defect scattering term [98]. For the sake of brevity, we skip the details, which can be found in Liu et al. [97]. The defect scattering term (τ_D) included core, screw, edge and mixed dislocations with total density N_{dis}, whose effect is to reduce the thermal conductivity [98].

Although we have a composite film (and thus, the dislocation density is expected to vary for the different layers), we estimated an average value for the composite film via X-Ray Diffraction (XRD)

measurements. For example, Figure 3.12c shows symmetric (rocking curve) scans of the (0002) lattice planes in the thin and thick GaN samples. Using the full width at half maximum (FWHM, denoted by β) value of the XRD scans, the screw-type dislocation density can be estimated as $\approx \frac{\beta^2}{4.35c^2}$, where c is the lattice constant (0.5185 nm) along the c-axis direction for the GaN wurtzite crystal [48]. Using this, we calculate the screw-type dislocation density to be $\approx 9\times10^8$ cm^{-2} and $\approx 2.5\times10^9$ cm^{-2} for the thick and thin GaN samples, respectively. An estimate of the edge-type dislocation density from XRD measurements is shown in Figure 3.13a, also in the order of 10^9 cm^{-2}. Finally, the direction-dependent boundary scattering term [94] is evaluated as $\tau_B = \frac{t_i}{2v_{ac}|\cos(\theta)|}$. The modeled in-plane thermal conductivities of the individual layers in the composite stack are depicted in Figure 3.12d as a function of the corresponding layer thickness. Due to the lack on in-plane

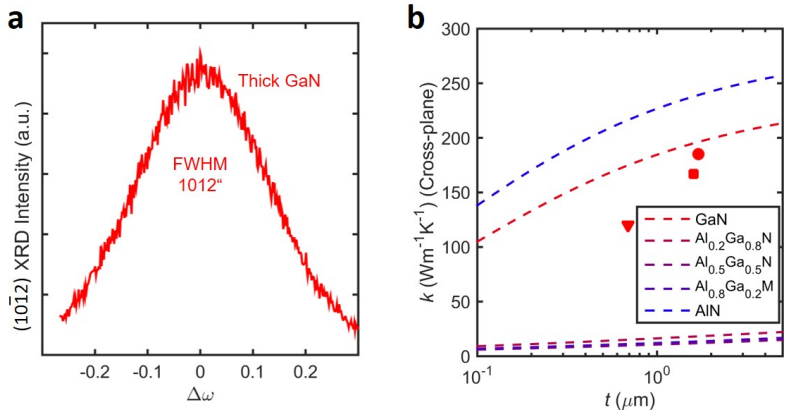

Figure 3.13: (a) XRD scan to estimate the density of edge-type dislocations in the thick GaN sample. The edge type dislocation density is estimated as $\sim3\times10^9$ cm^{-2} following the methods described in elsewhere [48]. (b) Cross-plane thermal conductivity estimates of the layers in our composite film as a function of thickness. The experimental data points correspond to cross-plane measurements in GaN [93, 80]. ©2018 Wiley.

thermal conductivity data in these films, it is difficult to compare the model in Figure 3.12d with literature. However, an estimate of the cross-plane thermal conductivity [94] using the layers can be estimated using a different $v_g = v_{ac}\cos(\theta)$ in (3.7), the results of which are in Figure 3.13b, showing good agreement with previous measurements. Using the thicknesses of the multilayers (Figure 3.2), the overall in-plane thermal conductivity of the composite stack (k) where the GaN buffer layer thickness (t_{GaN}) is varied (at room temperature) is shown in Figure 3.12e. In particular, we note that the model agrees with the experimental data well, and that dislocation densities in our range (10^9 – 10^{10} cm^{-2}) are estimated to have little effect on thermal conductivity of the film

layers. In other words, the in-plane thermal conductivity reduction from the thick GaN to the thin GaN composite stack is expected to arise almost exclusively from the size effect. We note that this observation is consistent with former reports of the cross-plane thermal conductivity in GaN films with similar dislocation densities [97, 99].

The measured Seebeck coefficients for the thick and thin GaN heterostructures are shown in Figure 3.12f. While the Seebeck coefficients for thick doped III-V films have been reported in the past [43, 76, 77], values for a polarization induced 2DEG have not been well studied in literature. The approximate linear increase in the Seebeck coefficient with temperature indicates a degenerate semiconductor that may be well approximated with a Cutler-Mott [100] formula for nearly free electrons. Since $R_{buffer} \gg R_{2DEG}$, the measured values can be considered to arise exclusively from the 2DEG [60], which is in agreement the degenerate semiconductor characteristic. To understand the magnitude and the observed dependencies with temperature, we implemented a simple analytical model based on Sztein et al [77]. For a bulk doped material with fixed electron concentration, the Seebeck coefficient is analytically evaluated as (following Chapter 2)

$$S = -\frac{\int (E - E_F)\sigma(E)dE}{qT \int \sigma(E)dE} \tag{3.8}$$

where $\sigma(E)$ is the differential electronic conductivity, q is the fundamental charge, E is the electron energy and E_F is the Fermi energy.

Following Sztein et al. [77], we evaluated S as a function of doping densities in GaN. The model for the Seebeck coefficient shows good match with measurements for doped GaN films (Figure 3.15a). These doping densities only serve to "mimic" the effect of 2DEG charge density, since the origin of the 2DEG is related to built-in polarization fields as discussed earlier. The differential electronic conductivity is evaluated using a non-parabolic energy dispersion relation and typical scattering mechanisms found in III-nitrides: optical phonon, piezoelectric, deformation potential and charged dislocation scattering [77]. The parameters and assumptions in the model follow from Sztein et al. [77], with the notable exception that we neglected ionized impurity scattering in the evaluation of $\sigma(E)$, since the 2DEG region is assumed to be undoped. In principle, the Seebeck coefficient for the 2DEG region can be evaluated by discretizing it into fine regions with approximately constant charge concentration using (3.8) via a thickness average. For simplicity, we instead compare the average volumetric density n_v for the 2DEG region that we obtained by calculating the average charge density $\frac{n_s}{t_{2D}}$ against the simulated Seebeck coefficients for "mimic" doping densities. The predicted Seebeck coefficient dependence using n_v ($= 1.73\times10^{19}$ cm^{-3}) is in good agreement with

the measured values for the 2DEG for the thick GaN sample, as illustrated in Figure 3.12f. However, the Seebeck coefficient values for the thin GaN sample are lower than the thick GaN sample, which could arise from a larger n_v ($= 2.07\times10^{19}$ cm^{-3}) due to reduced 2DEG thickness and differing relevance of scattering mechanisms (e.g., greater dislocation scattering) in comparison the thick GaN film.

Finally, we also note that our measured values for the AlGaN/GaN 2DEG Seebeck coefficients do not show a similar enhancement in comparison to a bulk 3D Seebeck coefficient, which is unlike other systems, such as ZnO based 2DEG [101]. This could arise from the relatively large 2DEG confinement thickness (t_{2D}) of ∼5 nm in our structures, as opposed to much smaller confinement depths (∼1 nm) in the ZnO based 2DEG [101]. Nonetheless, our results show that tuning the thermal transport while maintaining the electrical transport via buffer layer engineering can be achieved and is useful for the design of AlGaN/GaN devices.

3.1.9 Applications

The measured electrical, thermal, and thermoelectric properties could be important for a variety of GaN-based temperature, power electronics, heat-flux, magnetic field and energy harvesting devices using III-V heterostructures. As an example, we demonstrate how the measured electrical and thermal properties could be used to detect local temperatures from on-chip heat loads using the fully-suspended thick GaN platform. Figure 3.14a shows an on-chip circuit with four resistive heat sources (similar to the heater and sensor metal electrodes) with six 2DEG mesa regions (spanning the suspension and substrate regions) across which the Seebeck voltage can be measured. The substrate is held at 25°C using a temperature controlled probe-station. We then apply a heating power (25 mW) to induce a temperature gradient relative to the substrate in the suspended heterostructures. The simulated temperature profile for a quarter region using the measured thermal properties and external losses is shown in Figure 3.14b. Three sample locations of the "hot" ends of the 2DEG mesa where temperature is measured are illustrated in Figure 3.14b. Finally, with the heater power held constant, we measured the differential Seebeck voltage for the six 2DEG mesa regions. Using the measured temperature dependent Seebeck voltage for the thick GaN film, we extracted the temperatures at the hot ends of the 2DEG mesa regions and compared them with the simulated local temperatures from the finite element model. Excellent agreement is observed (within a maximum of ∼15% error), as seen in Figure 3.14c, which demonstrates how the measured properties could be used for local on-chip monitoring of thermal loads in addition to validating our measurements.

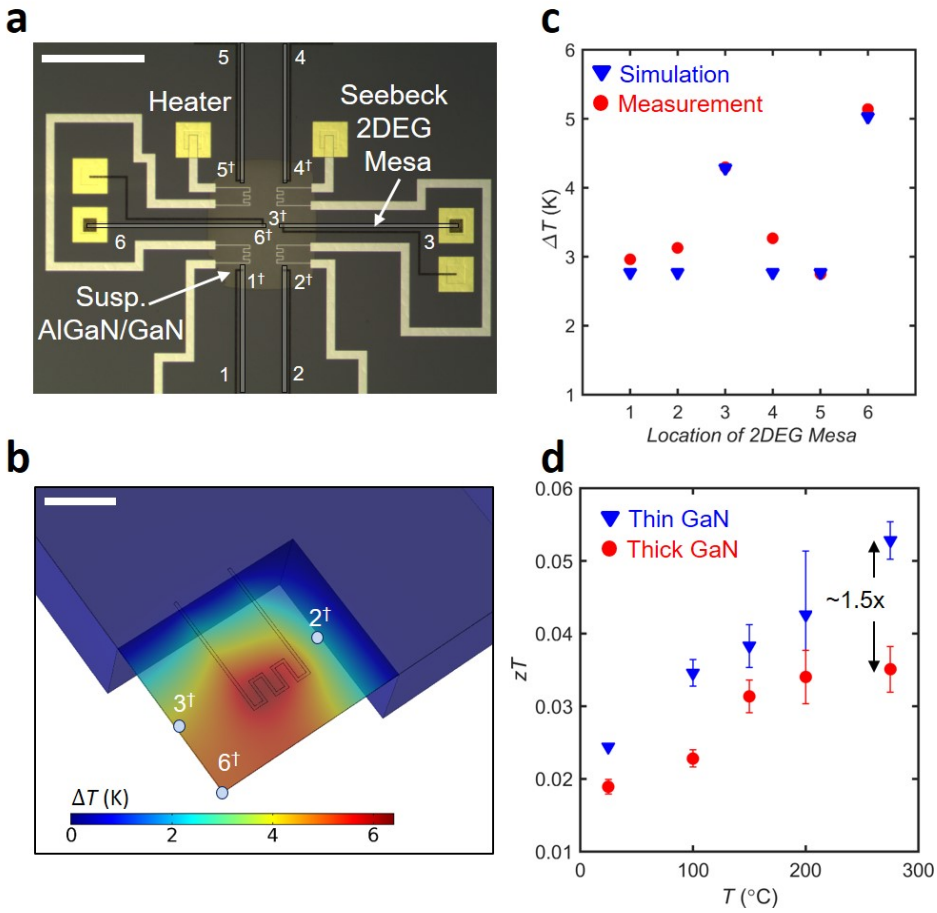

Figure 3.14: (a) Fully-suspended platform to measure local temperature rise using the thick GaN heterostructure. The six labelled AlGaN-GaN Seebeck 2DEG mesa regions (e.g., 2-2†, shaded white for clarity) can be used to estimate temperature rise near the heater line, which mimics a power device. Note that the temperatures are measured at the "hot" ends of the mesa regions, marked by a † symbol. (b) Finite element model of temperature rise with a heater power of 25 mW using the extracted thermal properties of the thick GaN sample. The model is for a quarter symmetry region of Figure 3.14a. Three locations for temperature rise measurement (2†, 3†, 6†) are also shown. The Si substrate is assumed to be at 25°C in this model. (c) Simulated and experimentally determined temperature rise at locations. The measured temperatures are noted to be accurate to within 15%. We used the measured Seebeck coefficient of the thick GaN sample to extract the temperature rise. (d) Measured thermoelectric figure of merit (zT) for thin and thick GaN samples, showing steady rise with temperature. An improvement of ∼22 to 51% is noted for the thin GaN sample over the thick GaN sample over the temperature range. Scale bars of (a), (b) 500 µm, 100 µm. ©2018 Wiley.

Finally, Figure 3.14d shows the temperature dependent thermoelectric figure of merit (zT) up to ∼300°C using the measurements of 2DEG electrical conductivity, Seebeck coefficient and in-plane

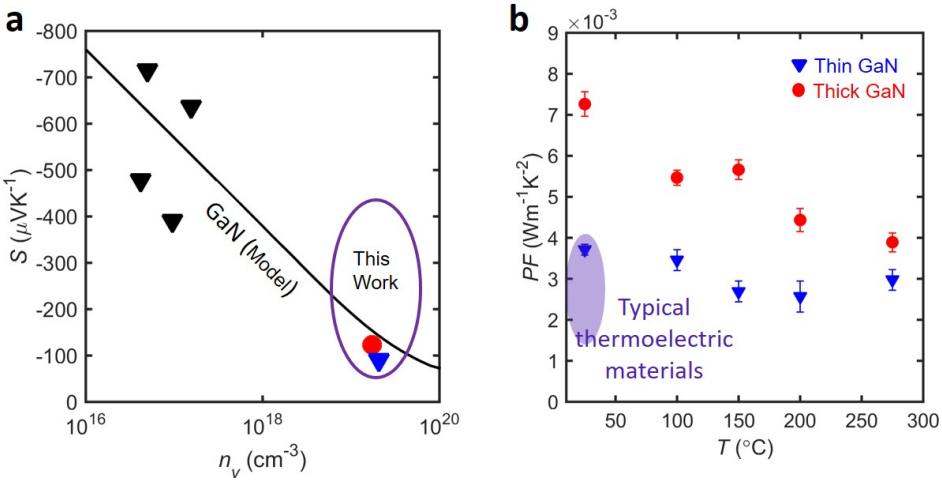

Figure 3.15: (a) Room temperature Seebeck coefficients (S) as a function of carrier concentration (n_v) in GaN. The black line represents the Seebeck coefficient model. The experimental data points [79, 102, 103] and the model are at room temperature. All the data points correspond to doped, bulk films. The measured values for the 2DEG in the thick and thin GaN sample in this work are also plotted. (b) Power factor of the 2DEG in the thin and thick GaN samples. The power factor for state-of-the-art thermoelectric materials is usually between 1.5×10^{-3} and 4×10^{-3} W·m^{-1}K^{-2} at room temperature [81]. ©2018 Wiley.

heterostructure thermal conductivity. These zT values are 3 to 4x higher than in bulk doped GaN films [77], owing to large 2DEG conductivities and thermal conductivity reduction from size effect. Further, we notice that the thin GaN film displays almost ∼22-51% higher zT values in comparison to the thick GaN film due to the large, ∼2.5x decrease in the in-plane thermal conductivity. The trend with temperature is almost linear, which is different from the super-linear trend [77] observed for doped III-V films, due a greater temperature exponent for the 2DEG mobility. Since the background doping concentration is low ($<10^{16}$ cm^{-3}) and the layers used are wide band gap materials, it is expected that the thermopower peak occurs at much higher temperatures [77] in comparison to doped III-V films, which warrants further investigation of these properties beyond 300°C. Apart from the thermoelectric figure of merit, the 2D electron gases in these films also show very high power factors between 4-7$\times10^{-3}$ W·m^{-1}K^{-2} at room temperature (Figure 3.15b), which is comparable to the values for state-of-the-art thermoelectric materials [81]. These observations suggest that this approach of engineering the heterostructure layers in conjunction with polarization-based 2DEGs has promising potential for thermoelectric applications at high temperatures.

3.1.10 Conclusion

In this section, we described the design and implementation of a suspended AlGaN/GaN heterostructure platform to investigate temperature dependent thermal and electrical transport of by tuning the GaN layer thickness. We have demonstrated effective manipulation of these properties, and in the process shed light on several transport parameters that have not been previously explored in detail in former literature. Notably, our results show that thin GaN layers of ∼100 nm significantly impede heat flow, but preserve the 2DEG conductivity, which could be useful for a range of GaN-based devices. The state-of-the-art power factors are also promising for making micro-thermoelectric generators. We also showed a simple example of how the measured properties can be used to monitor local heat fluxes on an AlGaN/GaN power device. We used a single AlGaN barrier layer in this study, which could serve as a backbone for extension to multiple, alternating GaN/AlGaN superlattice layers. Further work along these lines could include how changing the AlGaN thickness affects transport, improving the temperature dependent mobility degradation in AlGaN/GaN 2DEGs, exploring transport at higher temperatures beyond 300°C, and exploring thermoelectric phenomena in other III-V heterostructure families with 2DEGs using this experimental platform.

3.2 Geometry-Based Enhancement of Thermoelectric Properties

As previously discussed in Chapter 2, power density optimization is important for micro-thermoelectric generators, as it leads to higher power output per unit area. Improvement in material properties (such as the thermoelectric power factor) is one approach to increase power density. An alternate approach, is to use 3D, folded surfaces to keep the footprint same but increase the power density. Such folded surfaces are routinely used in the field of photonics [104, 105], for example, to improve light collection efficiency from solar cells. However, such ideas have not be explored in the context of thermoelectrics. In this section, we describe an enhancement of thermoelectric performance of AlGaN/GaN films grown on inverted pyramidal silicon (Si) substrates as compared to films grown on flat Si substrates. It must be noted that the films used in this section have non-negligible doping in the buffer, unlike the previous section. We found that the magnitude of the Seebeck coefficient at room temperature increased from ∼297 μV·K^{-1} for flat film to ∼849 μV·K^{-1} for the film on inverted pyramidal Si. In addition, we observed an increase in the "effective" electrical conductivity of the AlGaN/GaN film on inverted pyramidal structure because of a unique combination of series and

parallel resistances along the 2DEG path. These changes contributed to a significant improvement in the thermoelectric properties of AlGaN/GaN multilayers on three-dimensional (3D) pyramidal surfaces relative to the flat geometry. Portions of this section can also be found in our paper [106].

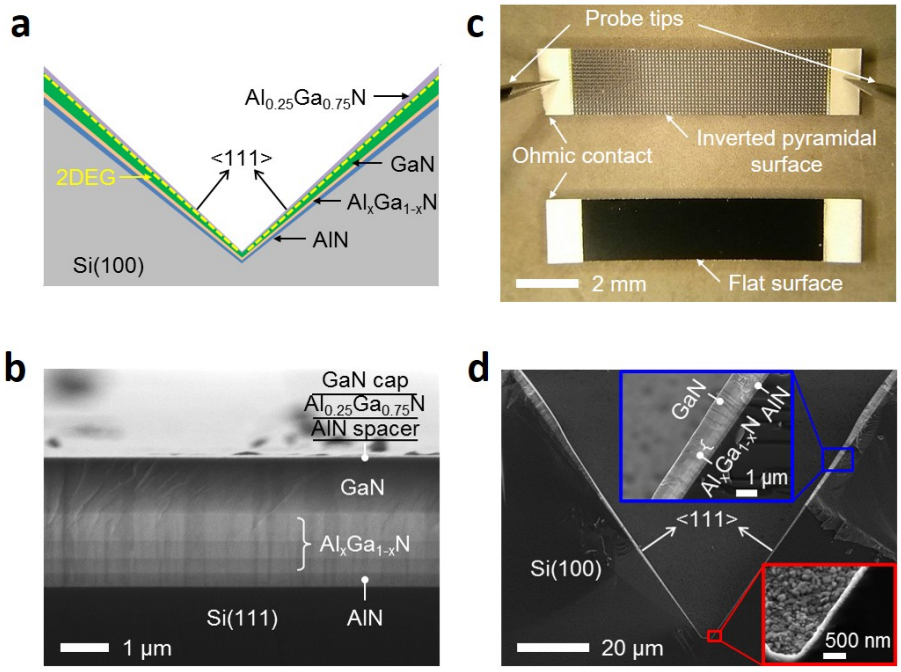

Figure 3.16: (a) Schematic of pyramidal heterostructure, showing the different layers and geometry-induced tapering of film thickness. (b) Optical images of long strip-type devices for current-voltage and Seebeck coefficient measurement experiments. An array of pyramidal structures can be seen on the surface of the pyramidal strip. (c) SEM images of the multilayered AlGaN/GaN layers grown using a MOCVD process on flat Si(111) substrate and (d) on inverted pyramidal Si substrate with zoomed-in view at different locations along the (111) surface. ©2017 AIP.

3.2.1 Fabrication

The flat AlGaN/GaN films were grown on Si(111) substrate, while Si(100) substrate whose (111) surfaces were exposed using potassium hydroxide (KOH) was used for the inverted pyramidal films [107]. Figure 3.16a shows a schematic of the pyramidal film that was grown in this study. To provide temperature gradient for the measurement of current-voltage response and Seebeck coefficient, we fabricated long, strip-type samples of AlGaN/GaN on both flat and inverted pyramidal Si substrates, as shown in Figure 3.16b. In both cases, the p-type Si substrates had similar resistivity of 0.1–1 Ω·cm. An in-house metal-organic chemical vapor deposition (MOCVD) process was used to deposit

AlGaN/GaN on the buffer layers. To eliminate batch-to-batch process variation, the MOCVD process was performed at the same time (in the same chamber) for both the flat and pyramidal samples. Details of the microfabrication of the AlGaN/GaN on inverted pyramidal Si surface can be found in our previous work [107]. In this study, the MOCVD recipe was carefully controlled to deposit ∼30 nm of $Al_{0.25}Ga_{0.75}N$ barrier layer on the GaN layer. A thin GaN capping layer of ∼3 nm was grown on top of the AlGaN barrier layer, and a 1 nm thick AlN spacer layer was inserted between the AlGaN and the GaN layers [83, 108]. Figures 3.16c and Figures 3.16d show a scanning electron microscope (SEM) image of the multilayers grown on flat and inverted pyramidal Si substrates, respectively. In comparison to the AlGaN/GaN multilayers on the flat substrate, each layer on the inverted pyramidal Si substrate tapered from the upper to the lower part of the pyramidal geometry [107] because of a reduction in mass transfer of the precursor gases in the cavities [109, 110, 111, 107]. Therefore, the AlGaN barrier layer tapered down from its initial value (∼30 nm) towards the bottom of the pyramidal structure. In this case, the 2DEG, which is formed at the AlGaN/GaN interface, is present along the contours of the inverted pyramid, giving rise to a 3D electrical conduction path [107]. Because the mass transfer rate for AlN is greater than that of GaN [Figure 3.16d], it should be noted that the buffer layers at the bottom of the pyramidal geometry are AlN-rich, as are shown in the inset of Figure 3.16d. This is also confirmed by performing energy-dispersive X-ray spectroscopy (EDS) along the slope of the pyramidal surface, as seen in Figure 3.17.

3.2.2 Band Diagrams

Figure 3.18a shows a simulated energy band diagram of the multilayers used in our study (i.e., GaN capping/AlGaN barrier/AlN spacer/GaN layer), obtained using a Schrödinger-Poisson solver (NextNano GmbH) [55]. The volumetric charge density, n_v, throughout the thickness of the device structure was also calculated. To calculate the 2DEG density, all the material layers were assumed to be undoped, and the barrier height at the GaN capping surface was set to 1 eV because the GaN surface was exposed to air [56]. Figure 3.18b shows that charge density, n_v, is concentrated in a thin ∼5 to 10 nm region near the AlGaN/AlN/GaN interface because of built-in polarization fields in these layers, creating the 2DEG [51, 112, 92]. The physical thickness of this region, t_{2D}, can be defined as the region in which GaN is degenerate (i.e., the conduction band, E_C, is below the Fermi energy, E_F, of the system) [79]. If the charge profile is assumed to be triangular, the average volumetric charge density can be defined as $n_v = \frac{n_s}{t_{2D}}$ [79], where n_s is the 2DEG sheet density. The 2DEG density, n_s, at room temperature was estimated to be ∼1.06 $\times 10^{13}$ cm^2 from

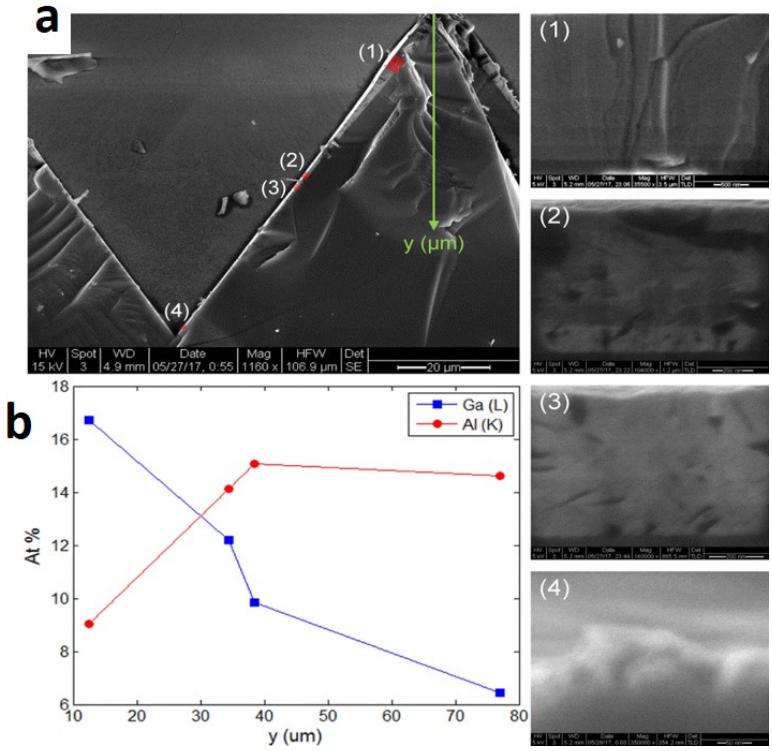

Figure 3.17: (a) SEM image of the multilayered AlGaN/GaN films on inverted pyramidal Si substrate with (1-4) zoomed-in view at different locations along the (111) surface. These locations and images were used for energy dispersive X-ray spectroscopy (EDS) analysis (EDAX Inc.) to identify the composition of the elements in films along the pyramidal surface. (b) Relative atomic ratio between Ga and Al at different locations (1-4). The other elements detected are not considered in the calculation. It should be noted that the heterostructure is Ga-rich in the upper portion, but gradually transitions to Al-rich towards the bottom. ©2017 AIP.

the Schrödinger-Poisson model. Using this, we obtained a n_v of $\sim 1.73 \times 10^{19}$ cm^3, with $t_{2D} \approx 6.1$ nm from the simulated band-structure for the flat sample.

3.2.3 Results and Discussion

To understand the thermoelectric enhancement, we first focus on the current increase in the 2DEG of the pyramidal structure compared to the flat structure due to the geometrical effect. Simplified analysis of the electrical resistance (R) between the devices on the flat and inverted pyramidal surfaces assuming identical thickness of current conduction layers and electrical conductivities to be σ^F and σ^P, respectively, can be found in our former work [107]. It should be noted that the

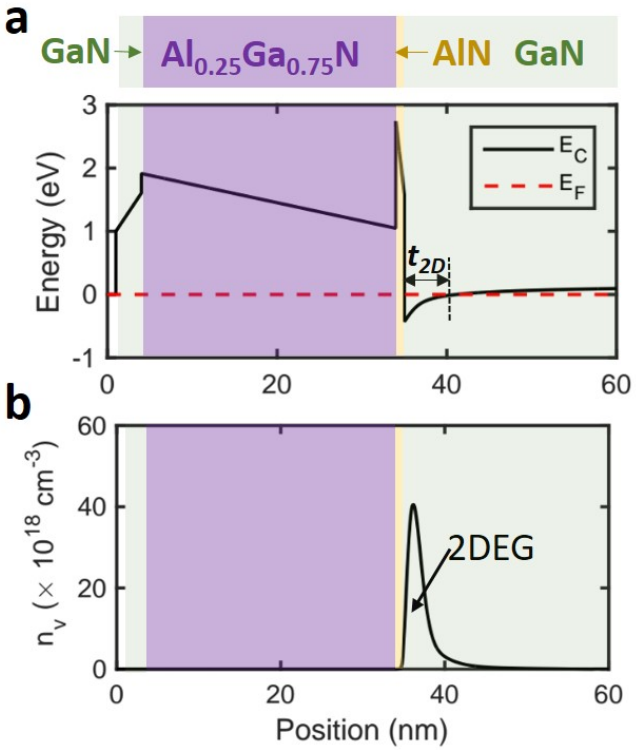

Figure 3.18: (a) Simulated energy band diagram for the flat device with AlGaN thickness set to 30 nm. The thickness of the 2DEG region, t_{2D}, is shown in the region where GaN is degenerate. (b) Volumetric charge density, n_v, versus position, depicting the approximately triangular charge profile. ©2017 AIP.

network of resistances in the inverted pyramidal structure gives $\frac{R^P}{R^F} = G \times (\frac{\sigma^F}{\sigma^P})$, where G is a geometry-enhancement factor. We previously estimated $G^{model} \approx 0.52$ analytically when $\sigma^F = \sigma^P$ [107], which means that the resistance of the pyramidal structure is predicted to be about half of the flat structure resistance, assuming the electrical conductivities are identical. Note that the lower resistance for the pyramidal sample arises due to the larger cross-sectional area of the pyramidal surfaces in comparison to the flat sample. In order to verify whether the analytical prediction (G^{model}) is valid for the strip-type samples used in this study, we measured the resistance of the flat and pyramidal devices. The measured resistances along with their current-voltage curves are shown in Figure 3.20a, with $R^P \approx 1743\ \Omega$, $R^F \approx 3018.9\ \Omega$, and thus $G^{expt} \approx 0.58$. While the current is assumed to largely flow through the 2DEG thickness t_{2D}, some contribution from the buffer layers can be also expected. It should be noted that G^{expt} value is slightly higher than the

geometry-enhancement factor of 0.52 (G^{model}) obtained from the network resistance analysis [107]. This means that the pyramid device has slightly higher resistivity than the flat device in the region where current flow occurs. The reason behind this follows from a simple, analytical model for the 2DEG sheet density n_s as follows [112, 113, 114, 115]:

$$n_s = \frac{\sigma}{q} - \frac{\epsilon_{AlGaN}}{q t_{AlGaN}} \left[\phi_b - \frac{\Delta E_C}{q} \right] \tag{3.9}$$

where σ is the polarization charge density at the AlGaN/GaN interface, q is the electron charge, ϵ_{AlGaN} is the permittivity of the AlGaN layer, t_{AlGaN} is the thickness of the AlGaN barrier layer, ϕ_b is the barrier height at the AlGaN surface, and ΔE_C is the heterojunction band offset for AlGaN/GaN. Because of the inverse, non-linear dependence on t_{AlGaN} in (3.9), it is found that n_s increases over a magnitude from $\sim 10^{12}$ cm^2 to $\sim 10^{13}$ cm^2 as the AlGaN thickness varies from 5 to 10 nm [56, 116], and then asymptotes as the AlGaN thickness increases. In this study, because the AlGaN thickness was found to taper towards the bottom of inverted pyramidal structure, the 2DEG sheet density varies locally within a pyramidal unit cell [107], with a lower 2DEG density at the bottom of the pyramidal structure in comparison to the upper area of the structure. This implies that the electrical conduction in the upper regions of the inverted pyramidal structure could arise from the 2DEG and buffer layers, while the dominant conduction in the lower part could arise from the buffer layers, which explains the slightly higher G^{expt} in comparison to G^{model}. We now discuss the measurement of the Seebeck voltage in both structures. For the measurement of Seebeck coefficient, each end of the sample was attached to a heater (S-1060, Signatone, Inc.) and heat sink using thermal grease to ensure a good thermal contact. Along with the Seebeck voltage, the temperature gradient was simultaneously measured using thermocouples on both the hot and cold side. An image of the experimental setup is shown in Figure 3.19. Figure 3.20b shows the measured Seebeck voltage for the AlGaN/GaN layers on the flat and inverted pyramidal substrate as a function of the temperature gradient between the hot and cold side (ΔT). The Seebeck voltage was observed to be linearly increasing with ΔT, giving rise to Seebeck coefficients of -296.6 μV·K^{-1} for flat device (S^F) and -848.4 μV·K^{-1} for inverted pyramidal device (S^P). These coefficients are valid at room temperature and are negative, consistent with the presence of a 2DEG in both the flat and pyramidal devices. Since both the (111) and (100) substrate types were co-deposited in the MOCVD chamber, similar doping (unintentionally) levels are expected. In addition, the expected temperature gradient, ΔT, is the same for each device. Therefore, we attribute the $\sim$2.86$\times$ enhancement to the geometry-induced properties of the pyramid sample in comparison to the flat sample. To further investigate

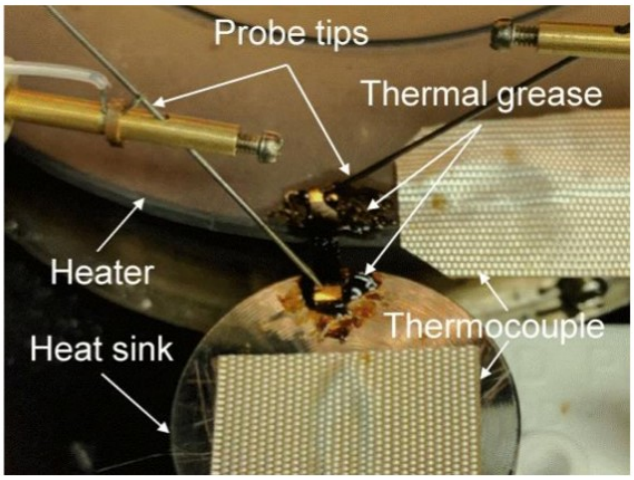

Figure 3.19: Experimental setup for Seebeck voltage measurement. The sample was firmly suspended across a heater and heat sink. Thermal grease (Apiezon Inc.) was used to ensure good thermal contact. The temperature at both ends was measured using a self-adhesive K-type thermocouple (OMEGA Eng.). ©2017 AIP.

the geometry effect on enhanced Seebeck coefficient, a theoretical model based on the work of Sztein et al [77]. for the Seebeck coefficients of AlN and GaN with respect to carrier concentration was implemented. The results from this model are plotted along with former experimental measurements [79, 103, 102, 78] in Figure 3.21. The scattering time of electrons is calculated using contributions from acoustic phonon, polar optical phonon, piezoelectric polarization, and charged dislocation components [77]. For charged dislocation scattering, the dislocation density is set to 10^9 cm^2, which is typical for GaN films [98, 117]. Good agreement with experiments was observed for GaN. However, previously measured values (∼-1000 μV·K^{-1}) for metal-organic vapor phase epitaxy (MOVPE) grown AlN samples are higher than the theoretically predicted values which might be due to hopping conductance, as suggested by former researchers [78, 118]. The measured Seebeck coefficient of the flat sample corresponds to the open circuit voltage in Figure 3.22a and can be expressed as [79]:

$$S^F = \frac{S^{2DEG}R^{Buffer} + S^{Buffer}R^{2DEG}}{R^{Buffer} + R^{2DEG}} \tag{3.10}$$

which includes contributions of the 2DEG region and buffer layers, as shown in Figure 3.22a. Here, R^{Buffer} and R^{2DEG} refer to the resistances of the buffer layers and the 2DEG region, respectively. Using the 2DEG concentration from the Schrödinger-Poisson model, n_v, of ∼1.73 ×10^{19} cm^3 and the Seebeck coefficient model for GaN (Figure 3.21), S_{2DEG} was estimated to be approximately

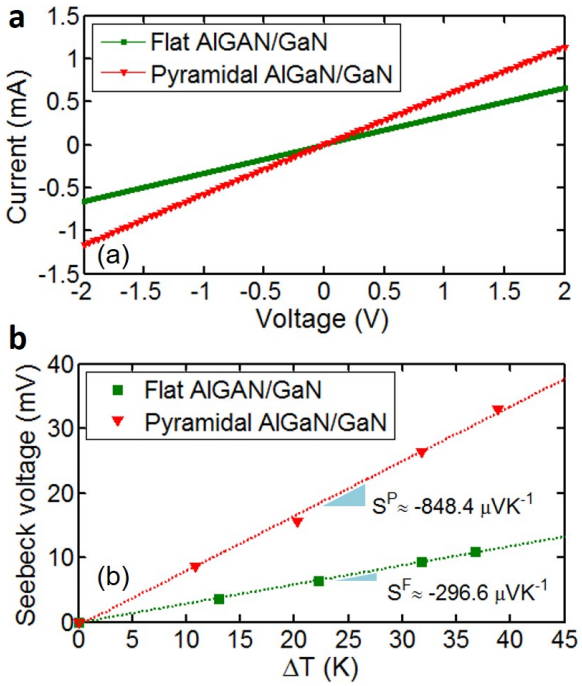

Figure 3.20: Comparison of (a) current-voltage response and (b) Seebeck voltage of AlGaN/GaN thin films on conventional flat silicon substrate and inverted pyramidal silicon substrate. Using a linear fitting curve, approximate Seebeck coefficients of -296.6 μVK^1 and -848.4 μVK^1 were obtained for AlGaN/GaN on flat and inverted pyramidal surfaces, respectively. ©2017 AIP.

-150 μV·K^{-1}, which is about half the measured Seebeck coefficient value of -296.6 μV·K^{-1} for the flat sample. To estimate R^{Buffer}, the 2DEG mesa was etched to a depth of ∼100 nm using an inductively coupled BCl_3/Cl_2 plasma for the flat sample. As a result, $\frac{R^{Buffer}}{R^{2DEG}} \approx 1.66$ was obtained based on the current-voltage measurement, corresponding to $S^{Buffer} \approx$ -540 μV·K^{-1} from (3.10). This implies an average buffer carrier concentration of ∼10^{17} cm^3 in the flat sample from the model for GaN as seen in Figure 3.21. For the AlGaN/GaN on inverted pyramidal surfaces, the measured Seebeck coefficient of -848.4 μV·K^{-1} might arise from a combination of location-dependent circuits, as depicted in Figure 3.22b. The Seebeck coefficient for the upper region of the inverted pyramidal AlGaN/GaN film might be similar to that of flat AlGaN/GaN film. However, because the 2DEG concentration decreases towards the bottom of the pyramidal shape (leading to $R^{2DEG} \gg R^{Buffer}$), the overall Seebeck coefficient could be dominated by the AlN-rich buffer layer, as shown in Figure 3.22b, which could explain the higher Seebeck coefficient. For the pyramidal film, the charged dislocation density in the lower, AlN-rich regions could be larger than the typical 10^9 cm^2, and

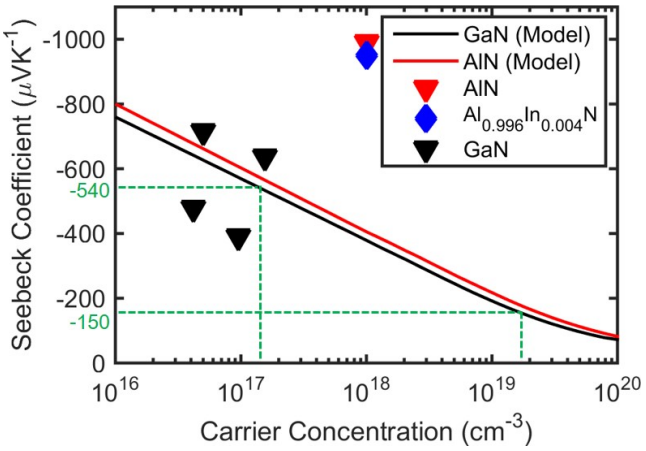

Figure 3.21: Experimentally observed [79, 103, 102, 78] and theoretically calculated (solid lines) Seebeck coefficients as a function of carrier concentration in GaN, AlN and related III-V alloys. For the data from Zhang et al. [78], carrier concentration was assumed to be $\sim 10^{18}$ cm^3 based on the other data in the paper. The Seebeck coefficients for GaN and AlN are calculated based on the model proposed by Sztein et al [77]. ©2017 AIP.

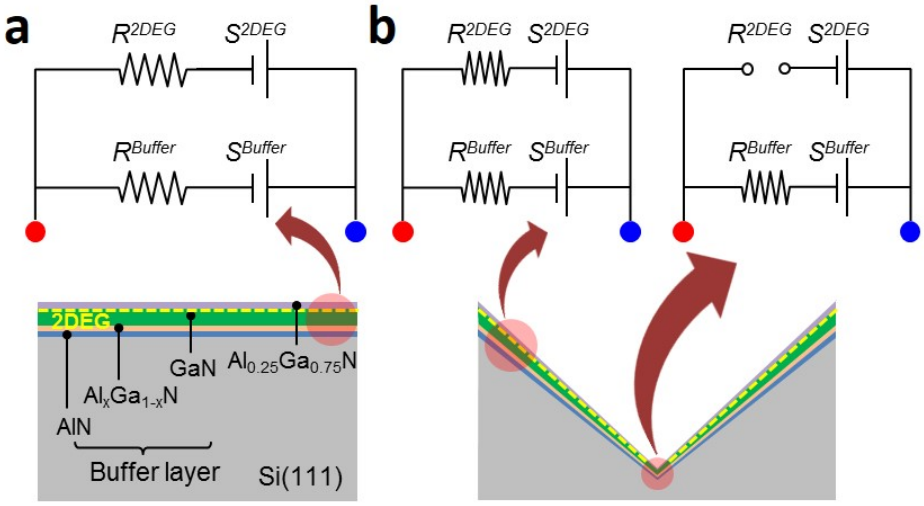

Figure 3.22: Schematic of the electrical circuit equivalent to (a) the AlGaN/GaN on flat Si(111) substrate and (b) AlGaN/GaN on inverted pyramidal Si(100) substrate indicating location-dependent electrical circuits due to tapered thickness of AlGaN/GaN multilayers. Note that the 2DEG at the bottom of the pyramid is expected to have a smaller charge concentration when compared to the top of the pyramid. ©2017 AIP.

thus partly responsible for the larger Seebeck coefficient observed. However, the increase from this effect is estimated to be small, as seen in Figure 3.23 and comparison with former experiments

[119]. In addition, it should be noted that the measured value (-848.4 μV·K^{-1}) is in agreement with the high Seebeck coefficient of ∼-1000 μV·K^{-1} for MOVPE grown AlN, as discussed earlier. The full benefit of the 3D structure is captured by evaluating the improvement in thermoelectric power factor. In doing so, we make the assumption that 2DEG and the buffer regions can be replaced by equivalent uniformly doped materials, and that the electrical conductivity (σ) improvement can be attributed to the geometry effect. With this assumption, we can write $\sigma^{P^*} \approx \frac{\sigma^F}{G^{expt}}$ where σ^{P^*} can be thought of as the "effective" conductivity of the pyramidal AlGaN/GaN film. As noted earlier, this is an approximation since the conducting buffer layers in the pyramid sample demonstrate thickness taper. In this case, the power factor ratio can be estimated as $(\frac{S^P}{S^F})^2 \times \frac{\sigma^{P^*}}{\sigma^F} \approx 14$. It should be noted that the power factor increases by ∼8 times even if the geometry enhancement on the conductivity is not considered. This represents an improvement in the power factor by the innovative use of 3D geometry. We emphasize that this power factor is only for a single 2DEG and buffer region, and to take full advantage of this approach, we would need to nanostructure periodic AlGaN/GaN/AlN/GaN superlattices to produce a continuous 2DEG along the normal direction to surface utilizing the pyramid architecture [65].

3.2.4 Conclusion

In this section, we demonstrated a strategy to improve the thermoelectric characteristics by growing AlGaN/GaN films on a folded pyramidal geometry. To further improve the thermoelectric characteristics, detailed investigation of the thermal conductivities must be conducted, as well as designing superlattice structures along the 3D geometry. This study motivates the use of the 2DEG as an integrated thermal sensing and harvesting element in III-V based power electronics platforms, and the use of 3D, folded geometries compatible with current CMOS technology [via the Si(100) substrate] to enhance thermoelectric performance for fixed device footprint.

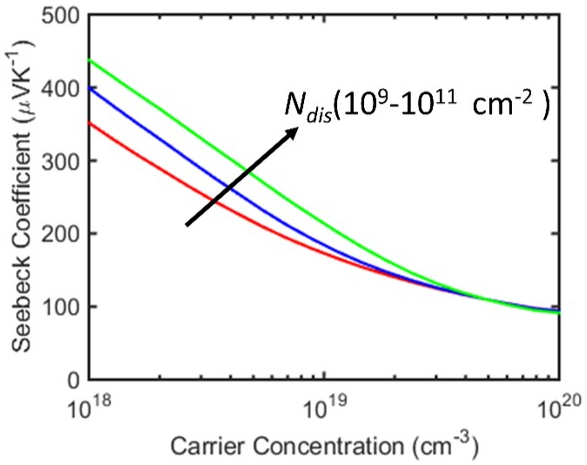

Figure 3.23: Magnitude of the Seebeck coefficient as a function of carrier concentration and dislocation density in a GaN film, based on the model by Sztein et al [77]. We varied the charged dislocation density parameter (N_{dis}) from 10^9 cm^{-2} (typical films [98, 117]) to 10^{11} cm^{-2} (extremely defective film [119]) within the model to estimate the Seebeck coefficient variation. It is seen, for example, that the Seebeck coefficient increases by ∼25% as the dislocation density varies from 10^9 to 10^{11} cm^{-2}. Similar results have been observed in InN films [119]. We note that the observed Seebeck coefficient increase for the pyramidal film over the flat film was over 180%. Thus, while dislocation density increase could be partly responsible for the higher Seebeck coefficient in the pyramidal film, we attribute the major cause to composition variation arising from the difference in the mass transfer rates of AlN and GaN. ©2017 AIP.

Chapter 4

Low Temperature Thermoelectric Transport

Apart from high temperature energy harvesting, another scenario where energy harvesting might be required is at low (cryogenic) temperatures. Thermoelectrics are usually not good at low temperatures because the Seebeck coefficient scales with temperature (and hence the power factor and the figure-of-merit). However, under certain conditions, a large enhancement in the thermoelectric performance can be obtained via electron-phonon interaction. In this chapter, we show experimental evidence of this effect in the AlGaN/GaN 2DEG, which can lead to promising low temperature thermoelectric properties.

4.1 Introduction

In modern semiconductor devices, the scattering of charge carriers by lattice vibrations, known as phonons, is an important bottleneck in the design of energy-efficient devices [120]. Yet, under a thermal gradient, commonplace in thermoelectric devices, these phonons can generate usable energy when they couple to charge carriers via an enhancement of the Seebeck coefficient (S) [121, 122, 123]. This momentum transfer to the charge carriers via non-equilibrium phonons, known as phonon drag (S_{ph}), supplements the thermal diffusion of charge carriers (S_d). Despite the potential gains in thermoelectric efficiency, understanding the contribution of phonon drag to the overall Seebeck coefficient has not received much consideration, largely due to early work which suggested that:

(1) S_{ph} is only significant at low temperatures (below $T \approx 50$ K), where the thermoelectric power conversion efficiency (zT) is low [124]; (2) S_{ph} is small relative to S for degenerate semiconductors [125, 126], which are common thermoelectric materials due to their large zT; and (3) an increase in S_{ph} coincides with a corresponding increase the thermal conductivity (k) [127, 128, 129], and thus has little benefit for power generation, since $zT \propto \frac{S^2}{k}$.

Contrary to these observations, recent experiments show that S_{ph} is almost 34% of the total S at room temperature in degenerate, bulk Si (doping on the order of 10^{19} cm^{-3}) [130]. Further, recent first-principles calculations show that different portions of the phonon mean free path spectrum (MFP, denoted by λ) contribute to thermal conductivity and phonon drag. Remarkably, this decoupling makes it possible to reduce k while preserving S_{ph} [123]. Though a detailed understanding of phonon drag can lead to advancements in solid-state thermoelectric power conversion, even at room temperature, there remain significant gaps in the literature. In particular, experiments which accurately quantify S_{ph} are yet lacking for low-dimensional systems. Degenerate 2D semiconductor quantum wells often have Seebeck coeffcients (S) and electronic conductivities (σ) which are enhanced relative to bulk [81, 131, 75, 65], increasing zT. Further improvements in thermoelectric performance necessitate understanding the contribution of S_{ph}.

Previous measurements of S_{ph} have been done in 2D electron gas systems by measuring the total Seebeck coefficient, theoretically estimating S_d, and calculating $S_{ph} = S - S_d$ [132]. However, estimating S_d is difficult to do because it needs precise knowledge of the scattering mechanisms for the charge carriers, in addition to the subband energies of the 2D quantum well. In the simple model by Herring [121], $S_{ph} \propto \lambda_{ph}$, where λ_{ph} is the MFP of the "representative" phonon that participates in drag. Thus, as shown in recent work on bulk Si [130], we can experimentally determine S and S_{ph} separately by varying dimensions [133], since this allows us to directly control the phonon MFP spectrum, and hence S_{ph}. In particular, as the sample dimension is reduced below a critical value, S_{ph} disappears meaning that in these samples $S \approx S_d$ [130]. S_{ph} in samples with a larger dimension can thus be estimated by subtracting out the Seebeck coefficient of these smaller samples. Because this method does not rely on the estimation of S_d from theory, it allows for a true extraction of S_{ph}.

In this chapter, we extend the concept of dimension scaling to extract S_{ph} in the AlGaN/GaN 2DEG. A large S_{ph} could help in the design of where low-temperature thermoelectric power sources, which would be ideal for the space environment [134]. We note here that the S_{ph} is due to the interaction of 3D phonons in the underlying GaN layer with the electrons at the AlGaN/GaN interface. Both GaN and AlN have relatively high Debye temperatures (600 K and 1150 K) [77], suggesting

that non-equilibrium phonons should be present in these materials below this temperature. This suggests that phonon drag could be observed, even at room temperature in this material system.

Using a combination of experiments and analytical modelling across 50 to 300 K, we experimentally separate out S_{ph} by comparing the thermoelectric properties of devices with various GaN thicknesses (100 nm to ∼1.2 µm). Further evidence for phonon drag is provided by examining the gate voltage dependency of the Seebeck coefficient. Our findings show that while S_{ph} is ∼32% of the total S at room temperature in a thick ∼1.2 µm device, S_{ph} is almost completely suppressed when t_{GaN} is reduced to ∼100 nm. By measuring the thermal conductivity in these samples, we show that the magnitude of the phonon drag can increase even when the thermal conductivity is decreasing. This decoupling of k and S_{ph} could enable significant advancements in thermoelectric power conversion. These first measurements of the thermoelectric properties of the AlGaN/GaN 2DEG in the low temperature range, are an important step toward understanding drag in such low-dimensional systems.

4.2 Fabrication and Procedure to Extract Phonon Drag

Experimental samples were fabricated via metal organic chemical vapor deposition (MOCVD) on an Si (111) wafer. In particular, the "thick" and the "thin" GaN samples previously discussed in *Chapter* 3 are re-used for this study. As a reminder, we note that the 2DEG forms in GaN at the AlGaN/GaN interface, has a nominal sheet density, $n_{2D} \approx 10^{13}$ cm^{-2} and a characteristic quantum well width of ∼5 nm [75].

The structures used to extract the thermoelectric properties of the 2DEG (S and k_{GaN}) are the same as previously described in *Section* 3.1.2. We recall that these are suspended AlGaN/GaN diaphragms, as depicted in Figures 4.1a and 4.1b. A 2DEG mesa was defined by etching the AlGaN on top of the membrane, except in a rectangular strip across which we extracted the Seebeck coefficient. Platinum (Pt) heater electrodes were deposited on top of a ∼47 nm atomic layer deposited (ALD) alumina layer to provide electrical isolation from the 2DEG and to create an in-plane temperature gradient across the 2DEG mesa. The main difference from the structure in *Section* 3.1.2 is that the mesa has a gate electrode (Au) on top of the alumina to modulate the charge density in the 2DEG, as seen in Figures 4.1a and 4.1c. This additional fabrication step is performed right before the silicon backside etch, as visualized in the fabrication flow in Figure 4.2.

Upon application of a temperature gradient via the Pt heater, a Seebeck voltage is measured across the mesa due to the thermal diffusion of the 2DEG electrons (V_d) and the drag imparted to

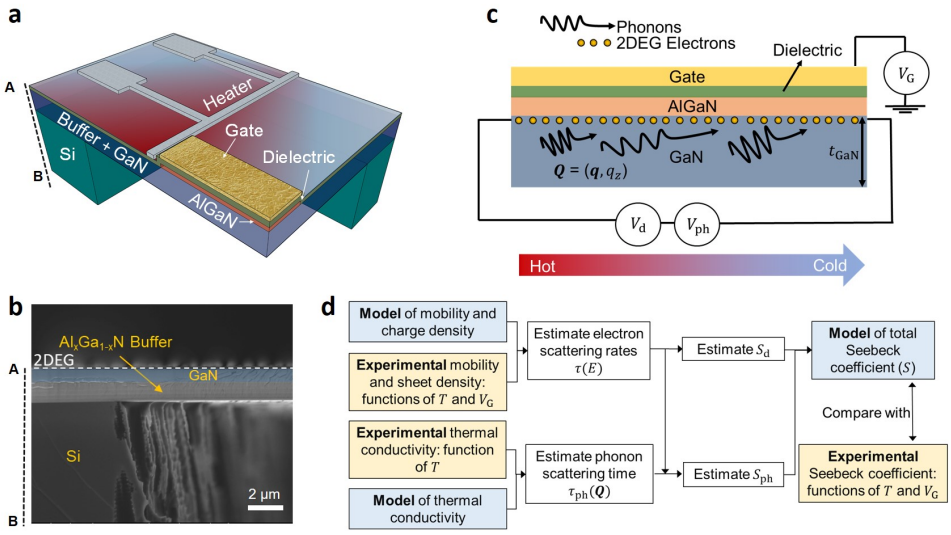

Figure 4.1: **Measurement platform to probe phonon drag**. (a) Schematic of suspended device to measure Seebeck coefficient, showing the heater metal, the AlGaN/GaN mesa, and the gate. (b) Cross-sectional SEM image of the suspended region, showing Si, the buffer and the GaN layer. This image is for the thick GaN sample, with $t_{GaN} \approx 1.2$ µm. (c) 2D schematic of the suspended mesa region, showing the drag and diffusive components of the Seebeck voltage. The phonon wave vector is marked by the symbol **Q**. (d) Flowchart showing the numerical procedure to extract the phonon drag component of the Seebeck coefficient, S_{ph}.

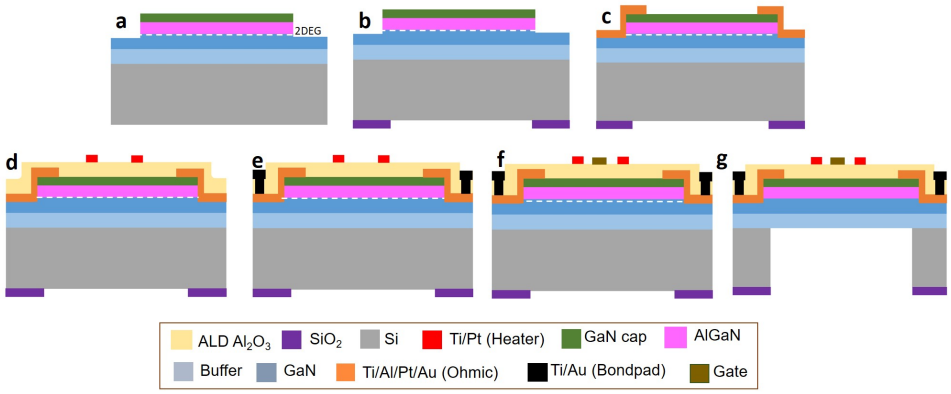

Figure 4.2: Fabrication process to create the suspended AlGaN/GaN diaphragms for measurement of thermoelectric properties.

them by phonons in the GaN layer (V_{ph}), as seen in Figure 4.2c. Using the heater as a thermometer, we extracted the Seebeck coefficient from the voltage across the 2DEG mesa, after accounting for the thermal losses in the alumina layer and the various interfaces. To extract the thermal conductivity

of the GaN and the underlying buffer layers, we used the same structure from *Section* 3.1.2. The flowchart in Figure 4.1d summarizes our numerical procedure to extract S_{ph}. Measurements of the 2DEG sheet density, n_{2D} and mobility, μ were taken and compared with an analytical model to obtain the scattering times, $\tau(E)$ for the 2DEG as a function of energy. The obtained $\tau(E)$ is used to calculate the diffusive component of the Seebeck coefficient, S_d. The thermal conductivity measurements are used to extract the MFP spectrum in the GaN layer, which is combined with $\tau(E)$ to calculate S_{ph}. This modeled S_{ph}, along with the calculated S_d, can be compared with the experimental values of the Seebeck coefficient for both the thick and thin GaN samples to shed light on the relative contribution of S_{ph}.

4.3 Measurement Notes

Although the calibration process for the various metal lines (heater and sensor) is identical to our previous description (*Section* 3.1.2), there are some key differences in the measurement process to extract the Seebeck coefficient and the thermal conductivity, which need to be discussed.The main distinction is that these experiments (from 50 to 300 K) were done in vaccum using a temperature controlled cryostat, while in *Section* 3.1.2, the experiments (300 – 573 K) were done in air as the ambient. Furthermore, since our Seebeck coefficient measurement now includes a gate, it is necessary to understand the modulation of the 2DEG sheet density and mobility as function of gate voltage. To obtain these gate and temperature dependent sheet densities and mobilities, we performed Hall effect and van der Pauw measurements in a vaccum cryostat. The use of vaccum ensures that any errors in the extraction of the thermal conductivity and Seebeck coefficient due to thermal convection effects are eliminated. In our measurement structures, the metal lines are placed on top of an amorphous alumina film of thickness ∼47 nm (to avoid electrical conduction with the underlying 2DEG), which needs to be properly accounted for to extract the thermal conductivity of the suspended film and the Seebeck coefficient of the 2DEG. For clarity, we re-visit some of the assumptions made to properly extract the thermal conductivity and the Seebeck coefficient.

We first focus on the thermal conductivity extraction procedure. As previously discussed in section *Section* 3.1.2, the thermal resistance of the suspended film (R_F) can be written as:

$$R_F = \frac{2(T_H - T_S)}{P_H} - 2R_{Al} - \frac{2(R_{mox} + R_{oxg})}{A_H} \tag{4.1}$$

where T_H and T_S are the heater and sensor line temperatures, P_H is the input power to the heater

and R_{Al} is the thermal resistance of the Al_2O_3 layer, A_H is the area projected area of the heater electrode (5 µm × 200 µm), R_{mox} is the thermal boundary resistance of the Heater/Al_2O_3 interface and R_{oxg} is the thermal boundary resistance of the Al_2O_3/GaN interface. The thermal conductivity of the film can be extracted from R_F and the known film dimensions. To calculate the thermal resistances, we denote t_{Al} and t_F are the thicknesses of the alumina and AlGaN/GaN/buffer film, respectively. We used a thermal boundary resistance of 2.8×10^{-8} m^2KW^{-1} for R_{mox} [84]. Although data for the thermal boundary resistance across the Al_2O_3/GaN film interface is not available, we estimated $R_{oxg} \approx 1\times10^{-8}$ m^2KW^{-1} based on measurements across amorphous dielectric/Si interfaces [85], since GaN and Si have similar Debye temperatures [86, 77]. The thermal resistance of the alumina layer can be estimated as $R_{Al} = \frac{t_{Al}}{k_{Al}A_H}$, where k_{Al} is the temperature dependent thermal conductivity of the alumina layer. The measurements for the thermal conductivity of

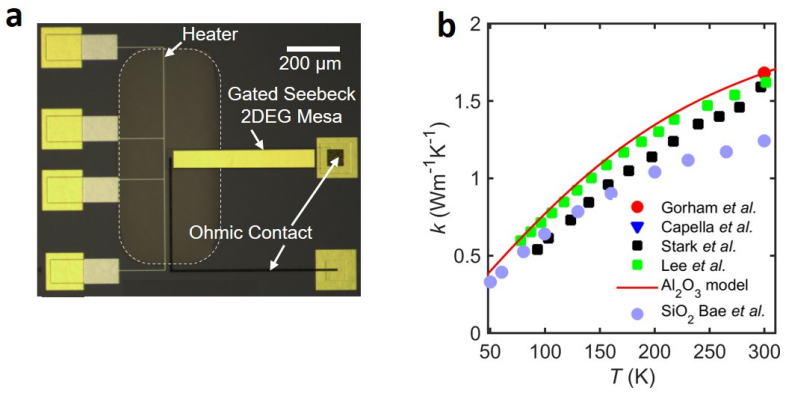

Figure 4.3: (a) Microscope image of the gated Seebeck coefficient measurement structure. (b) Temperature-dependent thermal conductivity for the amorphous alumina film.

amorphous alumina films have been published in the literature before. It is worth noting that amorphous films are typically modeled by the differential effective-medium (DEM) approximation, where $k \propto n^{(\frac{2}{3})}$, with n denoting the atomic density of the film [135]. Thus, the variation in the thermal conductivities between the different films is attributed to the different densities, which depends strongly on the growth technique and deposition temperature. Our film is prepared via atomic layer deposition (ALD) at a temperature of 200°C, whose thermal conductivity has been previously measured by Gorham et al. under the same condition at room temperature [135]. The temperature dependent thermal conductivities of alumina films prepared under different conditions have been reported by a few other research groups [84, 135, 136, 137], as seen in Figure 4.3b. Since

we can attribute the difference exclusively to density, we fit the thermal conductivity obtained by Lee et al. for different temperatures [137], and scale it to match the value obtained by Gorham et al. at room temperature [135] to obtain k_{Al}, marked by a red line in Figure 4.3b. In conclusion, since R_{mox}, R_{oxg} and R_{Al} are known from equation (4.1), we can calculate R_F which can be used to obtain the thermal conductivity (k_F) of the suspended film.

4.4 Measurements Under no Gate Bias

We first discuss the measurements of the thermoelectric properties under no gate bias. Figure 4.4a shows measurements of n_{2D} for the thick and thin GaN sample, extracted via Hall effect and van der Pauw measurements. The inset shows a schematic band diagram of the AlGaN/GaN quantum well, with the 2DEG depicted as the triangular region at the interface below the Fermi level (E_F). The thickness of the quantum well, t_{2D}, is defined as the distance from the AlGaN/GaN interface to the intersection of E_F and the GaN conduction band. We obtain a roughly constant $n_{2D} \approx 10^{13}$ cm^{-2} from 50 K to 300 K, consistent with the weak dependence on temperature of the piezoelectric constants of both AlN and GaN [52]. The thin and thick GaN samples have a similar charge density, verified using a commercially available Schrödinger-Poisson solver [55] as seen in Figure 4.4a. We also obtain $t_{2D} \approx 6.1$ nm and $t_{2D} \approx 4.4$ nm for the thick and thin GaN sample from the solver. For simplicity, we set $n_{2D} = 10^{13}$ cm^{-2} for both the thin and thick GaN samples in the models for the thermoelectric transport properties. Using the expression for the 2D density of states, assuming that all the sheet density is from a single subband, $g_{2D} = \frac{m^*}{\pi\hbar^2}$, we get $E_F - E_1 \approx 110$ meV, where E_F is the 2DEG Fermi level and E_1 denotes the energy at the bottom of the first subband. This is consistent with the energies obtained from the solver (Figure 4.5a), and indicates that only the bottom subband contributes significantly to charge density. For the rest of this work, only this subband is considered in the calculation of the Seebeck coefficient, because the contribution to S from each subband is weighted by the charge density in it [138]. Next, we turn to measurements of the 2DEG mobility, plotted in Figure 4.4b and Figure 4.4c for the thick and thin GaN samples, respectively. The dotted lines show the calculated contributions to the mobility from scattering mechanisms that are dominant in AlGaN/GaN 2DEGs [59]. Other scattering mechanisms (e.g. dislocation, ionized impurity and piezoelectric scattering) are neglected. Rigorous justification of this approximation is found in **Appendix A**. For both thick and thin GaN, polar optical phonon (POP) scattering is the dominant scattering mechanism at room temperature, due to the large optical phonon energy ($\hbar\omega_{OP} = 91.2$ meV) [139], and the polar nature [112] of the GaN wurtzite crystal. As

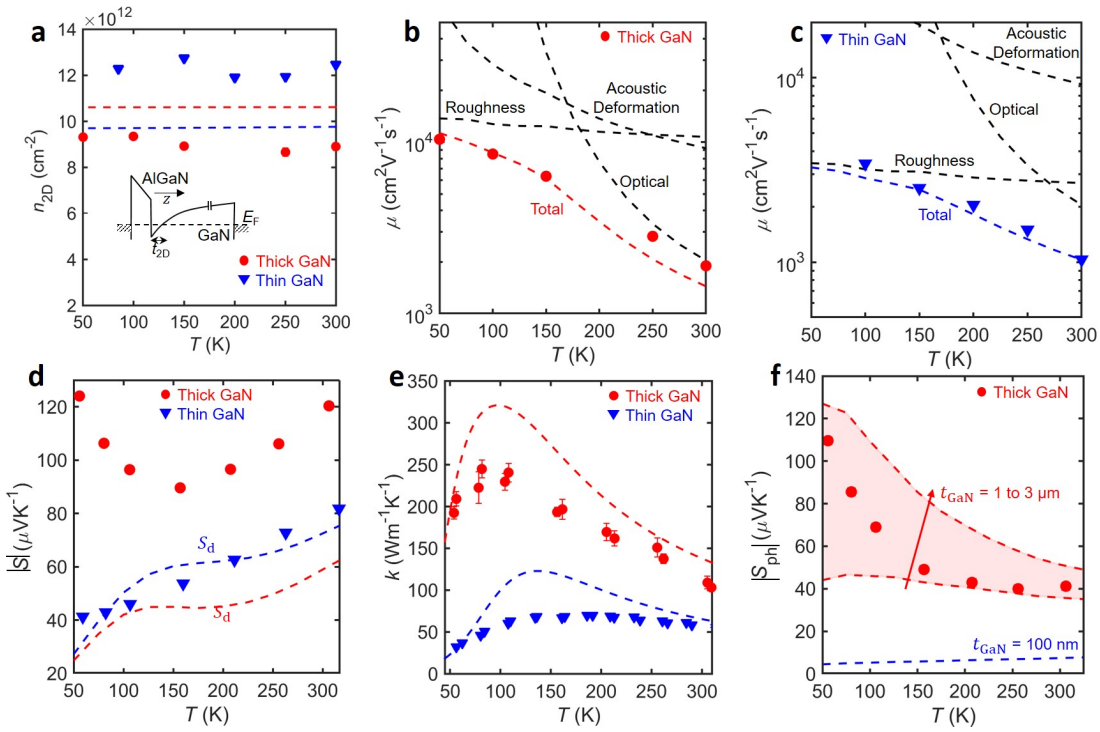

Figure 4.4: **Measurements for un-gated devices**. (a) Temperature dependent sheet density (n_{2D}) of the thick and thin GaN sample. The experimental markers (blue triangles and red circles) are obtained from Hall-effect and van der Pauw measurements, while the dashed lines show the simulated values obtained from a commercial solver. The inset shows a schematic of the AlGaN/GaN quantum well, with the Fermi level and the characteristic thickness of well, t_{2D}, marked. (b,c) Mobility for the thick and thin GaN sample, with the dashed lines showing the simulated components, and the markers from Hall and van der Pauw measurements. (d) Measured Seebeck coefficient. The dashed lines show the calculated diffusive components, which are similar for the thick and thin GaN samples. (e) Measured (markers) and calculated (dashed lines) thermal conductivities for the thick and thin GaN samples. (f) Simulated values of the phonon drag component of the Seebeck coefficient obtained by sweeping the effective thickness of the GaN layer. The red markers show the estimated drag component for the thick GaN sample extracted from the experimental data. A clear suppression of phonon drag is observed for smaller GaN layer thickness.

the optical phonon population decreases exponentially at lower temperatures, electrons in the lower subband scatter against the AlGaN/GaN interface (which we denote as roughness scattering). In order to calculate the roughness scattering, we set the average displacement of the interface, Δ, to be 1 and 2 nm for the thick and thin GaN sample respectively (an AFM image of the sample surface can be found in Figure 4.5b). The good agreement between the model and experimental data allows us to extract the scattering time, $\tau(E)$ for the electrons in the bottom subband of the 2DEG. Using these scattering times, we can calculate the diffusive component of the Seebeck coefficient for the

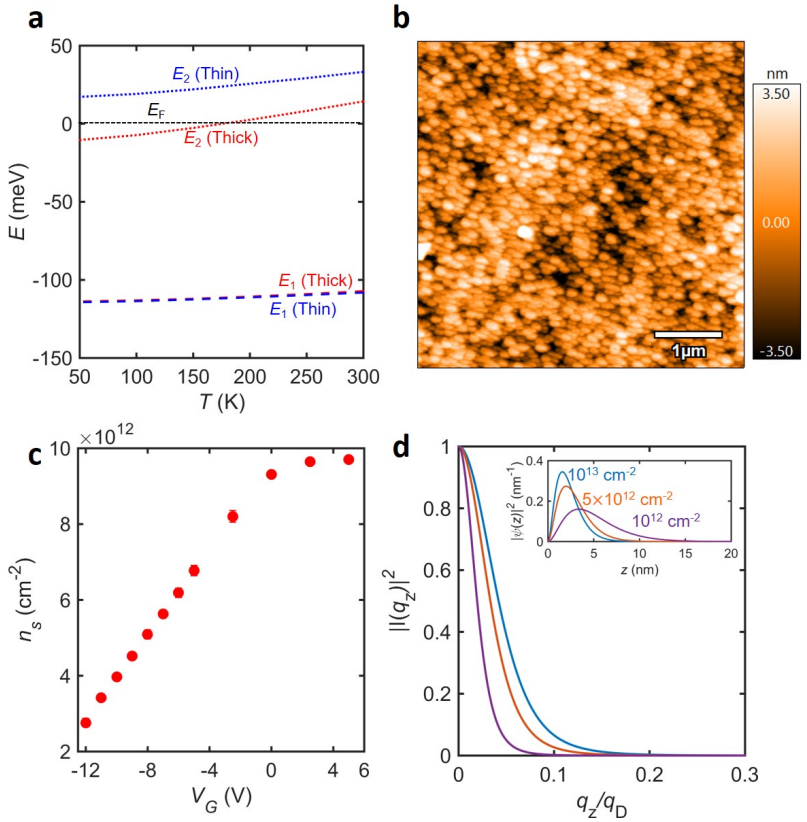

Figure 4.5: (a) Energies of the bottom 2 subbands in the AlGaN/GaN quantum well for the thick and thin GaN samples. (b) AFM image of the surface of the thick GaN sample (with the alumina layer on top). The RMS roughness is estimated to be ∼1.4 nm. (c) Gating of the sheet density in the thick GaN sample at a temperature of 50 K. (d) Electron-phonon momentum conservation in the out-of-plane direction for 2DEG sheet densities varying from 1-10×10^{12} cm^{-2}. The corresponding shape of the wave function, $\psi(z)$, for the bottom subband at the 2DEG at the AlGaN/GaN interface is shown in the inset.

bottom subband, S_d as [140]:

$$S_d = -\frac{1}{eT}\frac{\int E\frac{\partial f_0(E)}{\partial E}(E - E_F - E_1)\tau(E)dE}{\int E\frac{\partial f_0(E)}{\partial E}\tau(E)dE}, \tag{4.2}$$

where $f_0(E)$ is the Fermi function, and e is the magnitude of the electronic charge. These are plotted against the experimental data for the magnitude of the Seebeck coefficient (the actual sign is negative) in Figure 4.4d. The theoretical curves deviate slightly from a linear dependence on temperature, typical for a degenerate semiconductor with $\tau(E) \propto E^{\alpha}$, where α is a scattering exponent [138]. This deviation is due to POP scattering, which forbids electrons with energies

smaller than $\hbar\omega_{OP}$ from emitting optical phonons [140]. The slight difference in the calculated values of S_d for the thick and thin GaN sample is attributed to differences in roughness scattering. We observe that the Seebeck coefficient for the thin GaN sample agrees well with the calculated S_d, however this model cannot describe the thick GaN sample (Figure 4.4d). In addition, the magnitude of the Seebeck coefficient in the thick GaN sample exhibits a prominent upturn at low temperatures, hinting at phonon drag [132].

In our device, 3D phonons, represented by the wave vector $\mathbf{Q} = (\mathbf{q}, q_z)$, which represent the in-plane (of the 2DEG) and out-of-plane component, scatter with 2D electrons in the bottom subband, giving rise to S_{ph}. To calculate this drag, we follow the approach introduced by Cantrell and Butcher [122] and later modified by Smith [141, 142]. We additionally add a correction to include the phonon scattering time (τ_{ph}) as a function of the phonon wave vector explicitly:

$$S_{ph} = -\frac{(2m^*)^{\frac{3}{2}} v_{av}^2}{4(2\pi)^3 k_B T^2 n_{2D} e\rho} \int_0^\infty dq \int_{-\infty}^\infty dq_z \frac{\Xi^2(\mathbf{Q}) q^2 Q^2 \mid I(q_z) \mid^2 G(\mathbf{Q}) \tau_{ph}(\mathbf{Q})}{S^2(q,T) \sinh^2(\frac{\hbar\omega_Q}{2k_B T})}. \tag{4.3}$$

In equation (4.3), v_{av} is the average phonon velocity over the different modes, k_B is the Boltzmann constant, m^* is the electron effective mass and ρ is the density of GaN. The values of the parameters used for our calculations are in Table 4.1. The phonon frequency, ω_Q is approximated as $v_{av}\sqrt{q^2 + q_z^2}$ assuming a linear dispersion. The term $I(q_z) = \int \psi(z)^2 e^{\mathrm{i}q_z z}$ describes the electron-phonon momentum conservation in the z direction, where $\psi(z)$ is the wave function of the electrons in the bottom subband. The term $S(q,T)$ is a screening function for the electrons in the 2DEG. Detailed explanations for $I(q_z)$ and $S(q,T)$ are in **Appendix A**. $\Xi(\mathbf{Q})$ denotes the acoustic electron-phonon scattering potential (for the longitudinal and 2 transverse modes). The explicit expression for $\Xi(\mathbf{Q})$ is [142]

$$\mid \Xi \mid^2 = D^2 + \frac{8q_z^2 q^2 + q^4}{2(q^2 + q_z^2)^2}, \tag{4.4}$$

where the first term represents the scattering via the deformation potential (with strength of the interaction described by constant D) and the second term accounts for piezoelectric scattering. In equation (4.3), $G(\mathbf{Q})$ is the energy integral, which is written as:

$$G(\mathbf{Q}) = \frac{1 - e^{-\frac{\hbar\omega_\mathbf{Q}}{k_B T}}}{\hbar\omega_\mathbf{Q}} \int_\gamma^\infty dE \frac{f_0(E)(1 - f_0(E + \hbar\omega_\mathbf{Q}))}{\sqrt{E - \gamma}}. \tag{4.5}$$

In equation (4.6), $\gamma = \frac{\hbar\omega_\mathbf{Q} - E_q^2}{4E_q}$, with $E_q = \frac{\hbar^2 q^2}{2m^*}$. In Figure 4.5d, we show the form $I(q_z)$ for a range for n_{2D} varying from 10^{12} to 10^{13} cm^{-2}, where we note that for small values of q_z, $I(q_z) \approx 1$, but

Table 4.1: Definitions of Selected Parameters for Phonon Drag Calculations.

Parameters	Symbol(Units)	Value	Reference
Effective electron mass	m^*	$0.22m_e$	[59]
GaN dielectric constant	ϵ (F·m^{-1})	$10.4\epsilon_0$	[59]
GaN sheet density	n_{2D} (cm^{-2})	$\sim$1×10^{13} cm^{-2}	Our measurements
GaN deformation potential	D (eV)	8.5	[77]
Optical phonon energy	$\hbar\omega_{OP}$ (meV)	91.2	[77]
Density of GaN, AlN	ρ (kg·m^{-3})	6150, 3266	[77]
Grüneisen parameter	γ_G	0.5	[77]
Atomic mass of GaN, AlN	M (amu)	83.7, 40.99	[77]
Average phonon velocity in GaN, AlN	v_{av} (m·s^{-1})	5070.5, 7183.5	[77]
GaN, AlN Debye temperature	θ_D (K)	600, 1150	[77]
GaN Umklapp scattering constants	P (eV), C_U (K)	1.1375 eV, 132 K	[143]
AlN Umklapp scattering constants	P (eV), C_U (K)	2.0625 eV, 382 K	[144]

around q_z corresponding to the Debye wavelength (about 1.55×10^{10} m^{-1} in GaN), $I(q_z) \approx 0$. The physical interpretation is that for thinner quantum wells (smaller Δz), larger values of q_z are allowed to interact with the 2D electrons because the momentum conservation in the out-of-plane direction is less stringent [132]. Finally, we also note that because of the specific shape of $I(q_z)$, we can set the limits of the integration in equation (4.3) to the Debye wave vector (instead of ∞).

Of particular interest to us is $\tau_{ph}(\mathbf{Q})$ which appears in equation (4.3), the term representing the relaxation time of the phonons. This term describes the scaling dependence of S_{ph} on sample thickness, because $\tau_{ph}(\mathbf{Q}) \propto t_{GaN}$ due to boundary scattering. In particular, it is necessary to calculate the phonon scattering time, $\tau_{ph}(\mathbf{Q})$ in the GaN layer. This can be estimated accurately from the in-plane thermal conductivity measurements of the suspended AlGaN/GaN film. Since we do not have thermal conductivity measurements of the GaN layer exclusively, we follow a more involved approach. In particular, we first model the thermal conductivity of the composite film and compare with experimental data. Then, we use the model for the GaN film to estimate the $\tau_{ph}(\mathbf{Q})$ needed to calculate S_{ph}.

The approach for calculating k is similar to the procedure described in *Section* 3.1.8. The overall thermal conductivity (k) can be estimated as $\frac{\sum k_i t_i}{\sum t_i}$, where k_i and t_i refer to the thermal conductivities and thicknesses of individual layers. For each multilayer, we used a Boltzmann Transport Equation (BTE) model to quantify k_i with layer thickness (t_i). Using a simple Debye approximation for the phonon dispersion with an average velocity over the acoustic phonon modes (v_{ac}), the

in-plane thermal conductivity for each layer can be written as [145]:

$$k_i = \frac{k_B^4 T^3}{2\pi^2 \hbar^3 v_{av}} \int_0^{\frac{\theta_D}{T}} \frac{x^4 e^x \tau(x)}{(e^x - 1)^2}, \tag{4.6}$$

where θ_D is the Debye temperature for the multilayer, and $x = \frac{\hbar\omega_Q}{k_B T}$. The total scattering time is calculated by Mathiessen's rule with contributions from Umklapp (τ_U), alloy (τ_A), boundary (τ_B) and defect scattering (τ_D), respectively. Phonon-phonon scattering is evaluated using via the relaxation term for Umklapp processes [99]

$$\tau_U(x) = \frac{P k_B T^3 x^2 e^{-\frac{C_U}{T}}}{\hbar^2}, \tag{4.7}$$

where the constants P and C_U for GaN and AlN are listed in Table 4.1. To evaluate the boundary scattering term, we used $\tau_B \approx 2.38\frac{t_i}{v_{av}}$ [95]. The remaining scattering terms are modeled as described in *Section* 3.1.8. The dotted lines in Figure 4.4e show the modeled k for the entire stack, taking into account all the described scattering mechanisms. The alloy and dislocation scattering terms are challenging to estimate analytically [97, 98], which could explain the disagreement between the model and the data at the lower temperatures. Yet, this model will suffice to explain the observed trends in the phonon drag behavior. Assuming that only the phonons in the GaN layer contribute to drag, the modelled τ_{ph} for this layer is combined with equation (4.3) to calculate S_{ph}.

The modeled S_{ph} is plotted in Figure 4.4f for a range of t_{GaN} values. It is seen that S_{ph} for the thin GaN is between 4 and 8 μV·K^{-1} across all T, significantly less than the measured 40 to 80 μV·K^{-1} (Figure 4.4d), supporting the conclusion that $S \approx S_d$. The nearly constant S_{ph} can be attributed to k_{GaN} being limited by boundary scattering across the entire temperature range. S_{ph} in the thick GaN film was estimated by subtracting a linear fit (including the origin) of the measured Seebeck coefficient in the thin GaN sample from the measured Seebeck coefficient of the thick GaN sample. We have used a linear fit to the origin of the thin GaN Seebeck coefficient to avoid overestimating the diffusive component of the Seebeck coefficient. This is because the measured Seebeck coefficient values of the thin GaN sample still includes a small phonon drag component, which is visible as a slight upturn at the lower temperatures (blue triangles in Figure 4.4d). The estimate of S_{ph} for the thick GaN sample after subtraction from the linear fit is plotted in Figure 4.4f (red markers). The shaded region shows the calculated S_{ph} for various effective GaN thicknesses (t_{GaN}) from 1 to 3 µm using equation (4.3). We have swept the GaN thickness in the model since it under-predicts S_{ph} if we use the actual thickness (1.2 µm). This inaccuracy may arise from the simple model for the thermal

conductivity and phonon drag used here, in addition the 2DEG quantum well thickness, which is challenging to obtain experimentally. The data and model agree within the swept thickness range, and shows that ∼32% of the total S at room temperature can be attributed to drag, increasing to almost 88% of S at 50 K. The inverse temperature dependence of S_{ph} is reflective of phonon-phonon scattering, from which the phonon MFP scales as T^{-1}.

The measurements of the Seebeck coefficient and the thermal conductivity in Figures 2e and 2f also suggest that the phonon drag continues to increase even when the thermal conductivity starts decreasing (below ∼90 K), providing experimental demonstration that these two parameters can be decoupled. This is in agreement with previous theoretical work suggesting that these two parameters can be decoupled to increase zT [146, 61].

4.5 Measurements Under Gate Bias

The application of a gate voltage, V_G, can tune the thermoelectric power factor ($S^2\sigma$) without changing k, which can further optimize zT [147, 101]. While the effect of V_G on S_d is well known, only a few studies have attempted to quantify its effect on drag [132, 148, 149]. In particular, application of V_G tunes the quantum well width and 2DEG charge density (n_{2D}), simultaneously. S_{ph} is inversely proportional to n_{2D} giving it a strong dependency on this parameter, as seen in equation (4.3). Quantum well width affects S_{ph} through $I(q_z)$ which is strongly dependent on wave function shape $\psi(z)$. A more tightly confined wave function in real space (which corresponds to larger n_{2D}) is broader in Fourier space, increasing $I(q_z)$. These two effects compete against each other resulting in a complex gate voltage dependency.

Hall-effect measurements of the 2DEG sheet density as a function of gate voltage are presented in Figure 4.6a. The data at 300 K shows a depletion of the 2DEG sheet density by up to a factor of ∼3x from its ungated value as V_G is lowered to -12 V. The gating is similar at lower temperatures (data for the thick GaN sample at 50 K are plotted with black circles in Figure 4.6a) and for the thin GaN sample. The inset of Figure 4.6a shows how depletion widens the quantum well at the AlGaN/GaN interface. Depletion also reduces the 2DEG mobility as seen in Figure 4.6b, similar to former work [150, 81]. To study the effect of gating on S_{ph}, we need to first estimate S_d as a function of gate voltage. This can be done by studying the effect of V_G on the thin GaN sample, presented in Figure 3c. For a degenerate 2D quantum well, we can roughly approximate the magnitude of the diffusive Seebeck coefficient as $S_d \propto \frac{T}{(E_F - E_1)}$ [138]. Since $n_{2D} \propto (E_F - E_1)$, the magnitude of the diffusive Seebeck coefficient should increase with negative V_G as it depletes the 2DEG and decrease

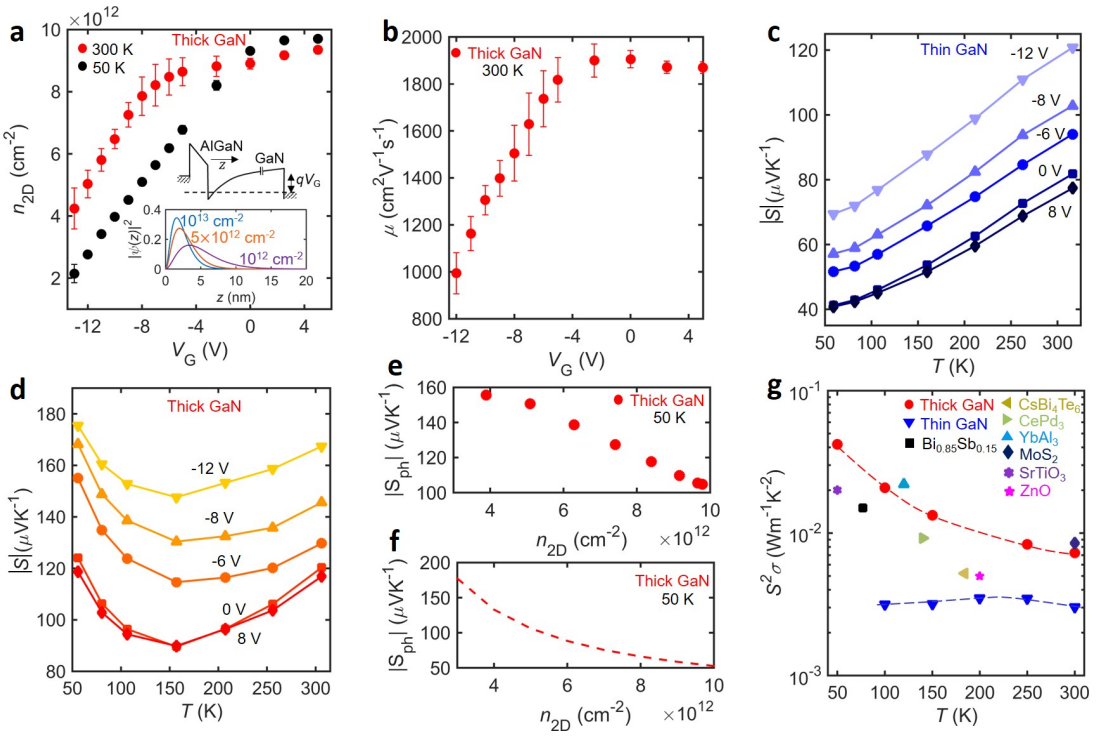

Figure 4.6: **Measurements with a gate bias**. (a) Modulation of the sheet density in the 2DEG (n_{2D}) with applied gate bias at 300 K and 50 K for the thick GaN sample. The markers are obtained from Hall-effect measurements. The inset shows the simulated wave function in the bottom subband of the 2DEG for three different sheet densities. The coordinate $z = 0$ corresponds to the AlGaN/GaN interface, as seen in the band diagram (black lines). Positive z represents the GaN layer. (b) Experimental measurements of field-effect mobility at 300 K. (c,d) Gated Seebeck coefficient measurements for the thin and thick GaN sample. The solid lines are a guide for the eye, while the makers are the experimental measurements. (e) Estimated drag component for the thick GaN sample from the experimental data, at 50 K. (f) Simulated phonon drag component for the thick GaN sample (using $t_{GaN} = 1.2$ µm) for 2DEG sheet densities that correspond to our applied voltage range, at 50 K. (g) Estimated temperature-dependent power factors for the thin and the thick GaN samples from 50 to 300 K from the experimental data, with the gate grounded. The dashed red and blue lines are guidelines for the eye. We have also included power factor data from other material systems for comparison with the thick GaN 2DEG.

linearly with T. Both features are visible in Figure 4.6c.

Figure 4.6d shows the effect of V_G on the magnitude of the Seebeck coefficient in the thick GaN sample, where the upturn below ∼150 K is apparent even after depletion. As in Figure 4.4f, we subtracted a linear fit of the thin GaN Seebeck coefficients (in Figure 4.6c) from the values for the thick GaN to estimate S_{ph} for different V_G. Because we know the relation between n_{2D} and V_G (Figure 4.6a), we can thus estimate S_{ph} as a function of n_{2D}. We have plotted the gate-voltage

dependence of S_{ph} at a fixed temperature of 50 K, for different n_{2D} values in Figure 4.6e. It is seen that the magnitude of S_{ph} increases by a factor of ∼1.5x as n_{2D} decreases from 10^{13} cm^{-2} to 3×10^{12} cm^{-2}. To confirm the trend of these values, we also simulated S_{ph} over this n_{2D} range (4.3) (with the actual GaN thickness of 1.2 µm), taking into account the shape of the quantum well. These simulations are plotted in Figure 4.6f at a temperature of 50 K, for ease of comparison to the data in Figure 4.6e. The simulated data shows the same trend (i.e., magnitude of S_{ph} increasing as n_{2D} decreases), but the increase is much larger (∼3x). Although the reason for the mismatch needs further study, these trends of S_{ph} vs. V_G suggest that the Seebeck coefficient behavior in the thick GaN sample is indeed due to PD. Further, they show that depleting the AlGaN/GaN 2DEG increases the magnitudes of both the diffusive and drag components of the Seebeck coefficient.

Finally, it is worthwhile to examine the TE power factor ($S^2\sigma$) of the 2DEG in both the thick and the thin GaN sample. These values are plotted in Figure 4.6g, where the gate is grounded. In order to calculate the conductivity of the 2DEG, σ, we use the mobility values in Figure 4.4b and Figure 4.4c, along with an estimate for the average volumetric charge density, $n_v = \frac{n_{2D}}{t_{2D}}$. The n_{2D} values are taken from the experimental values in Figure 4.4a. While the power factor for the thin GaN sample is quite insensitive to temperature, the value for the thick GaN sample shows a pronounced enhancement at low temperatures, as seen in Figure 3g, reaching ∼40 mW·m^{-1}K^{-2} at 50 K. This high power factor, which originates from the upturn of the Seebeck coefficient at low temperatures via phonon drag, is state-of-the-art when compared with other TE materials also plotted in Figure 4.6g ($Bi_{0.85}Sb_{0.15}$ [151], $CsBi_4Te_6$ [152], $CePd_3$ [153], $YbAl_3$ [154], MoS_2 [155]). We have also plotted the power factors for other 2DEG systems where measurements are available, such as gated ZnO [101] and gated $SrTiO_3$ [148] for comparison in Figure 4.6g. The enhancement of the Seebeck coefficient in our thick GaN sample is in contrast with typical TE materials, where the power factor scales directly with temperature because the Seebeck coefficient is diffusive [152]. The high power factor values in the thick GaN sample, although only for a single 2DEG, are promising for planar applications such as Peltier coolers. Further, they could make promising low-temperature energy harvesting elements when structured as a superlattice [65].

4.6 Conclusion

In conclusion, we have experimentally shown that phonon drag can be a significant portion of the total Seebeck coefficient in a 2DEG, even at room temperature. By using thickness as a "knob" to control sample dimensions, we show that S_{ph} is suppressed in the AlGaN/GaN 2DEG at a film

dimension of ∼100 nm. From a thermoelectric power conversion perspective, we shed light on two important phenomena: First, the magnitude of the phonon drag can increase even when the thermal conductivity is decreasing, which means that these could be tuned separately. Second, depleting a 2DEG can lead to an increase in both the phonon drag and diffusive contributions of the Seebeck coefficient. These findings enable a better understanding of the phonon drag effect, and can lead to advancements in thermoelectric power conversion across a wide range of temperatures.

Chapter 5

Unconventional Sensing Applications in AlGaN/GaN 2DEGs

In Chapter 2, we introduced the concept of using the AlGaN/GaN 2DEG as an extreme environment IoT platform. Specifically, this requires the maturation of sensing, logic and power delivery technologies under these harsh environment conditions. In this chapter, we discuss novel sensors that can be made using the innate polarization fields in the AlGaN/GaN 2DEG. In the first part of this chapter, the combined effect of applied strain and temperature on the device characteristics of AlGaN/GaN high electron mobility transistors (HEMTs) is discussed. The developed model is a useful tool for predicting the response of HEMTs used in sensing and under the influence of packaging in extreme environments, especially when temperature fluctuation and strain coupling is of concern. The second part of this chapter discusses a novel photodetector that uses the AlGaN/GaN 2DEG for its electrodes, which leads to record signal-to-noise performance.

5.1 Strain Sensing Using the AlGaN/GaN 2DEG

5.1.1 Introduction

We recall that AlGaN/GaN HEMTs leverage a two-dimensional electron gas (2DEG), which is created by the spontaneous and piezoelectric polarization in these heterostructured materials [112]. The amount of charge in the 2DEG is altered by external strains and temperature swings, which ultimately leads to a shift in the current-voltage characteristic of the HEMT device. This strain-temperature sensitivity can impact electronic device stability under packaging and thermal stresses. In addition, strain sensitive transistor elements can be exploited to create sensors used for the measurement of pressure, force, acceleration and torque. However, temperature compensation techniques are required if they are to be operated under temperature excursions in a reliable fashion.

Recently, AlGaN/GaN heterostructures have been used to create a variety of sensors (physical, chemical and biological) [156] and micromechanical resonators [157, 158, 159] demonstrating the flexibility of this electronic material system. Strain sensors using the AlGaN/GaN 2DEG as a piezoresistor have shown measured gauge factors (at room temperature) with a wide range of values, from -2.8 to $-40,000$, while simulated gauge factors are only in the range of -7.9 ± 5.2 [160]. The simulated gauge factors for AlGaN/GaN 2DEGs are low in comparison to piezoresistors made of Si [161]. The discrepencies between simulation and experiment calls for a better understanding of the fundamental physics that govern the strain response of these devices. In addition, AlGaN/GaN piezoresistors suffer from temperature cross-sensitivity which is significant at high-temperatures and interferes with the strain measurement. However, there are no experimental reports of the strain response of AlGaN/GaN HEMT devices at temperatures above 100°C [162] and few reports of simulation models which capture this operating condition [163]. Recent experimental results have demonstrated a large increase in the strain sensitivity of AlGaN/GaN HEMTs (transistor based) [164, 165, 115]. In these reports, it has been shown by experiment that the current-voltage response of the HEMT and the strain configuration (biaxial versus uniaxial) play a key role in achieving large sensitivity. Specifically, the biaxial configuration is recommended to enhance strain sensitivity. Further, recent results also show that the effect of strain on the 2DEG charge varies strongly due to the interface state density at the Schottky contact [115], however, this has not been explored in detail. Thus, in order to achieve the full potential of AlGaN/GaN HEMTs for strain sensing in extreme environments, there is a need for a comprehensive theoretical model which predicts the strain sensitivity over a wide range of temperatures and to develop methods to decouple the strain

response from temperature, and vice-versa.

In this section, a comprehensive, physics-based model is developed to determine the strain-temperature behaviour of commonly microfabricated AlGaN/GaN HEMT devices. Many of the physical parameters that dictate the electrical characteristics of AlGaN/GaN HEMTs are strain- and temperature-dependent. As a result, our physical model includes the effect of temperature and strain on parameters such as the elastic coefficients, piezoelectric coefficients, band-structure, atomic lattice constants, and carrier concentration, which is critical to realizing practical approximations. Our model was applied to predict the current-voltage response of an AlGaN/GaN HEMT under a range of temperatures and strain loading conditions for a variety of interface state densities at the Schottky contact. The temperature range is restricted to 300-500 K due to significant strain relaxation and degradation in HEMT devices above this limit [166]. The applied biaxial strain is limited to $\pm 1\%$ based on observations of the tensile strength in AlGaN and GaN to be $\sim$10 GPa at temperatures below 400°C [20]. Sensitivity analysis of this model identified device operation regimes for enhancing strain sensitivity and mitigating temperature effects. In addition, the validity of the model is tested through comparisons to recent data on microfabricated AlGaN/GaN HEMTs under controlled temperature and strain variations. Analysis of our model confirmed that AlGaN/GaN HEMTs can be effectively used for strain sensing in high-temperature environments under certain operating conditions.

5.1.2 Modeling the strain at the 2DEG interface

In this subsection, the total strain, composed of lattice mismatch, thermal and applied strains, at the 2DEG interface is modeled using temperature-dependent physical parameters. Figure 5.1 is an image of a commonly used AlGaN/GaN heterostructure under biaxial loading, which may be present due to device packaging or during sensor operation. As shown in Figure 5.1a, a typical Ga-face AlGaN/GaN HEMT is composed of an epitaxially-grown GaN thin film, thin AlGaN layer (20 to 30 nm thick) and a thin GaN capping layer (few nm) [167]. For modeling purposes, the substrate (e.g., Si, SiC) and buffer layers are not introduced and the thin GaN cap layer is ignored. The shorthand 1, 2, and 3 corresponds to $\langle 11\bar{2}0\rangle$, $\langle 10\bar{1}0\rangle$, and $\langle 0001\rangle$ directions in the Wurtzite AlGaN and GaN crystals, respectively. Strains generated during operation typically dominate in the basal plane (1- and 2-directions). Shown graphically in Figure 5.1b, the applied biaxial strain is in the 1- and 2-directions. Both GaN and AlGaN are naturally poled, and thus exhibit a spontaneous polarization when a heterostructure is created [51]. In addition, the application of an external strain

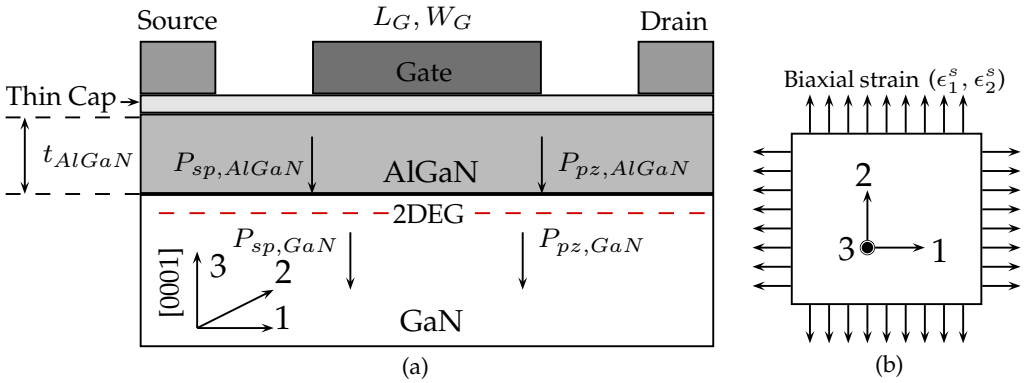

Figure 5.1: (a) Cross-sectional image of a typical Ga-face AlGaN/GaN heterostructure used in HEMT device microfabrication. (b) Top-view of the AlGaN/GaN HEMT under biaxial applied strain in the 1- and 2-directions (basal plane). ©2016 IOP.

leads to additional piezoelectric polarization charge [51]. The dipole vectors due to these two effects, represented by P_{sp} and P_{pz}, are depicted in Figure 5.1 with the dipole pointing from negative to positive charge.

Lattice mismatch strain

Due to the growth of two distinct AlGaN and GaN layers, a lattice mismatch strain (ϵ_l) is developed in the heterostructure. The stress-strain (σ-ϵ) constitutive relationship is:

$$\sigma_i = \sum_j C_{ij}\epsilon_i \qquad i,j = 1,...,6 \tag{5.1}$$

where C_{ij} is the form of the elastic coefficient matrix specific to the Wurtzite crystal [52], ϵ_i is the strain, and 4, 5, and 6 are shorthand for the shear stress components in the 23, 13, and 12 directions, respectively. The variation in the elastic coefficients is less than 5% for temperatures (T) between 300 K and 500 K [168], thus they can be treated as constants within this temperature range. It can be assumed that AlGaN grows as an epitaxial layer such that GaN is fully relaxed at the 2DEG interface, while AlGaN develops a biaxial lattice mismatch stress state (denoted with superscript l), such that $\sigma_1^l = \sigma_2^l$, while $\sigma_3^l = 0$. Since $\sigma_3^l = 0$, using (5.1), it is possible to relate ϵ_3^l to ϵ_1^l. Thus, as shown in (5.2), the strains developed in the AlGaN layer due to lattice mismatch are

$$\epsilon_1^{l,\alpha} = \epsilon_2^{l,\alpha} = \frac{a_\gamma - a_\alpha}{a_\alpha}, \quad \epsilon_3^{l,\alpha} = -2\frac{C_{13}^\alpha}{C_{33}^\alpha}\epsilon_1^{l,\alpha} \tag{5.2}$$

where a_γ and a_α are the basal plane (1- and 2-directions) lattice constants for GaN and AlGaN, respectively. Here, $2\frac{C^\alpha_{13}}{C^\alpha_{33}}$ is the Poisson's ratio. It should be noted that the superscript symbols α and γ are used to denote AlGaN and GaN, respectively. The effect of temperature on the epitaxial lattice mismatch strain is accounted for in the residual thermal strain, as discussed below.

Residual thermal strain

Growth of AlGaN and GaN thin films at elevated temperatures (approximately 1000°C) by metal organic chemical vapor deposition (MOCVD) causes residual strain due to differences in the thermal expansion coefficients [169]. The strains in the GaN and AlGaN layers due to thermal expansion ($\epsilon^{t,\gamma}$ and $\epsilon^{t,\alpha}$) are assumed to be independent from lattice mismatch strain and applied strain. However, they are temperature-dependent. In-plane thermal expansion causes the wafer to curve such that both materials have the same length at the interface as it is cooled from the growth temperature T_g to the operation temperature T. Assuming a growth temperature, T_g, and following the approach developed by Steude et al., [169], the temperature-dependent strains at the 2DEG due to biaxial, in-plane thermal expansion are given by

$$\epsilon^t_{1,a}(T) = \epsilon^t_{2,a}(T) = \pm\left|\frac{(a_\alpha^{T_g} - a_\alpha^T) - (a_\gamma^{T_g} - a_\gamma^T)}{1 + (a_\alpha^{T_g} - a_\alpha^T)}\right|, \quad \epsilon^t_{3,a}(T) = -2\frac{C_{13}}{C_{33}}\epsilon^t_{1,a} \tag{5.3}$$

where the lattice constants at different temperatures (a^T, a^{T_g}) can be approximated using the experimental data in [170]. Since the lattice constant of AlGaN is smaller than that of GaN at all temperatures, the in-plane strain is tensile for GaN (positive) and compressive for AlGaN (negative). Assuming the reference temperature T_{ref} at 0 K, out-of-plane (3-direction) residual thermal strain is approximated as

$$\epsilon^t_{1,c} = \epsilon^t_{2,c} = 0, \quad \epsilon^t_{3,c}(T) = \frac{c^T - c^{T_{\text{ref}}}}{c^{T_{\text{ref}}}} \tag{5.4}$$

where c^T and $c^{T_{\text{ref}}}$ are the temperature-dependent lattice constants of AlGaN (or GaN) in the 3-direction. The total residual thermal strain is the sum of the in-plane and out-of-plane components in each material for each direction, represented by $\epsilon_i^{t,\alpha}(T)$, $\epsilon_i^{t,\gamma}(T)$ $(i = 1 - 3)$ for AlGaN and GaN, respectively.

Applied strain

The state of the HEMT under an applied biaxial strain is shown in Figure 5.1b. Using the superscript s to denote applied strain, the biaxial applied strain state for AlGaN or GaN is defined as

$$\epsilon_1^s = \epsilon_2^s = R, \quad \epsilon_3^s = -2\frac{C_{13}}{C_{33}}\epsilon_1^s. \tag{5.5}$$

While $R = \pm 1\%$ as stated earlier, fracture in suspended GaN-on-Si devices occurs for applied strains as small as 0.2% due to stress concentrations limiting the failure strength [171], thus the output from our model should be used with caution in such scenarios.

Total strain

Depending on whether the applied strain is uniaxial or biaxial, the total strain can be calculated by summing the components of the lattice mismatch, thermal and applied strain for each material in each direction. This represents the strain state at the 2DEG, given by the directional components ϵ_i^α, ϵ_i^γ $(i = 1 - 3)$ for AlGaN and GaN, respectively.

5.1.3 Strain-and temperature-dependence of the 2DEG sheet conductivity

The mechanism of the formation of the 2DEG has been discussed previously in several references [172, 54, 173]. We present an explanation of the AlGaN-GaN interface and derive the expression for the 2DEG charge in the context of strain and temperature effects. Figure 5.2 shows the energy band diagram of an undoped AlGaN-GaN heterostructure. Both AlGaN and GaN have polarized charges at their surfaces due to the dipole vectors shown in Figure 5.1a. These charge densities are collectively represented by the symbol q_p. Since these charges are equal and opposite and present only on the surfaces, both the AlGaN and GaN layers behave like parallel plate capacitors with a constant internal electric field whose magnitude is given by $\frac{q_p}{\kappa}$, where κ is the absolute permittivity. From Figure 5.2, the electric field due to q_p is from the interface to the AlGaN surface for AlGaN, while it is from the interface to the surface in GaN. These polarization charges are immobile dipoles which implies that they are not the source of mobile 2DEG electrons. First, consider independent, isolated AlGaN and GaN layers, not in contact with each other. The presence of polarized charges alludes to a bent band with a constant electric field in equilibrium in these layers, as implied in the previous discussion. However, these bent bands lead to production of interface state generated

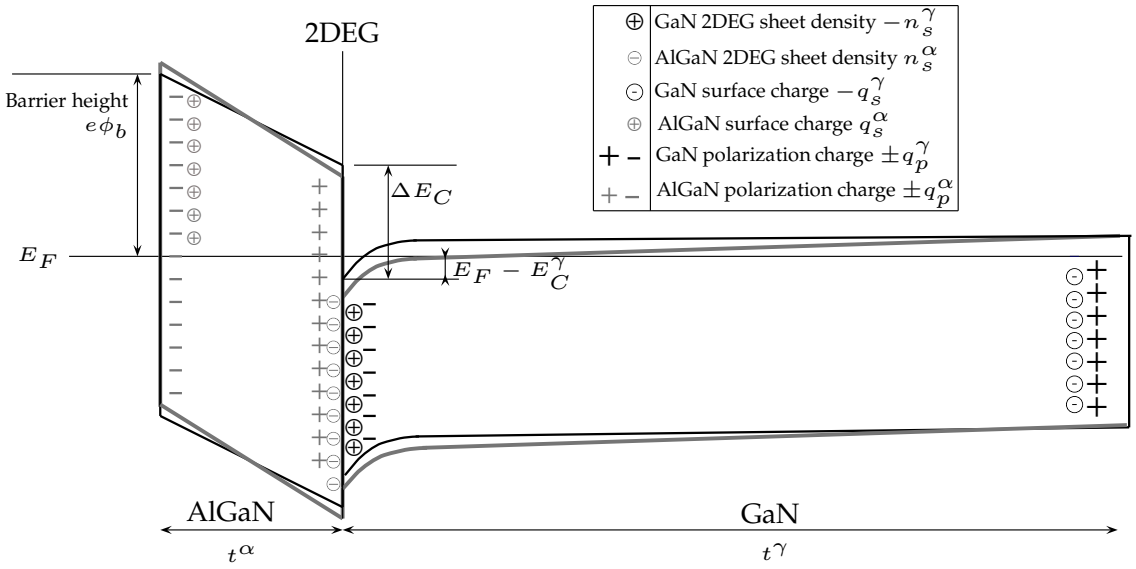

Figure 5.2: Schematic illustration of energy bands in an undoped AlGaN-GaN heterostructure. The black lines and the thick grey lines represent the bands with no strain and after the application of a tensile external strain, respectively. q_s, q_p represent surface and polarization charge densities, respectively. In the Figure, n_s represents the electron sheet density at the 2DEG. Further, it should be noted that the AlGaN and GaN surface charges arise from the net difference of the donor and acceptor states (whose density is constant in this model) on their surfaces. For large strain values, the change in the positions of the the conduction and valence band edge is significant (not shown in the Figure).©2016 IOP.

surface charges which tend cancel out the electric field created by the polarized charges, as depicted in Figure 5.2, leading to an overall minimization of the potential energy within the AlGaN and GaN layers. For simplicity in the analysis, it is assumed that the interface state density D_{it} of both acceptor and donor-type states is constant across the band-gap. The 2DEG is the result of these donor and acceptor states on the exposed AlGaN and GaN surfaces. A donor state behaves in equivalent fashion to a n-type donor, i.e., it is neutral if it is occupied by an electron and positively charged if it is not occupied by an electron. An acceptor state is negatively charged if it is occupied, while it is neutral if unoccupied. The Fermi and conduction levels are defined by E_F and E_C, respectively. The donor states below E_F are occupied and thus neutral. However, the donor states above E_F are not occupied and hence positively charged, leading to a net positive charge q_s^α on the exposed AlGaN surface. The electrons generated by the effective number donors n_s^α are swept by the electric field towards the 2DEG. Note that the units of q_p and n_s are that of charge density

and the number of charges per unit area, respectively. The GaN layer is unconstrained by a barrier height, thus, the occupied acceptor states below E_F on its exposed surface lead to a net negative charge $-q_s^\gamma$ that approximately cancels out the polarized charge. Since the structure is neutral on the whole, this leads to a reduction in the amount of 2DEG electrons due to GaN, represented by the symbol $-n_s^\gamma$. This implies that the net 2DEG sheet density n_s is equal to $n_s^\alpha - n_s^\gamma$. Further, it is worth noticing that when the thickness of the AlGaN layer is very small, very few donor states are unoccupied because E_F is close to the top of the conduction band of AlGaN, which implies that the 2DEG sheet density is lower for smaller AlGaN thicknesses. The potential drop across the AlGaN layer ΔV^α is simply calculated as the drop across a capacitor:

$$\frac{\Delta V^\alpha}{t^\alpha} = \frac{q_p^\alpha}{\kappa^\alpha} - \frac{e n_s^\alpha}{\kappa^\alpha} \tag{5.6}$$

where e and t^α refer to the magnitude of the electronic charge and the thickness of the AlGaN layer, respectively. Also, notice from Figure 5.2 that the potential drop can be equivalently written in terms of energy as

$$e\Delta V^\alpha = e\phi_b - [\Delta E_C - (E_F - E_C^\gamma)] \tag{5.7}$$

where ϕ_b is the barrier height at the AlGaN surface due to the gate contact. Both ΔE_C and $E_F - E_C^\gamma$ are calculated at the 2DEG interface, as represented in Figure 5.2. From (5.6) and (5.7), the electron sheet density in the 2DEG from AlGaN is

$$n_s^\alpha = \frac{q_p^\alpha}{e} - \frac{\kappa^\alpha}{e^2 t^\alpha}\left[e\phi_b - \Delta E_C + E_F - E_C^\gamma\right]. \tag{5.8}$$

Based on the assumption that the acceptor states on the GaN surface approximately cancel out the polarized charge, it is possible to approximate $-n_s^\gamma$ as $\frac{-q_p^\gamma}{e}$. In summary, for undoped pseudomorphic HEMTs, the total 2DEG charge density n_s taking into account temperature and strain effects is [172]

$$n_s(\epsilon, T) = \underbrace{\frac{q_p^\alpha(\epsilon) - q_p^\gamma(\epsilon)}{e}}_{1} - \frac{\kappa^\alpha}{e^2 t^\alpha}\left[e\underbrace{\phi_b(\epsilon, T)}_{2} - \underbrace{\Delta E_C(\epsilon, T)}_{3} + \underbrace{(E_F - E_C^\gamma)(\epsilon, T)}_{4}\right]. \tag{5.9}$$

The different terms in this equation are labelled 1-4 for compact referencing. To calculate term 1 in (5.9), the polarization charge needs to be obtained. Let P_{sp} and P_{pz} represent the spontaneous and strain-dependent piezoelectric polarization components. Term 1 can then be written at the 2DEG

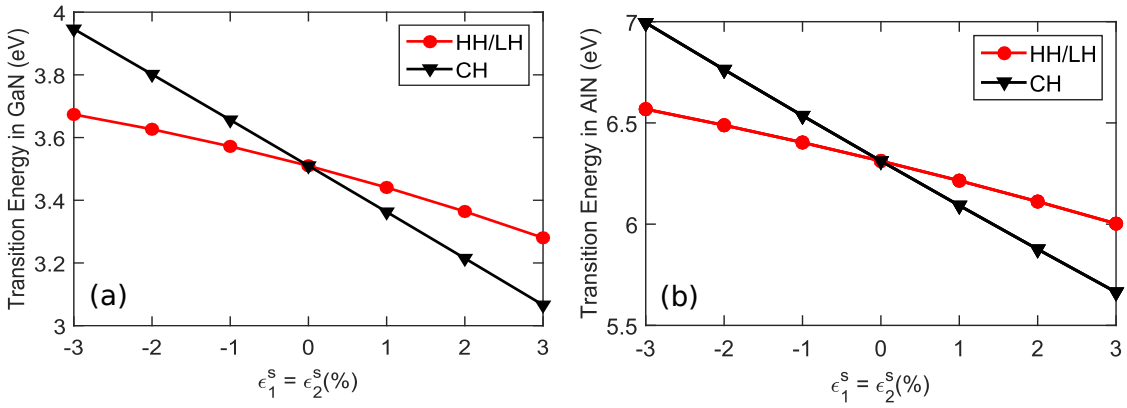

Figure 5.3: Transition energies from the HH/LH and the CH valence bands to the conduction band in AlN and GaN, based on [174] for a large applied strain range of ±3%. These values are calculated at a temperature of 0 K assuming no initial strain. ©2016 IOP.

interface using the difference in these polarization components at the 2DEG interface as [52]

$$q_p^{\alpha}(\epsilon) - q_p^{\gamma}(\epsilon) = (P_{sp}^{\gamma} - P_{sp}^{\alpha}) + (P_{pz}^{\gamma}(\epsilon) - P_{pz}^{\alpha}(\epsilon)) \quad \text{where,} \tag{5.10}$$

$$P_{sp}(x) = -p_1 x - p_2(1-x) + p_3 x(1-x), \tag{5.11}$$

$$P_{pz}(\epsilon) = \epsilon_1 e_{31} + \epsilon_2 e_{31} + \epsilon_3 e_{33}, \tag{5.12}$$

$$P_{pz}^{\mathrm{AlN}}(\epsilon) = -1.808\epsilon_1 + 5.624\epsilon_1^2 \quad \epsilon_1 < 0, \tag{5.13}$$

$$P_{pz}^{\mathrm{AlN}}(\epsilon) = -1.808\epsilon_1 - 7.888\epsilon_1^2 \quad \epsilon_1 > 0, \tag{5.14}$$

$$P_{pz}^{\gamma}(\epsilon) = -0.918\epsilon_1 + 9.541\epsilon_1^2. \tag{5.15}$$

Equations (5.11) − (5.12) are valid for both AlGaN and GaN. In (5.11), x is the mole fraction of Al in AlGaN and is usually around 20-30% [167]. The spontaneous and piezoelectric polarization coefficients are represented by p_i and e_{ij}, respectively. The linear relation in (5.12) is accurate for small strain levels, typically less than ∼0.2%. For the large strain range in this work, especially for the biaxial case, the piezoelectric charge is non-linear with applied strain, thus the relations (5.13) − (5.15) are used [52] instead of (5.12). The band offset in term 3 of (5.9) is related to the

difference in the band-gap energies (E_G) of AlGaN and GaN [175]:

$$\Delta E_C(\epsilon, T) = 0.7(E_G^{\alpha}(\epsilon, T) - E_G^{\gamma}(\epsilon, T)) \quad \text{where,} \tag{5.16}$$

$$E_G(\epsilon, T) = E_G(\epsilon, T = 0\text{ K}) - \frac{vT^2}{T + w}\ . \tag{5.17}$$

Here, $E_G(\epsilon, T = 0\text{ K})$ is the band-gap at 0 K for biaxial strain ϵ. The change in the band-gap with temperature is less than 0.1 eV from 300-500 K, however, this is accounted for using the standard Varshni band-gap parameters [176] v and w for GaN and AlN. In order to calculate the change in positions of the valence and conduction band of AlGaN and GaN due to strain, we use the relations derived in the **k.p** method from Yan et al. [177, 174]. With no strain in AlN or GaN, the top three valence bands (VB) include a pair of degenerate heavy (HH) and light (LH) hole bands, as well as a slightly lower crystal-field split-off (CH) band. Biaxial strain preserves the symmetry of the wurtzite system, thus it does not split the HH/LH valence band at the Γ point. The HH/LH hole band is the upper-most valence band when the biaxial strain is negative or not present. When the biaxial strain in the system in the system is positive, the CH band rises above the HH and LH bands and becomes the upper-most valence band, which makes it necessary to consider in this analysis. The change in the positions of the conduction and valence band edge (ΔE_{CB}, $\Delta E_{\text{VB}}^{\text{HH/LH}}$, $\Delta E_{\text{VB}}^{\text{CH}}$) due to strain are [174]:

$$\Delta E_{\text{CB}} = \alpha_{cz}\epsilon_3 + \alpha_{ct}(\epsilon_1 + \epsilon_2) + b_1\epsilon_3^2 + b_2(\epsilon_1 + \epsilon_2)^2, \tag{5.18}$$

$$\Delta E_{\text{VB}}^{\text{HH/LH}} = (D_1 + D_3)\epsilon_3 + (D_2 + D_4)(\epsilon_1 + \epsilon_2) - b_3\epsilon_3^2 - b_4(\epsilon_1 + \epsilon_2)^2, \tag{5.19}$$

$$\Delta E_{\text{VB}}^{\text{CH}} = D_1\epsilon_3 + D_2(\epsilon_1 + \epsilon_2). \tag{5.20}$$

Here, $\alpha_{cz}, \alpha_{ct}, D_1 - D_4$ represent conduction and valence band deformation potentials, while b_1, b_2, b_3 and b_4 represent bowing parameters to account for second-order nonlinearities. The recommended values of these parameters were obtained from [174]. With the relations (5.18) – (5.20) and (5.16) – (5.17), the band offset $\Delta E_C(\epsilon, T)$ in term 3 of (5.9) can be calculated. The calculated change in the band-gap of GaN and AlN based on these relations due to strain is shown in Figure 5.3.

In order to calculate the temperature-and strain-dependent barrier height $\phi_b(\epsilon, T)$ which is needed in (5.9), a Ni gate contact is assumed for simplicity. The effect of applied strain on ϕ_b with the temperature held constant is apparent from the band-diagram in Figure 5.2, which indicates an increase in the ϕ_b due to positive (tensile) strain, and vice-versa. This is expected since a positive

strain leads to additional negative piezoelectric charge at the gate-AlGaN surface, which is compensated by the creation of more positive surface donor charges as discussed previously, thus increasing ϕ_b. This effect has been recently verified experimentally by Yao et al. using suspended GaN-on-Si structures [115] for small applied strains up-to $\sim \pm 1.5 \times 10^{-4}$. For the large strain range in this work, the position of the conduction band edge at the Schottky contact itself changes in addition to the previous affect (as discussed in (5.18)), which affects the electron affinity χ^α that is needed to determine ϕ_b. Following [115], the barrier height is estimated using a simple Schottky model [178] as:

$$\phi_b(\epsilon, T) = \phi_{\mathrm{Ni}}(300\ \mathrm{K}) + \zeta_{\mathrm{Ni}} T - \chi^\alpha(\epsilon_s) + \frac{q_p^\alpha(\epsilon_s)}{e^2 D_{\mathrm{it}}} \quad \text{where,} \tag{5.21}$$

$$\chi^\alpha(\epsilon) = \chi^\alpha_{300\ \mathrm{K}}(\epsilon_s = 0\%) + \Delta E_{\mathrm{CB}}, \tag{5.22}$$

In the preceding equations, ϕ_{Ni} and ζ_{Ni} represent the gate metal work function and the temperature coefficient, respectively. D_{it} is the constant density of interface states on the AlGaN surface, as discussed previously. Note from (5.21) that the change in ϕ_b is small for large D_{it} since only a small number of states need to be ionized to compensate the 2DEG charge, and vice-versa. If D_{it} is not constant for the specific Schottky-AlGaN interface, (5.21) might need to be adjusted as a function of energy accordingly. It should also be noted that the amount of interface charge generated from D_{it} could change from temperature due to the Fermi distribution of the traps along the band-gap (especially in the deep levels), however, this effect is ignored in this analysis to keep the model simple [179]. The electron affinity of AlGaN χ^α is a weak function of temperature [180], thus only its strain-dependence is accounted for. The value of χ^α at 300 K in (5.22) for no applied strain is interpolated from known values of χ for GaN and AlN [181].

Since E_F is below E_C at the 2DEG, $E_F - E_C^\gamma$, which is term 4 of (5.9), is calculated using degenerate Fermi-Dirac semiconductor statistics. Let the thickness of the 2DEG in the 3-direction to be t_{2DEG}. Then, assuming the charge is linearly distributed along this thickness [175], it is possible to relate the volume charge density n_v to n_s:

$$n_v(\epsilon, T) = \frac{2 n_s(\epsilon, T)}{t_{\mathrm{2DEG}}}. \tag{5.23}$$

In order to relate $E_F - E_C^\gamma$ to n_v, the reduced chemical potential η and the reduced carrier concentration r are defined:

$$\eta(\epsilon, T) = \frac{E_F - E_C^\gamma}{k_b T} \tag{5.24}$$

$$r(\epsilon, T) = \frac{n_v}{N_c^\gamma}, \tag{5.25}$$

where $N_c^\gamma(\epsilon, T) = 2\left[\frac{2\pi k_b T m_{\text{eff}}(\epsilon)}{h^2}\right]^{3/2}$.

Here, N_c^γ is the conduction band density-of-states in GaN. In order to calculate the electron effective mass, an average over the 1 and 2 directions is used. Thus $m_{\text{eff}}(\epsilon) = \sqrt{m_1(\epsilon)m_2(\epsilon)}$, where m_1 and m_2 are the effective masses in the 1 and 2 directions. The values of these effective masses are $0.198m_0$ and $0.197m_0$ without strain by Chu et al. [182], where m_0 is the electron rest mass. The average in-plane (1- and 2-directions) effective mass change per 0.1% biaxial strain is calculated to be $\sim -2.7\%$ from [182], making it possible to determine $N_c^\gamma(\epsilon, T)$ in (5.25). η and r are related by the Nilsson approximation [183] of the Fermi-Dirac integral:

$$\eta(\epsilon, T) = \frac{\ln r}{1-r} + \left(\frac{3\sqrt{\pi}r}{4}\right)^{\frac{2}{3}} + \frac{8\sqrt{\pi}r}{3(4+\sqrt{\pi}r)^2}. \tag{5.26}$$

Using (5.26) and (5.23)$-$(5.25), it is possible to relate $E_F - E_C^\gamma$ at the 2DEG interface to n_s, making (5.9) an implicit equation that can be solved for it in terms of temperature and strain.

Fundamentally, the 2DEG channel mobility μ is dependent on the collision time τ_c and the m_{eff} of the 2DEG electrons. The effect of temperature is to predominantly change τ_c, while the effect of strain is to change m_{eff}, which was discussed previously. Room temperature mobility of the 2DEG is dependent on the quality of the material sample. For the purposes of modeling, it is assumed that the 2DEG has a low concentration of ionized impurities ($\ll 10^{17}$ cm^{-3}) [184], under which the idealized temperature-dependence of the mobility is given by [185]

$$\mu(T) = \mu_0 \left(\frac{T}{300}\right)^{-\theta_T} \tag{5.27}$$

where μ_0 is the mobility at 300 K and θ_T is the temperature coefficient of mobility. A standard value of $\mu_0 = 1600$ cm^2·V^{-1}s^{-1} and $\theta_T = 1.5$ is used [185], which arises from the increase in the 2DEG electron-optical phonon scattering rate with elevated temperature. Thus, the strain-and temperature-dependence of the 2DEG sheet conductivity can be analytically calculated.

Analysis

Using the constants from Table 5.1, Figure 5.4 depicts plots of n_s and ϕ_b for a typical AlGaN/GaN on Si wafer with $x = 0.25$ and the thickness of AlGaN set to 30 nm. Note that these results are

for a biaxial strain, which makes the gauge factors obtained here larger than uniaxial gauge factors reported in literature. The properties of AlGaN are assumed to be linear interpolations between AlN and GaN. The change in the charge density and the barrier height, Δn_s and $\Delta\phi_b$ for two cases of D_{it} within a small strain range of $\pm 0.1\%$ is illustrated in (a) and (b) at 300 K. $\Delta\phi_b$ is small with larger D_{it}, as discussed earlier. When $\Delta\phi_b$ is small, the difference in the piezoelectric polarization charge largely determines the strain response of the 2DEG, leading to a positive Δn_s with increase in strain as can be seen in (a), which is in accordance for most values reported in literature [160]. However, when $\Delta\phi_b$ is large, a negative Δn_s with increase in strain is predicted, as can be seen in (a), which agrees with recently reported results [115]. Even from this simple model where D_{it} is assumed to be constant, it is observed that its value can lead to large variability in the gauge factor, which might explain the $\sim$4 orders of variation in existing literature in addition to possible measurement inaccuracy [160]. For this small biaxial strain range, using a linear approximation and accounting for the mobility dependence on strain via the effective mass change described previously, a biaxial gauge factor of $\sim$-20 to -30 is calculated for the smaller and larger D_{it}, respectively. These values are comparable to former simulation results [160]. The negative gauge factor for the larger D_{it} case is expected, however, even for the smaller D_{it}, a negative value was obtained because of the increase in mobility with positive ϵ_s. Figure 5.4c shows the temperature response of n_s from 300-500 K at a D_{it} of 5×10^{13} $\text{cm}^{-2}\cdot\text{eV}^{-1}$ for a small strain range ($\pm 0.1\%$). For a given strain level, increase in temperature lowers ϕ_b, thus increasing n_s marginally. Finally, panel (d) of Figure 5.4 depicts Δn_s for the larger D_{it} case at 300 K over the full applied strain range of $\pm 1\%$, accounting for all the nonlinearities discussed previously. For negative ϵ_s, almost no change in n_s is predicted because the applied strain acts in opposition to the existing lattice mismatch strain of $\sim$0.6% in AlGaN. Finally, for this particular D_{it}, a quadratic response with a negative gauge factor is seen for positive ϵ_s, predominantly arising due to the relations (5.13) – (5.15). The analysis thus suggests that Δn_s is heavily dependent on D_{it}, and that specific interface state engineering strategies could be adopted from other device architectures [186] to precisely manipulate the gauge factor.

5.1.4 Electrical model

In this subsection, the $I_D - V_G$ characteristics of the HEMT are discussed as functions of temperature and applied strain. The major temperature-and strain-dependencies are manifested via the threshold voltage, the channel saturation velocity, and the 2DEG mobility, which was discussed previously. Since the charge in the 2DEG is known, the strain-and temperature-dependent threshold voltage

Table 5.1: Model constants.

Property	Value		Property	Value
	GaN	AlN		
C_{11} (GPa) [52]	367	396	t^{α} (nm)	30
C_{12} (GPa) [52]	135	137	ϕ_{Ni} (300 K, eV) [175]	5.15
C_{13} (GPa) [52]	103	108	ζ_{Ni} (eV·K^{-1}) [175]	-5.6×10^{-4}
C_{33} (GPa) [52]	405	373	D_{it} (cm$^{-2}\cdot$eV^{-1})	$4\times10^{12}-5\times10^{13}$
a (300 K, nm) [52]	0.3189	0.3112	μ_0 (cm^2·V^{-1}s^{-1}) [185]	1600
c (300 K, nm) [52]	0.5185	0.4982	θ_T [185]	1.5
$\kappa(\times10^{-11}$, F·m$^{-1})$ [52]	8.4075	7.965	t_{2DEG} (nm) [175]	3
e_{31} (C·m^{-2}) [52]	-0.34	-0.53	R_S, R_D (Ω)	10
e_{33} (C·m^{-2}) [52]	0.67	1.5	L_G, W_G (µm)	10, 100
$E_G(0)$ (eV) [175]	3.51	6.312	p_1, p_2, p_3 (C·m^{-2}) [52]	-0.090, -0.034, 0.021
v (meV·K^{-1}) [175]	0.909	1.799	$\chi^{\mathrm{GaN}}, \chi^{\mathrm{AlN}}$ (eV) [181]	4.2, 2.05
w (K) [175]	830	1462	T_g (K)	1400

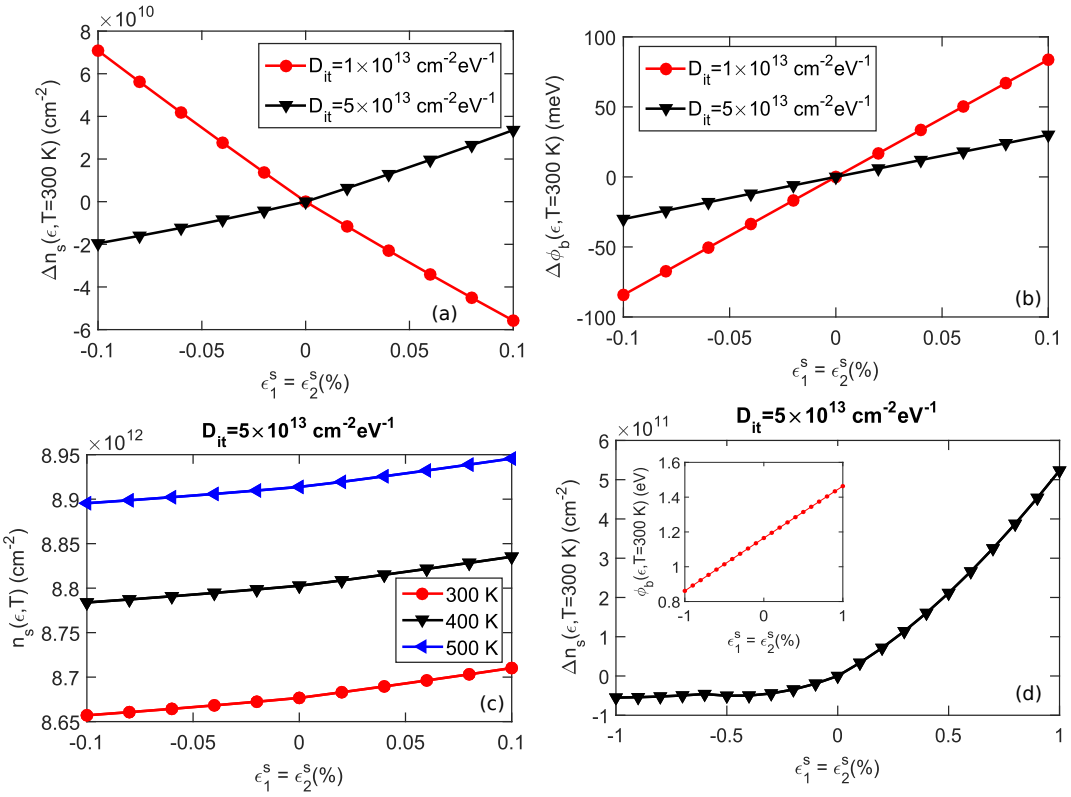

Figure 5.4: Strain-and temperature-dependence of the 2DEG sheet density n_s and Schottky barrier height ϕ_b as a function of the interface state density D_{it} at the Schottky-AlGaN interface. ©2016 IOP.

V_{th} defined as the voltage required to turn off the HEMT is easily determined since the capacitance of the AlGaN layer is known:

$$V_{\text{th}}(\epsilon, T) = -\frac{n_s(\epsilon, T) e t^{\alpha}}{\kappa^{\alpha}}. \tag{5.28}$$

From (5.28), $V_{\text{th}}(\epsilon, T)$ is calculated to be a range of values ∼-5 V for our model case.

Assuming that the optical phonon energies in the 2DEG are not affected by strain, $v_{\text{sat}}(\epsilon, T)$ is (approximately) evaluated as [175, 187, 188]:

$$v_{\text{sat}}(\epsilon, T) \sim \sqrt{\frac{n_s(\epsilon_s = 0\%)}{n_s(\epsilon_s)}} \frac{1.4 \times 10^7}{0.85 + \frac{0.15T}{300}} \text{ cm} \cdot \text{s}^{-1}. \tag{5.29}$$

The drain and source contact resistances, R_S and R_D are assumed to be equal to 10 Ω, while the drain voltage V_D is assumed to 1 V for our model case. It is assumed that the V_D has no effect on V_{th}. The gate length L_G and width W_G are taken to be 10 µm and 100 µm, respectively. For simplicity, the channel length is taken to be L_G. These values are arbitrary (but realistic) constants and do not affect the response trends of the HEMT. Although in practice a small decrease in contact resistance is expected with increase in temperature, it is reasonable to assume it to be constant as it is ohmic [175]. Given these parameters, a simple drift-diffusion model that is accurate for moderate temperatures up-to ∼500 K is used to evaluate the small-signal characteristics of the HEMT. Details of this model can be found elsewhere [189, 175]. It is noted that the results from this model are not accurate for devices with smaller gate sizes (sub-half micron devices), in which scenario a different model should be used [190]. Further, the model does not account for quantum corrections due to tunneling normal to the AlGaN/GaN interface, which could be important for thinner AlGaN layers and high enough temperatures [191].

The calculated strain response of the HEMT for biaxial strain is depicted in the $I_D - V_G$ response plots in Figure 5.5a-c for decreasing D_{it}. Distinct lines are obtained for each ϵ_s, quantified by a ΔI_D for a given V_G which is a measure of the strain sensitivity of the 2DEG. Due to large decrease in channel mobility, ∼60% drop in I_D is observed in (a) from 300 to 500 K. Due to the reversal of the trend of Δn_s with strain that was discussed earlier, a flip in the strain response characteristic is observed as we shift from higher to lower D_{it}. The different strain response lines in (b) and (c) intersect each other because of the opposing trends of the μ and V_{th} with ϵ_s. As we shift towards even lower D_{it} values, the flip in the strain response characteristic occurs at progressively higher V_G, as seen by comparing (b) and (c). While the trend in (a) is traditionally associated with HEMT strain behaviour [160], behaviour of type (b) has been observed in recent literature [164, 115].

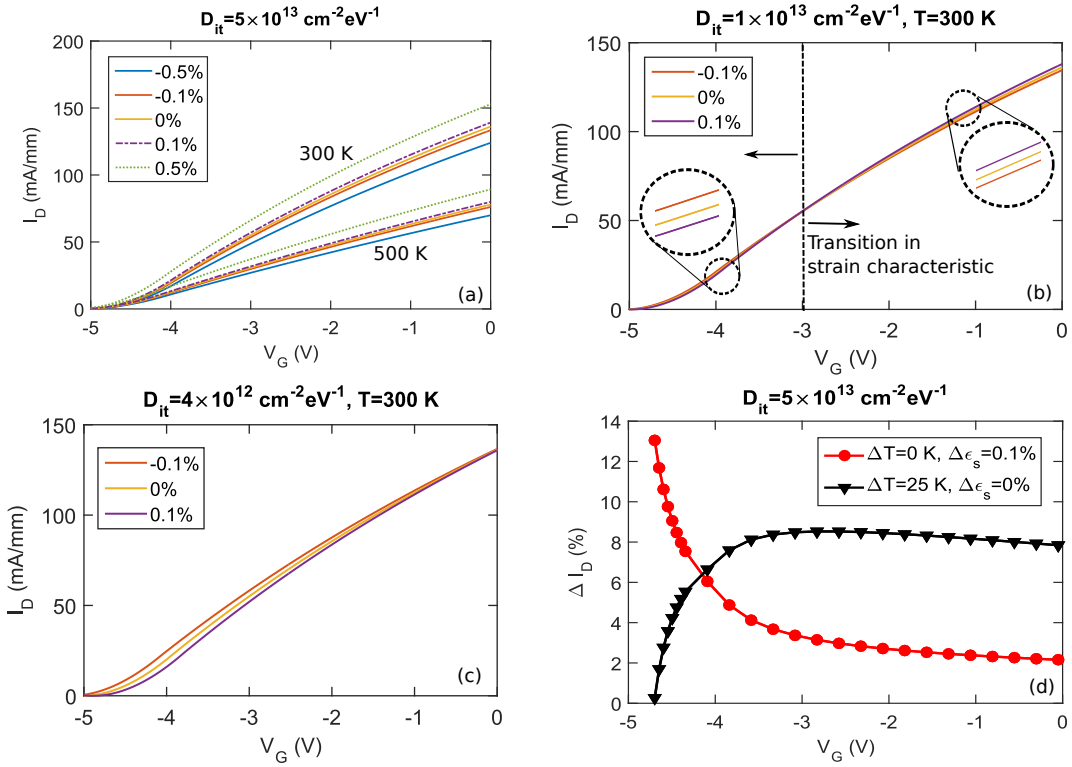

Figure 5.5: (a)-(c) Current-Voltage characteristics of the HEMT channel as a function of strain, temperature and D_{it} at $V_D = 1$. The zoomed in regions are only to show the order of the lines when they are close. A flip in the strain response characteristic is observed in (b) at a gate voltage of ∼-3 V. (d) Plot of numerically modeled $\Delta I_D(\%)$ for 0.1% ϵ_s with a temperature fluctuation from 300-325 K. ©2016 IOP.

Finally, there have been discussions of operation near V_{th} to enhance strain sensitivity in recent literature [165, 164]. This effect is depicted in Figure 5.5d, which show shows not only an increase in the strain sensitivity (red line), but a decrease in the temperature sensitivity (black line) as we approach V_{th}, which is ∼-5 V for the chosen HEMT parameters. In (d), the strain sensitivity at 300 K (red line) is defined as the percent change in I_D for $\epsilon_s = 0.1\%$ relative to the value at no strain. In order to define the temperature sensitivity (black line), ϵ_s was held at 0 % and the percent change in current from 300 to 325 K was calculated at each V_G. The choice of 300 to 325 K was arbitrary, but represents a realistic value of the temperature fluctuation that could be expected in environment where the HEMT might be used to sense strain. For this particular choice of parameters, an operation point ∼-4.8 V enables temperature compensation and boosts strain sensitivity to ∼13% change in current for 0.1% ϵ_s. Recently published experimental results

for AlGaN/GaN HEMT pressure sensors and cantilevers at room temperature confirm the strain response observed in Figure 5.5d [165, 164]. For example, Boulbar et al. demonstrate up-to 40% change in ΔI_D for V_G near V_{th} for a HEMT under biaxial strain on a circular membrane subjected to a differential pressure [164]. While the exact change in ΔI_D depends on the HEMT and the D_{it} distribution, this technique is broadly applicable for strain sensing using HEMTs.

5.1.5 Conclusion and Future Work

In this section, a comprehensive, semi-empirical model (using first-principles) of the effects of temperature, strain and the interface state density on the device characteristics of AlGaN/GaN HEMTs was presented for the first time. The quantitative variation in the current-voltage response of the HEMT due to the combined effect of strain and temperature was discussed. The results from the model are useful for deciding the optimal HEMT parameters for sensing applications. Significant amplification of the strain sensitivity is predicted by operating the 2DEG as a HEMT instead of a resistor, confirming that AlGaN/GaN HEMTs can be effectively used for strain sensing in high-temperature environments. For devices where strain sensing with minimal cross talk due to temperature effects is the objective (such as pressure sensors based on AlGaN/GaN) it is useful to operate in a biaxial strain configuration in the temperature-compensated region. For devices where external strain effects are not desirable (such as those arising out of packaging) or applications where temperature sensing is the objective, it is recommended to operate the HEMT with $V_G \gg V_{\text{th}}$ to avoid device shift. It is noted that the value of the interface state density has a profound impact on the strain response characteristics of HEMTs, and that its value could be optimally tuned to control sensitivity. Future work involves experimentally testing the these response curves across the modeled temperature range with different interface state densities to verify the model. Neglected aspects of the model, such as self-heating of the HEMT and accounting for temperature and geometry dependent strain relaxation could be incorporated to extend the scope of our work. In addition, future research involves developing predictions of strain sensing using other III-V material combinations, such as AlInN and InGaN, as well as other heterostructured material families with large differences in piezoelectric constants by extending the current model.

5.2 A High Responsivity, Low Dark Current Ultraviolet Photodetector using the AlGaN/GaN 2DEG

In this section, we discuss the fabrication and operation of a high-performance photodetector that uses the polarization fields in AlGaN/GaN to obtain high sensitivity.

5.2.1 Introduction

UV photodetectors have applications in diverse fields, including combustion flame detection, UV astronomy and satellite positioning [192, 193]. GaN is an appealing materials platform for manufacturing UV photodetectors due to the maturity of GaN high electron mobility transistor (HEMT) fabrication technology, in addition to its ability to operate in high-temperature and radiation-rich environments [194]. In most applications, the ideal photodetector would exhibit a high responsivity to maximize the signal, in addition to a low dark current to minimize quiescent power. A performance metric which simultaneously captures these two values is the normalized photocurrent-to-dark current ratio (NPDR), defined as the ratio of responsivity to dark current, with units of W^{-1}[195, 196]. Numerous photodetector architectures [193, 197, 198, 199, 200, 201, 202, 203, 204, 205] have been demonstrated in GaN, with a broad range of reported responsivities and NPDRs, as summarized in Table 5.2. Table 5.2 additionally reports the UV-visible rejection-ratio, another important performance metric which determines the cross-sensitivity of the photodetector to visible light. A distinction can be drawn between devices with a responsivity that corresponds to less than 100% quantum efficiency [198, 199] (0.29 $A{\cdot}W^{-1}$ for 365 nm illumination), and those with a responsivity that exceeds this value [197, 200, 201, 202, 203]. In the latter category of photodetectors, which includes photoconductors [201], phototransistors [200, 206] and some metal-semiconductor-metal (MSM) photodetectors [197, 207], an internal gain mechanism must exist where each incident photon induces more than one electron in the conduction band. The gain (G) is defined as the ratio of charge carriers to the photon flux [9]:

$$G = \frac{hc}{e\lambda}\frac{I}{P} \tag{5.30}$$

where I is the photocurrent, λ is the wavelength of incident radiation and P is the incident power. One particularly high gain photodetector architecture is the phototransistor; AlGaN/GaN phototransistors have been shown to achieve gains as high as 170,000 [200]. Though these devices have a high gain, their fabrication requires the use of both n-and p-doped GaN [200]. Due to the high

Table 5.2: Performance of Various Photodetector Architectures Demonstrated in GaN.

Type	Responsivity ($A \cdot W^{-1}$)	NPDR (W^{-1})	UV/Vis	Bias (V)	References
MSM	3.1	3×10^{12}	10^5	10	[197]
p-i-n diode	0.15	2×10^{9}	10^3	10	[198]
Avalanche	0.13	2×10^{10}	10^4	20	[199]
Phototransistor	50000	5×10^{14}	10^8	3	[200]
Photoconductor	13000	4×10^{8}	10^2	1	[201]
HEMT	3000	2×10^{6}	10^3	10	[202]
Meander	10000	8×10^{12}	10^4	5	[203]
Sliced HEMT	33	1×10^{12}	10^3	5	[204]
2DEG IDT	7800	6×10^{14}	10^6	5	This work

activation energies of all known acceptor-type dopants in GaN [208], it is desirable to fabricate photodetectors which do not require doping. It is further desirable to fabricate devices compatible with HEMT fabrication, in order to leverage mature GaN technology and enable monolithic integration. Previous HEMT photodetectors [202, 209], which leverage the modulation of the AlGaN/GaN 2DEG sheet density under UV illumination, have been shown to have a high gain, however such devices also have high dark current, leading to some of the lowest NPDRs among reported devices ($\sim10^6$). Recent work [203, 204] has shown that by introducing an intrinsic GaN channel between two 2DEG electrodes, a high NPDR can be achieved. Understanding the gain mechanism of such photodetectors is important for maturing this promising class of devices. In this section, we present such a device with a record high NPDR (6×10^{14}). In addition, the device has a responsivity (7,800 $A \cdot W^{-1}$), and UV-visible rejection-ratio (10^6) that are among the highest reported values. We propose that our device has a similar gain mechanism to that of a phototransistor, in a device architecture that is significantly simpler to fabricate, requiring two masks, and no doping. Evidence for this gain mechanism is provided by investigating the scaling of gain with channel length and incident power.

5.2.2 Fabrication

Devices were fabricated on an AlGaN/GaN-on-Si wafer (DOWA, Inc.) grown by metal-organic chemical vapor deposition (MOCVD). The III-nitride stack, illustrated schematically in Figure 5.6a, consists of a 1.5 -µm-thick strain management buffer structure and an active 1.2-µm-thick GaN layer grown on top of Si (111). Subsequent to the growth of the GaN layer, formation of the 2DEG was accomplished by growing an epitaxial stack consisting of a 1-nm-thick AlN spacer, 30-nm-thick $Al_{0.25}Ga_{0.75}N$ barrier layer and 1-nm-thick GaN capping layer. This wafer has a manufacturer specified 2DEG mobility of 1,400 $cm^2 \cdot V^{-1}s^{-1}$ and sheet density of 1×10^{13} cm^{-2} at room temperature.

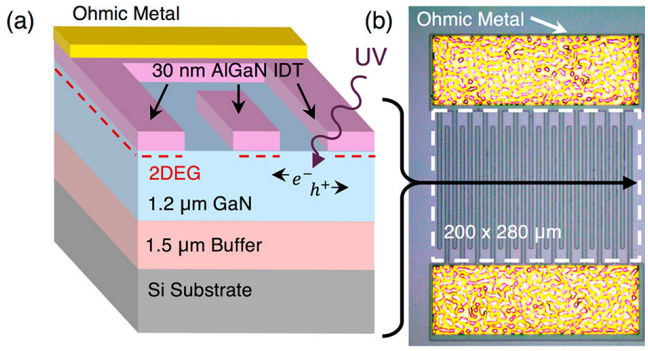

Figure 5.6: (a) Schematic illustration of material stack. (b) Optical image of fabricated device. ©2016 ACS.

As shown in Figure 5.6b, an array of 2DEG interdigitated transducers (2DEG-IDT) was fabricated by etching AlGaN 2DEG mesa electrodes. The mesa etch was performed using an inductive coupled plasma with BCl_3/Cl_2 gases to a depth of 60 nm. These 5-µm-wide 2DEG electrodes were separated by 5-µm-wide intrinsic (un-intentionally doped below 10^{16} cm^{-3}) GaN buffer channels. Post mesa isolation, a standard Ti/Al/Pt/Au Ohmic metal stack was deposited, and activated with a 35 second, 850°C anneal [67]. After this two-step process, the fabrication of the 2DEG IDT photodetectors was completed, however it should be noted that the wafer received subsequent processing for co-fabricated devices. In particular, standard MSM photodetectors were fabricated on the GaN buffer, using the same geometry as the 2DEG-IDT photodetectors. These devices (Pd-MSM) had Pd/Au (40 nm/10 nm) metal fingers in place of the AlGaN mesa electrodes for comparison studies.

5.2.3 Measurements and Gain Mechanism

Responsivity measurements were taken using a 365 nm UV lamp and semiconductor parameter analyzer (henceforth Setup I). All presented measurements were taken at room temperature. The results of these measurements for a characteristic 2DEG-IDT and Pd-MSM device under 1.5 $mW{\cdot}cm^{-2}$ optical power are shown in Figure 5.7a. While both devices have a comparable, low dark current of ∼10 pA, the 2DEG-IDT device has significantly higher photocurrent, corresponding to a responsivity of 2,500 $A{\cdot}W^{-1}$ at 5 V, in contrast to the 0.78 $A{\cdot}W^{-1}$ responsivity observed in the MSM photodetector at the same bias voltage. Though the 2DEG-IDT device has significantly higher responsivity, both devices have a responsivity which exceeds the 100% quantum efficiency limit (0.29 $A{\cdot}W^{-1}$ for 365 nm illumination), indicating the presence of a gain mechanism in both devices.

To further probe the gain mechanism in the 2DEG-IDT device, we measured responsivity while varying the UV intensity across four orders of magnitude. These measurements are presented in Figure 5.7b. Measurements with incident power above 0.010 mW·cm^{-2} were DC measurements performed with Setup I, and those with power below 0.010 mW·cm^{-2} were AC measurements, performed using a lock-in amplifier and a monochromated optical beam chopped at 200 Hz (henceforth Setup II). These data show that as power increases from 0.15 µW·cm^{-2} to 110 µW·cm^{-2}, the responsivity increases dramatically by greater than 4 orders of magnitude, peaking at 7,800 A·W^{-1}. Above 110 µW·cm^{-2}, the responsivity decreases slightly to 2,500 A·W^{-1} at 1.5 mW·cm^{-2} This increase in responsivity with increasing incident power, and subsequent saturation is consistent with previous reports of high gain GaN MSM photodetectors [207], however opposite of the trend seen in phototransistors [200]. Measurements of the transient response of the 2DEG-IDT device were

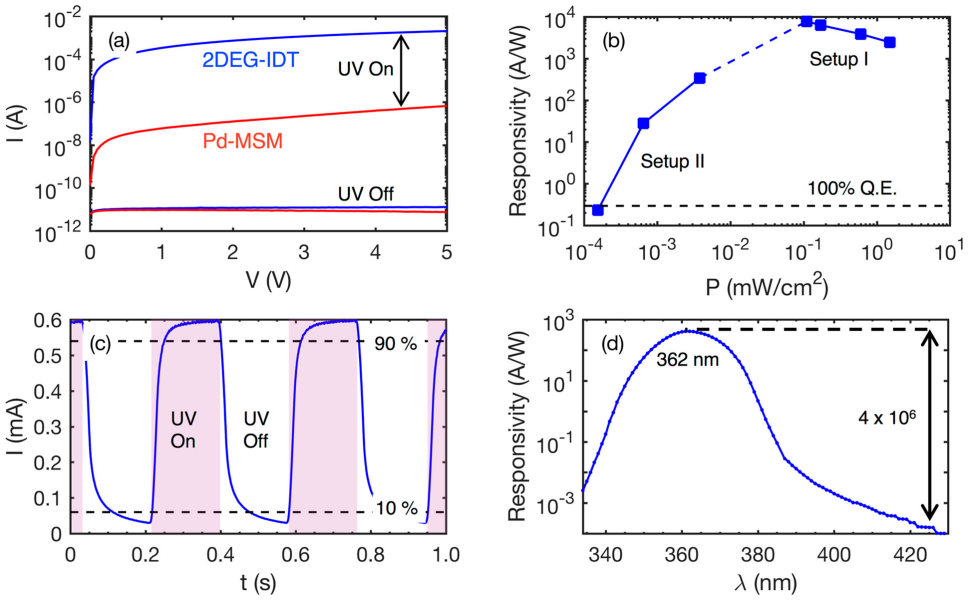

Figure 5.7: a) UV photoresponse of characteristic 2DEG-IDT and MSM devices exposed to 1.5 mW·cm^{-2} UV power. (b) Responsivity as a function of incident power, with the responsivity corresponding to 100% Q.E. labelled. Measurements below 0.010 mW·cm^{-2} were performed using Setup II, those above 0.010 mW·cm^{-2} were performed with Setup I. (c) Transient measurement of 2DEG-IDT response to 0.17 mW·cm^{-2} 365 nm illumination chopped at 5 Hz, measured in Setup I. (d) Responsivity vs. wavelength, measured in Setup II. Measurements in (b,c,d) were at a bias voltage of 5 V. ©2016 ACS.

conducted using Setup I with an optical chopper operating at 5 Hz. These measurements, presented in Figure 5.7c, demonstrate rise and fall times of 32 ms and 76 ms, respectively, here defined as the time it takes the photocurrent to go from 10% to 90% of its final value. It is also observed that

within a 200 ms window the photocurrent does not recover to its ∼10 pA dark state value, indicating the presence of persistent photoconductivity [210], common to AlGaN/GaN 2DEG photodetector devices. These rise and fall times are long relative to MSM photodetectors with no internal gain [193], however they present a significant improvement on the 20 s rise and 60 s fall time observed in a photoconductor with comparable gain to our 2DEG-IDT device [201].

Measurements of responsivity as a function of wavelength were also performed using Setup II. These data, shown in Figure 5.7d, demonstrate a high UV-visible rejection ratio of 4×10^6, with a peak responsivity at ∼362 nm. The broadband light source used in this measurement had a roughly constant intensity between 1 and 3 µW·cm^{-2} below the peak responsivity at 362 nm, and an increasing intensity between 3 and 28 µW·cm^{-2} as the wavelength increased from 362 to 430 nm. Because the responsivity of the 2DEG-IDT photodetector increases with incident power (as seen in Figure 5.7), this measurement underestimates the true UV-visible rejection ratio. The band-pass nature of the spectral responsivity of this photodetector, where the responsivity decreases at wavelengths both below and above the GaN band gap (∼365 nm), is consistent with previous reports of phototransistors [200, 206], indicating a similar gain mechanism in both devices.

We seek to explain the gain observed in both device architectures, in particular the extraordinarily high gain of 26,000 observed in the 2DEG-IDT. In order to understand the scaling laws of the gain mechanisms in MSM and 2DEG-IDT photodetectors, devices were fabricated where the intrinsic GaN channel length between the Pd and 2DEG electrodes was varied from 4 to 20 µm. Optical microscope images of the MSM and 2DEG-IDT structures are shown in the inserts of Figure 5.8a and 5.8(b) respectively. Figures 5.8 and 5.8b show the gain vs. $1/L^2$, where L is the spacing between the Pd and 2DEG electrodes respectively. These data show that while there is a clear linear relation, with zero y-intercept, between gain and $\frac{1}{L^2}$ for the 2DEG-IDT photodetectors (Figure 5.8b), the same relation does not describe the gain vs. $\frac{1}{L^2}$ relation in the MSM photodetectors (Figure 5.8a). This difference in length scaling, in addition to the vastly different response magnitudes, implies that different gain mechanisms are present in these two types of devices. In the standard model of gain in photoconductors, which has been used by Kumar et al. [204] to describe the gain of an InAlN/GaN device with a similar architecture to this work, gain is due to carrier accumulation that is limited by recombination, leading to the following scaling law: $G = \frac{\mu_e \tau_r V}{L^2}$, where μ_e is the electron mobility, τ_r is the recombination time and V is the applied voltage. Though this model reproduces the appropriate $\frac{1}{L^2}$ dependency, using a bulk mobility of 900 cm^2·V^{-1}s^{-1}, which is appropriate for our unintentional doping concentration [211], a recombination time of ∼3 µs is required to fit our data.

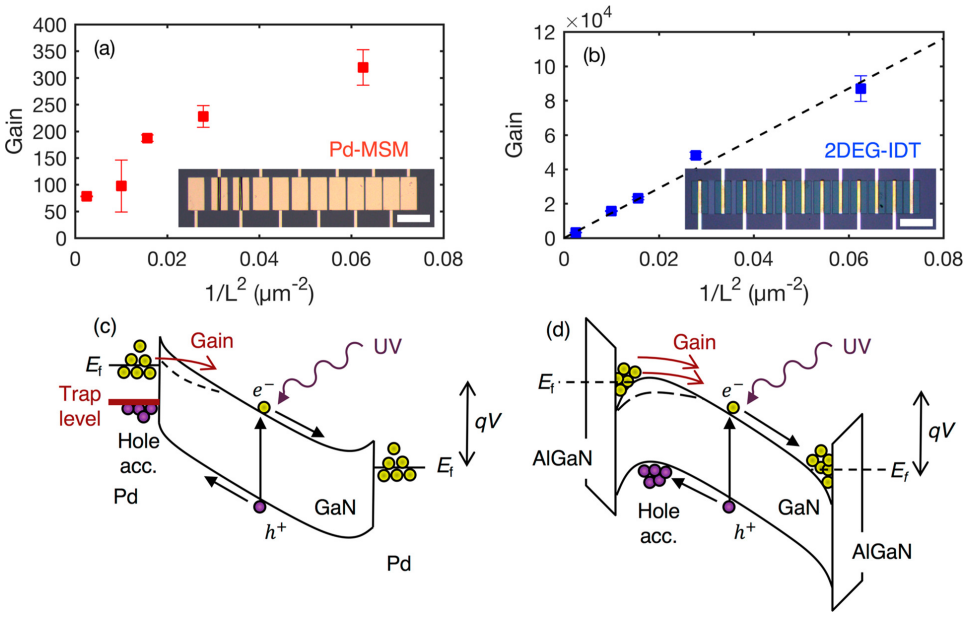

Figure 5.8: Comparison of internal gain vs. length for (a) Pd-MSM and (b) 2DEG-IDT photodetectors. Error bars represent response biasing photodetector at ±5 V. Inserts show microscope images of fabricated devices with spacing of 4-20 µm, scale bars represent 100 µm. It is observed that there is a linear proportionality between gain and $\frac{1}{L^2}$ for the 2DEG-IDT device (black dashed line), but not for the Pd-MSM device. Band structures for the Pd-MSM and 2DEG-IDT photodetectors under applied bias are found in (c) and (d) respectively. Dashed lines in GaN conduction band represent electrostatic barrier lowering due to photon-induced hole accumulation. ©2016 ACS.

This value is three orders of magnitude larger than the previously reported ∼6 ns minority carrier lifetimes in GaN [212]. Because the ∼3 µs recombination time required to fit the standard model is unreasonable, a different gain mechanism is needed to describe the behavior of our 2DEG-IDT devices.

The proposed gain mechanism is schematically illustrated in the band diagram for a 2DEG-IDT photodetector presented in Figure 5.8d. In the 2DEG-IDT device, an AlGaN/GaN valence band offset creates an energetic barrier which leads to hole accumulation at this interface. This hole accumulation leads to an electrostatic lowering of the energetic barrier for electrons in the 2DEG to escape the quantum well and enter the conduction band (dashed line in Figure 5.8d). Using only the lowermost sub-band, the number of carriers per unit volume with sufficient energy to escape the 2DEG quantum well can be approximately written as:

$$n_e(\phi_b) \approx \frac{k_B T m^*}{\pi \hbar^2} e^{\frac{-q(\phi_b - \Delta\phi_b)}{k_b T}} \tag{5.31}$$

where m^* is the effective mass, ϕ_b is the energy separation between the Fermi level in the 2DEG and the top of the GaN conduction band in the dark state, and $\Delta\phi_b$ is the barrier lowering due to photon-induced hole accumulation (Figure 5.8d). Assuming that all electrons with sufficient energy enter the conduction band, and that electron conduction between the 2DEG electrodes is due to drift, the gain is found to be:

$$G = \frac{n_e(\phi_b)}{n_{ph,tot}} \frac{\mu_e V}{L} \tag{5.32}$$

where $n_{ph,tot}$ is the total number of photons incident on the device. Evidence for a drift model comes from the fact that the photocurrent shown in Figure 5.7a is approximately linear with applied voltage. This drift model can further explain the $\frac{1}{L^2}$ dependency of gain if $n_e(\phi_b) \propto F_{ph}$, where F_{ph} is photon flux per unit area, because $n_{ph,tot} = F_{ph}L$. Using a mobility of 900 $\text{cm}^2 \cdot \text{V}^{-1}\text{s}^{-1}$, the barrier height required to explain the observed photocurrents is 150 meV. This order of magnitude is consistent with theoretical values for ϕ_b, calculated to be ~100 meV using a commercial Schrödinger-Poisson solver [55]. The exponential nature of the model in (5.32) further explains the observation in Figure 5.7b, where increasing incident power increases responsivity, up to a point of saturation. At low incident powers, when $\phi_b - \Delta\phi_b \approx \phi_b$, small changes in $\Delta\phi_b$ lead to small changes in the number of conduction electrons. However, when $\phi_b - \Delta\phi_b$ is lowered at high incident powers, the same small change in $\Delta\phi_b$ will lead to an exponentially larger change in the number of conduction electrons. This continues until reaching a point of saturation where non-idealities, such as increased recombination in the channel and the AlGaN/GaN interface, lead to a divergence from this model. This gain mechanism is similar to that of a phototransistor, where minority carrier accumulation in the base lowers the base-emitter energetic barrier, allowing more majority carriers to be injected from the emitter.

The band structure of an MSM photodetector, schematically illustrated in Figure 5.8c has no barrier to hole conduction into the metal, in contrast to the 2DEG-IDT device. Thus, in order for spatial hole accumulation to occur, which is necessary to achieve a gain greater than unity, a trap state must exist at the metal contact. The gain due to such a trap state would be limited by the density of trap states and the de-trapping time, thus the assumption $n_e(\phi_b) \propto F_{ph}$ is unlikely to hold. This explains the fact that gain in the Pd-MSM photodetector is not linearly proportional to $\frac{1}{L^2}$. Though trap states could exist at the AlGaN/GaN interface, the difference in the scaling of the gain with length in these devices indicates that trap states do not play the same role in determining the gain of the 2DEG-IDT device as they do in the Pd-MSM device.

5.2.4 Conclusion

In this section, we demonstrated a 2DEG-IDT photodetector with a record high NPDR ($6x10^{14}$), in addition to a high responsivity (7,800 $A{\cdot}W^{-1}$) and UV-visible rejection-ratio (10^6) using the polarization fields at the AlGaN/GaN interface. The observed 32/76 ms rise/fall times present significant improvements on the 20/60 s rise/fall times seen in a photoconductor with comparable gain. We argue that the gain mechanism in this device is similar to that of a phototransistor, where spatial hole accumulation leads to a lowering of the energy barrier for electrons entering the conduction band. This mechanism is consistent with the scaling of gain with incident power and device channel length. The simple, two-mask fabrication process further allows for monolithic integration of our device with AlGaN/GaN HEMTs, enabling on-chip integration of optical sensing systems using this material platform.

Chapter 6

Concluding Remarks and Future Work

6.1 Conclusions

In this thesis, we discussed the merits of the AlGaN/GaN 2DEG for energy harvesting and sensing applications, outside its traditional use case scenario (RF and power electronics). The results which we have discussed suggest a monolithically integrated AlGaN/GaN-on-Si system, with sufficient maturation of logic, sensing, and power delivery, as an enabling technology for extreme environment IoT applications. In this, thesis, we primarily focussed on a wide temperature range ($\sim$77 K to $\sim$300°C) as our definition of extreme environment. Although this is limited in scope, the mechanical strength and radiation hardness of GaN suggest that the platforms fabricated in this thesis should be operational in other harsh environments too.

In the first segment of this thesis (Chapter 3 and Chapter 4), we attempted to understand the merits of the AlGaN/GaN 2DEG for thermoelectric energy harvesting (a first study of its kind). This is in contrast with traditional research on III-nitride thermoelectrics, which largely focuses on cross-plane transport in doped layers. We argued in Chapter 2 that the small thickness of such layers will not lead to good thermoelectric performance, and we should focus on in-plane transport, specifically trying to maximize the thermoelectric power factor. The AlGaN/GaN 2DEG satisfies both these requirements. As shown in Chapter 3, the thermoelectric power factor of the AlGaN/GaN 2DEG reaches state-of-the-art values (4-7$\times 10^{-3}$ W$\cdot$m^{-1}K^{-2} at room temperature)

with little degradation as the temperature increased to 300°C. We also attempted to optimize the thermoelectric performance by reducing the thickness of the buffer layers, in the hope that it would reduce the thermal conductivity without disturbing the power factor. The thermal conductivity was reduced (up to a factor of 2.5x at room temeperature), keeping the electrical properties similar. On the whole, the thermoelectric figure of merit (zT), for a single 2DEG was found to be about ∼4x the best reported value for III-nitride materials to date (InGaN) [43].

While improvement in material properties (such as the thermoelectric power factor) is one approach to increase power density, an alternate approach, is to use 3D, folded surfaces to keep the footprint same but increase the power density, which is important for µTEGs. We explored such an idea in Chapter 3 by measuring the thermoelectric properties of AlGaN/GaN films grown on an inverted pyramidal geometry. Although the buffer layers had a high level of unintenional doping that contributed to the thermoelectric properties, we found a large, ∼14x improvement in the thermoelectric power factor. This increase was partly due to the boost in the effective conductivity of the film (because of the larger cross-sectional area). However, perhaps surprisingly, we also found a large increase in the Seebeck coefficient (from ∼297 μV·K^{-1} for flat film to ∼849 μV·K^{-1}) due to a gradual composition change (from GaN rich to AlN rich) along the walls of the pyramid. While this study only explored room temeprature thermoelectric properties, the idea of using geometry optimization for thermoelectric energy harvesting needs to be further explored.

In Chapter 4, we looked at the low temeperature thermoelectric properties of the 2DEG, where we measured the properties for 2DEGs with "thick" and "thin" buffers. Our findings showed that while S_{ph} is ∼32% of the total S at room temperature in a thick ∼1.2 µm device, S_{ph} is almost completely suppressed when t_{GaN} is reduced to ∼100 nm. Phonon drag also lead to state-of-the-art thermoelectric power factor in the thick GaN sample. By measuring the thermal conductivity in these samples, we showed that the magnitude of the phonon drag can increase even when the thermal conductivity is decreasing. This decoupling of k and S_{ph} could enable significant advancements in thermoelectric power conversion. These first measurements of the thermoelectric properties of the AlGaN/GaN 2DEG in the low temperature range, are an important step toward understanding drag in such low-dimensional systems.

In the second segment of this thesis (Chapter 5), we explored some novel sensing mechanisms enabled by the AlGaN/GaN 2DEG. We first explored electron transport in the AlGaN/GaN 2DEG under the combined influence of applied strain and temperature via a model. The results from the model are useful for deciding the optimal HEMT parameters for sensing applications (e.g., strain and

pressure). Significant amplification of the strain sensitivity is predicted by operating the 2DEG as a HEMT instead of a resistor, confirming that AlGaN/GaN HEMTs can be effectively used for strain sensing in high-temperature environments. We specifically found that operating in a biaxial strain configuration near the threshold voltage is useful for enhancing the strain sensitivity. After looking at strain sensing, we switched gears to photodetectors. Our photodetector used the AlGaN/GaN 2DEG for its electrodes, in contrast to metal that typically used. In the presence of UV light, the large band offset at the AlGaN/GaN interface lead to holes being trapped at the GaN valence band-edge, lowering the conduction band and releasing additional 2DEG electrons. This led to record high NPDR (6x10^{14}), in addition to a high responsivity (7,800 A·W^{-1}) and UV-visible rejection-ratio (10^{6}). These experiments were only done at room temperature, but futher high-and-low temperature experiments, as well as radiation exposure, are required to study extreme environment operation.

In terms of an overall summary, we learned that manipulation of the polarization fields intrinsic to GaN devices can lead to unusual, but promising applications in energy harvesting and sensing. GaN devices may not able to compete with Si-based devices for low-voltage, room-temperature applications. However, they may become the building blocks for electronic and sensing systems that are essential for hostile environments, which need to be probed, for example, to improve the energy-efficiency of our infrastructure (e.g. combustion engines) as well as space exploration.

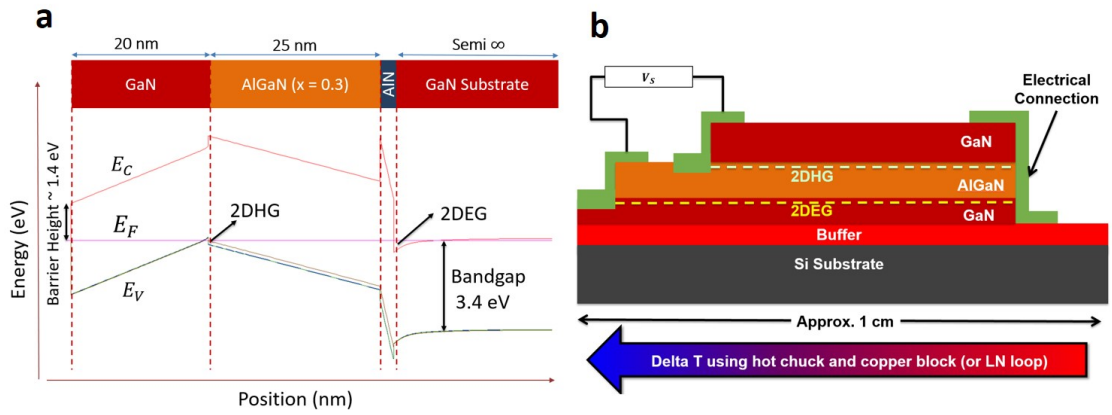

Figure 6.1: (a) Band diagram of a AlGaN/GaN heterostructure with a thick GaN cap, showing the 2DHG at the GaN cap/AlGaN interface. (b) A 2DEG-2DHG thermocouple.

6.2 Future Work

Some recommendations for further work are as follows:

- A single 2DEG is too resistive for practical thermoelectric applications. A superlattice, where alternating layers of AlGaN and GaN, with a thickness of a few microns, needs to be investigated as the n-type thermoelectric element. As discussed earlier in this thesis, such superlattices have been made on sapphire substrate, and their thermoelectric properties have been measured at room temperature [65]. Thus, a guideline for future work is to study the thermoelectric properties of suspended superlattices on optimized buffer structures, such as those in Chapter 3.

- We have only focused on n-type 2DEGs as thermoelectric elements in this thesis. Practical thermoelectric devices need both n-and-p-type elements. Although we could simply use a metal instead of the p-type element, that would heavily compromise thermoelectric performance. Thus, further research is needed into making p-type elements within the AlGaN/GaN 2DEG. With the polarization fields, it is currently possible to make two-dimensional hole gases (2DHGs), but such elements have low mobilties (below $\sim$30 $cm^2 \cdot V^{-1}s^{-1}$ at room temperature [30, 31]) today. These can be made by simply extending the thickness of the capping layer in the GaN/AlGaN/AlN/GaN buffer system. An example is shown in Figure 6.1a, where the thickness of the capping layer is set to 20 nm. A 2DHG is seen at the GaN cap/AlGaN interface. The low hole mobilites suggest that further innovations are required to improve the performance of such a p-type element in GaN or other compatible material platforms.

- Once a 2DEG and a 2DHG are placed next to each other, an innovative thermoelectric architecture that connects these can be thought of. An example is shown in Figure 6.1b, where the temperature gradient runs along the 2DEG and the 2DHG, thus we expect the output voltage to add up. In this Figure, it is assumed that the 2DEG and the 2DHG are not interacting with each other. However, very recent theoretical research shows that if these electron-hole layers can be brought sufficiently close, an exciton (bound state of an electron and hole) thermoelectric could be produced, with potential vast improvements in efficiency [213]. An experimental realization of this, perhaps on the GaN/AlGaN/GaN system could be very exciting. Further, investigation of low resistivity contact schemes for such coupled 2DEG/2DHG systems is necessary.

- The pyramidal architecture we investiaged in this thesis contained a buffer with a high doping concentration. In future studies, this should ideally be done with an undoped buffer. Further, investigation of the growth of superlattice structures with a pyramidal geometry is necessary.

- Although phonon drag was investiaged with only a single 2DEG in this thesis, further work is necessary to understand what its effect on a superlattice (which is required for making a practical thermoelectric device) might be.
- Further extreme environment testing across a wider range of temperatures, and radiation exposure are promising avenues for all the devices described in this thesis.

Finally, GaN-based sensors, although promising in standalone, may not become commercially viable unless the supporting verticals (circuitry for information processing, memory elements, and packaging) are also developed concurrently. Careful thought into the development of these verticals constitute an important avenue for future work.

Appendix A

Mobility Model

To model the mobility in the AlGaN/GaN 2D electron gas, we need to understand the scattering rates for the electrons in the 2DEG quantum well with phonons (acoustic and optical), as well as the 2DEG interface. The electronic state for a 2D quantum well can be described by wave vector $\mathbf{k} = (k_x,k_y)$ in the plane of the AlGaN/GaN interface, and subband index n to describe the wave function along the confinement direction (z). Under this assumption, we can write the wave function and electron energy for the electrons in the bottom subband as:

$$\Psi_{n,\mathbf{k}} = \psi(z)e^{\mathrm{i}\mathbf{k}\cdot\mathbf{r}} \tag{A.1}$$

$$E_n(\mathbf{k}) = E_n + \frac{\hbar^2 k^2}{2m^*} \tag{A.2}$$

where $\mathbf{r} = (x, y)$ denotes the spatial coordinate in-the-plane of the 2DEG and E_n is the energy at the bottom of the subband corresponding to index n [214]. Figure 4.4a shows E_n as a function of temperature (50 to 300 K) with respect to the Fermi level for the bottom two subbands for the thin and thick GaN sample. Since the majority of conduction electrons ($> 90\%$) are present in the lowermost subband, we only consider the bottom subband ($n = 1$) for evaluating all the electronic transport properties (thus neglecting inter-subband scattering). To model the wave function along the confinement direction, we can use the Fang-Howard expression, where $\psi(z) = \sqrt{\frac{b^3 z^2}{2}} e^{-\frac{bz}{2}}$ [59]. Here, the parameter $b = (\frac{12m^* e^2 n_{\text{eff}}}{\epsilon\hbar^2})^{\frac{1}{3}}$, where $n_{\text{eff}} \approx \frac{11}{32} n_{2D}$ [59], assuming that the barrier layer is un-doped and all the 2DEG electrons are a result of built-in polarization fields at the AlGaN/GaN interface.

The scattering rates for electrons can be evaluated using Fermi's golden rule, for which we need

to calculate the matrix elements with the correct scattering potentials for the different mechanisms. For the sake of brevity, we will skip the details, which can be found elsewhere [59]. In our scattering picture, the 3D phonon can be represented by the wave vector $\mathbf{Q} = (\mathbf{q}, q_z)$, where $\mathbf{q}$ and q_z represent the in-plane and out-of-plane component. When an electron with initial wave vector $\mathbf{k} = (k_x, k_y)$ scatters with $\mathbf{Q}$, its final state can be written as $\mathbf{k}' = \mathbf{k}+\mathbf{q}$ from conservation of momentum in-plane. If the collision is elastic, we can write $\mid \mathbf{q} \mid = q = 2k\sin(\frac{\theta}{2})$, where θ is the angle between $\mathbf{k}$ and $\mathbf{k}'$. The in-plane scattering matrix elements (M) are identical to the ones used for scattering with 3D electrons. However, in this case, because we need to account for the out-of-plane phonon wave vector q_z, the 2D matrix scattering element is modified as

$$M_{2D}^2 = \int M^2 \mid I(q_z) \mid^2 dq_z, \tag{A.3}$$

where $I(q_z) = \int \psi(z)^2 e^{\mathrm{iq_z z}}$. Using the Fang-Howard form for $\psi(z)$, $\mid I(q_z) \mid^2$ can be simplified as $\frac{b^6}{(b^2+q_z^2)^3}$ [59]. For the purposes of calculating the AlGaN/GaN mobility, the mechanisms we consider here are scattering from acoustic phonons, optical phonons, and roughness at the AlGaN/GaN quantum well interface. In particular, scattering by ionized impurities is neglected since the AlGaN barrier layer is assumed to be un-doped. Further, only acoustic scattering via the deformation potential is considered and piezoelectric scattering is neglected as it is found to be negligible [59].

Screening of the electron-phonon interaction by the carriers themselves is important to consider for the elastic processes (in our case, for acoustic phonon scattering and roughness scattering). This is often done by scaling the matrix scattering element M_{2D} by the screening function, defined as [59]

$$S(q,T) = 1 + \frac{e^2 F(q)\Pi(q,T)}{2\epsilon q}, \tag{A.4}$$

where $q = \mid \mathbf{q} \mid$, $F(q)$ and $\Pi(q,T)$ are the form factor and the polarizability function whose definitions are well known in the literature [214]. Once $S(q)$ is known, we can calculate the scattering times $\tau(E)$ for the 2DEG electrons as functions of electron kinetic energy (E). The integrated expressions for $\tau(E)$ over the limits of the scattering angle θ (from 0 to 2π) for acoustic deformation potential scattering, $\tau_{ac}(E)$ and optical phonon scattering, $\tau_{opt}(E)$ can be found in former work [59]. For roughness scattering, we correct the expression found in former work [59] (missing a factor of π), and is correctly written as

$$\frac{1}{\tau_{ir}(E)} = \frac{m^*\Delta^2\lambda^2 e^4 n_{2D}^2}{8\pi\hbar^3\epsilon^2} \int_0^{2\pi} e^{-\frac{-q^2\lambda^2}{4}} \frac{(1-\cos\theta)}{S(q,T)^2} d\theta, \tag{A.5}$$

where Δ is the average displacement of the interface and λ is a parameter defined as the auto-correlation length [59]. In our calculations, we have set $\lambda = 7.5$ nm. In order to accurately fit the mobility data over temperature, we set values of λ corresponding to 1 nm and 2 nm for the thick GaN and thin GaN sample discussed in Chapter 4, respectively. An AFM image of the sample surface is shown in Figure 4.4b. Once the values for the different scattering times are obtained, the total scattering time $\tau(E)$ can be calculated by adding up the different scattering rates. Finally, we calculate the energy averaged scattering time as a function of temperature as

$$\tau_{\mathrm{av}}(T) = \frac{\int \tau(E) \frac{\partial f_0(E)}{\partial E} dE}{\int E \frac{\partial f_0(E)}{\partial E} dE}, \tag{A.6}$$

where $f_0(E)$ is the Fermi function and the limits of integration are from the subband bottom E_1 to ∞ (referenced to E_F). Since $n_{2D} \approx \frac{m^*(E_F - E_1)}{\pi\hbar^2}$ when using only the bottom subband, we obtain $E_1 \approx -108$ meV, which is consistent with the Schrödinger–Poisson model (Figure 4.4). Once $\tau_{av}(T)$ is calculated, the 2DEG mobility can be obtained.

Appendix B

Fabrication process for thermoelectrics

A seven-mask process to fabricate the fully-suspended AlGaN/GaN platform for thermal measurements described in Chapter 3. The AlGaN/GaN/buffer heterostructure for the thin and bulk GaN samples was grown using an in-house metal organic chemical vapor deposition (MOCVD) chamber on a Si (111) substrate. In order to define the 2DEG mesa, we etched the AlGaN/GaN layers to a depth of ∼100 nm using an inductive coupled plasma technique with BCl_3/Cl_2 gases as shown in Figure B.1a. This was followed by the deposition of ∼4 µm PECVD oxide on the backside and selectively patterned to define the Si removal region, as depicted in Figure B.1b. The Ohmic contacts to the 2DEG were patterned by depositing Ti/Al/Pt/Au (20/100/40/80 nm) followed by a rapid thermal anneal (RTA) in N_2 ambient at 850°C for 35 seconds (Figure B.1c). Next, we deposited ∼47 nm of atomic-layer deposited (ALD) Al_2O_3 followed by patterning Ti/Pt (10/100 nm) heater and sensor metal lines, as shown in Figure B.1d. To deposit Ti/Au (20/200 nm) bondpad metal, we opened vias in the ALD film using a 20:1 buffered oxide etch for ∼2 min (Figure B.1e). In order to release the AlGaN/GaN/buffer heterostructure, Si was finally etched from the backside using a deep reactive ion etching (DRIE) technique, stopping at the buffer/Si interface. X-Ray diffraction data for the AlGaN/GaN/buffer layers in available in our former work [50]. After suspension, the total thickness of the heterostructure layers was obtained as ∼1.695 µm for the thin GaN heterostructure and ∼2.85 µm for the thick GaN heterostructure from the SEM cross-section images.

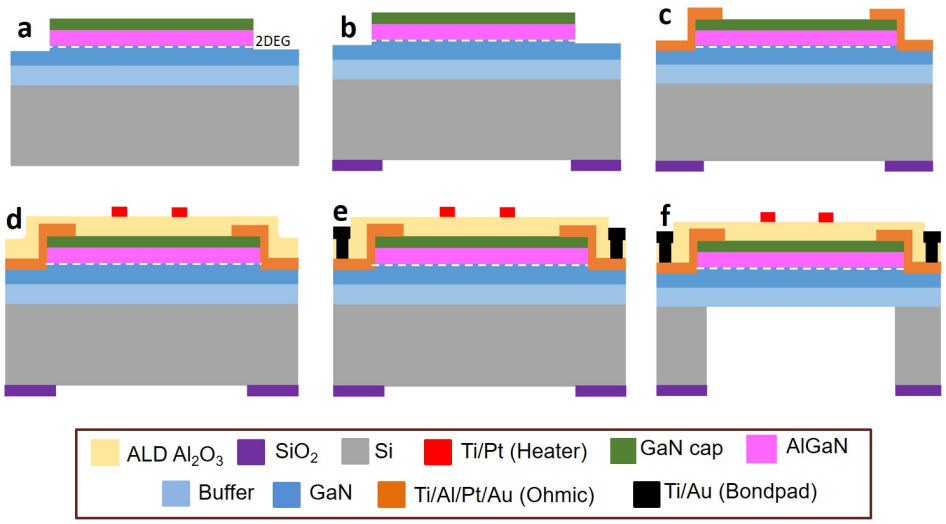

Figure B.1: Fabrication process for the thermoelectric property measurement platforms described in Chapter 3.

Appendix C

Codes

C.1 Band Diagrams

The codes to reproduce than band diagrams for the thick and the thin GaN films described in Chapter 3 and Chapter 4 are available in a GitHub repository [215].

C.2 Phonon drag simulations

The codes to model the thermal conductivity and Seebeck coefficients (diffusive and drag components) discussed in Chapter 4 are available in a GitHub repository [216].

Bibliography

[1] "IIoT Market worth 91.40 billion USD by 2023," https://www.marketsandmarkets.com/PressReleases/industrial-internet-of-things.asp, accessed: 2019-01-09.

[2] M. Mehregany, C. A. Zorman, N. Rajan, and C. H. Wu, "Silicon carbide MEMS for harsh environments," *Proceedings of the IEEE*, vol. 86, no. 8, pp. 1594–1609, Aug 1998.

[3] P. Neudeck, R. Okojie, and L. Chen, "High-temperature electronics-a role for wide bandgap semiconductors?" *Proceedings of the IEEE*, vol. 90, no. 6, pp. 1065–1076, 2002.

[4] R. W. Johnson, J. L. Evans, P. Jacobsen, J. R. Thompson, and M. Christopher, "The changing automotive environment: high-temperature electronics," *IEEE Transactions on Electronics Packaging Manufacturing*, vol. 27, no. 3, pp. 164–176, July 2004.

[5] R. Patterson, A. Hammoud, and M. Elbuluk, "Assessment of electronics for cryogenic space exploration missions," *Cryogenics*, vol. 46, no. 2, pp. 231 – 236, 2006.

[6] E. A. Gutierrez-D, J. Deen, and C. Claeys, *Low temperature electronics: physics, devices, circuits, and applications*. Elsevier, 2000.

[7] J. Y. Tsao, S. Chowdhury, M. A. Hollis, D. Jena, N. M. Johnson, K. A. Jones, R. J. Kaplar, S. Rajan, C. G. Van de Walle, E. Bellotti, C. L. Chua, R. Collazo, M. E. Coltrin, J. A. Cooper, K. R. Evans, S. Graham, T. A. Grotjohn, E. R. Heller, M. Higashiwaki, M. S. Islam, P. W. Juodawlkis, M. A. Khan, A. D. Koehler, J. H. Leach, U. K. Mishra, R. J. Nemanich, R. C. Pilawa-Podgurski, J. B. Shealy, Z. Sitar, M. J. Tadjer, A. F. Witulski, M. Wraback, and J. A. Simmons, "Ultrawide-Bandgap Semiconductors: Research Opportunities and Challenges," *Advanced Electronic Materials*, vol. 4, no. 1, p. 1600501, 2018.

[8] R. A. Guidotti, F. W. Reinhardt, and J. Odinek, "Overview of high-temperature batteries for geothermal and oil/gas borehole power sources," *Journal of Power Sources*, vol. 136, no. 2, pp. 257–262, 2004.

[9] S. Sze and K. Ng, *Physics of Semiconductor Devices*. John Wiley & Sons, Inc., 2006.

[10] N. Lu and I. Ferguson, "III-nitrides for energy production: photovoltaic and thermoelectric applications," *Semiconductor Science and Technology*, vol. 28, no. 7, p. 074023, 7 2013.

[11] M. Asif Khan, A. Bhattarai, J. Kuznia, and D. Olson, "High electron mobility transistor based on a GaN-Al_x $Ga_{1-x}N$ heterojunction," *Applied Physics Letters*, vol. 63, no. 9, pp. 1214–1215, 1993.

[12] D. Maier, M. Alomari, N. Grandjean, J.-F. Carlin, M.-A. Diforte-Poisson, C. Dua, S. Delage, and E. Kohn, "InAlN/GaN HEMTs for operation in the 1000°C regime: A first experiment," *IEEE Electron Device Letters*, vol. 33, no. 7, pp. 985–987, 2012.

[13] I. Daumiller, C. Kirchner, M. Kamp, K. Ebeling, and E. Kohn, "Evaluation of the temperature stability of AlGaN/GaN heterostructure FETs," *IEEE Electron Device Letters*, vol. 20, no. 9, p. 448, Sept 1999.

[14] S. Pearton, F. Ren, E. Patrick, M. Law, and A. Y. Polyakov, "Ionizing radiation damage effects on GaN devices," *ECS Journal of Solid State Science and Technology*, vol. 5, no. 2, pp. Q35–Q60, 2016.

[15] K.-A. Son, A. Liao, G. Lung, M. Gallegos, T. Hatake, R. D. Harris, L. Z. Scheick, and W. D. Smythe, "GaN-based high temperature and radiation-hard electronics for harsh environments," *Nanoscience and Nanotechnology Letters*, vol. 2, no. 2, pp. 89–95, 2010.

[16] A. Ionascut-Nedelcescu, C. Carlone, A. Houdayer, H. Von Bardeleben, J.-L. Cantin, and S. Raymond, "Radiation hardness of gallium nitride," *IEEE Transactions on Nuclear Science*, vol. 49, no. 6, pp. 2733–2738, 2002.

[17] D. G. Senesky, H. So, A. J. Suria, A. S. Yalamarthy, S. R. Jain, C. A. Chapin, H. C. Chiamori, and M. Hou, *Gallium Nitride Microelectronics for High-Temperature Environments*, ch. 12, pp. 395–433.

[18] I. Yonenaga and K. Motoki, "Yield strength and dislocation mobility in plastically deformed bulk single-crystal GaN," *Journal of Applied Physics*, vol. 90, no. 12, pp. 6539–6541, 2001.

[19] K. E. Petersen, "Silicon as a mechanical material," *Proceedings of the IEEE*, vol. 70, no. 5, pp. 420–457, 1982.

[20] M. G. Ancona, S. C. Binari, and D. J. Meyer, "Fully coupled thermoelectromechanical analysis of GaN high electron mobility transistor degradation," *Journal of Applied Physics*, vol. 111, no. 7, p. 074504, 2012.

[21] C. A. Chapin, R. A. Miller, K. M. Dowling, R. Chen, and D. G. Senesky, "InAlN/GaN high electron mobility micro-pressure sensors for high-temperature environments," *Sensors and Actuators A: Physical*, vol. 263, pp. 216–223, 2017.

[22] L. C. Popa and D. Weinstein, "2DEG electrodes for piezoelectric transduction of AlGaN/GaN MEMS resonators," in *2013 Joint European Frequency and Time Forum and International Frequency Control Symposium, EFTF/IFC 2013*, 2013, pp. 922–925.

[23] M. Hou, H. So, A. J. Suria, A. S. Yalamarthy, and D. G. Senesky, "Suppression of Persistent Photoconductivity in AlGaN/GaN Ultraviolet Photodetectors Using in Situ Heating," *IEEE Electron Device Letters*, vol. 38, no. 1, pp. 56–59, 2017.

[24] C.-F. Lo, L. Liu, B.-H. Chu, F. Ren, S. J. Pearton, S. Doré, C.-H. Hsu, J. Kim, A. M. Dabiran, and P. P. Chow, "Carbon monoxide detection sensitivity of ZnO nanorod-gated AlGaN/GaN high electron mobility transistors in different temperature environments," *Journal of Vacuum Science & Technology B, Nanotechnology and Microelectronics: Materials, Processing, Measurement, and Phenomena*, vol. 30, no. 1, p. 010606, 2012.

[25] S. J. Pearton, B. S. Kang, S. Kim, F. Ren, B. P. Gila, C. R. Abernathy, J. Lin, and S. N. G. Chu, "GaN-based diodes and transistors for chemical, gas, biological and pressure sensing," *Journal of Physics: Condensed Matter*, vol. 16, no. 29, pp. R961–R994, 7 2004.

[26] P. Offermans and R. Vitushinsky, "NO_2 Detection With AlGaN/GaN 2DEG Channels for Air Quality Monitoring," *IEEE Sensors Journal*, vol. 13, no. 8, pp. 2823–2827, 2013.

[27] R. A. Miller, H. So, H. C. Chiamori, A. J. Suria, C. A. Chapin, and D. G. Senesky, "A microfabricated sun sensor using GaN-on-sapphire ultraviolet photodetector arrays," *Review of Scientific Instruments*, vol. 87, no. 9, p. 095003, 2016.

[28] P. F. Satterthwaite, A. S. Yalamarthy, N. A. Scandrette, A. K. Newaz, and D. G. Senesky, "High Responsivity, Low Dark Current Ultraviolet Photodetectors Based on Two-Dimensional Electron Gas Interdigitated Transducers," *ACS Photonics*, vol. 5, no. 11, pp. 4277–4282, 2018.

[29] Y. Cai, Z. Cheng, Z. Yang, C. W. Tang, K. M. Lau, and K. J. Chen, "High-temperature operation of AlGaN/GaN HEMTs direct-coupled FET logic (DCFL) integrated circuits," *IEEE Electron Device Letters*, vol. 28, no. 5, pp. 328–331, 2007.

[30] Z.-H. Zhang, S. Tiam Tan, Z. Kyaw, W. Liu, Y. Ji, Z. Ju, X. Zhang, X. Wei Sun, and H. Volkan Demir, "p-doping-free InGaN/GaN light-emitting diode driven by three-dimensional hole gas," *Applied Physics Letters*, vol. 103, no. 26, p. 263501, 2013.

[31] H. Hahn, B. Reuters, A. Pooth, B. Holländer, M. Heuken, H. Kalisch, and A. Vescan, "p-channel enhancement and depletion mode GaN-based HFETs with quaternary backbarriers," *IEEE Transactions on Electron Devices*, vol. 60, no. 10, pp. 3005–3011, 2013.

[32] J. Yan, X. Liao, D. Yan, and Y. Chen, "Review of Micro Thermoelectric Generator," *Journal of Microelectromechanical Systems*, vol. 27, no. 1, pp. 1–18, 2018.

[33] S. Butera, G. Lioliou, and A. Barnett, "Temperature effects on gallium arsenide 63Ni betavoltaic cell," *Applied Radiation and Isotopes*, vol. 125, pp. 42 – 47, 2017.

[34] G. Landis, R. Rafaelle, and D. Merritt, " High temperature solar cell development," in *19th European Photovoltaic Science and Engineering Conference*, 2004.

[35] K. A. A. Khalid, T. J. Leong, and K. Mohamed, "Review on Thermionic Energy Converters," *IEEE Transactions on Electron Devices*, vol. 63, no. 6, pp. 2231–2241, June 2016.

[36] A. Elefsiniotis, N. Kokorakis, T. Becker, and U. Schmid, "A Novel High-temperature Aircraft-specific Energy Harvester Using PCMs and State of the art TEGs," *Materials Today: Proceedings*, vol. 2, no. 2, pp. 814 – 822, 2015.

[37] J. E. Köhler, R. Heijl, L. G. H. Staaf, S. Zenkic, E. Svenman, A. Lindblom, A. E. C. Palmqvist, and P. Enoksson, "High temperature energy harvester for wireless sensors," *Smart Materials and Structures*, vol. 23, no. 9, p. 095042, 2014.

[38] M. Haras and T. Skotnicki, "Thermoelectricity for IoT – A review," *Nano Energy*, vol. 54, pp. 461 – 476, 2018.

[39] T. M. Tritt and M. A. Subramanian, "Thermoelectric Materials, Phenomena, and Applications: A Bird's Eye View," *MRS Bulletin*, vol. 31, no. 3, p. 188–198, 2006.

[40] G. J. Snyder and E. S. Toberer, "Complex thermoelectric materials," *Nature Materials*, vol. 7, no. 105, 2008.

[41] J. D. Cressler, "On the potential of SiGe HBTs for extreme environment electronics," *Proceedings of the IEEE*, vol. 93, no. 9, pp. 1559–1582, 2005.

[42] A. Sztein, H. Ohta, J. Sonoda, A. Ramu, J. E. Bowers, S. P. Denbaars, and S. Nakamura, "GaN-Based Integrated Lateral Thermoelectric Device for Micro-Power Generation," *Applied Physics Express*, vol. 2, no. 11, p. 111003, 2009.

[43] A. Sztein, H. Ohta, J. E. Bowers, S. P. Denbaars, and S. Nakamura, "High temperature thermoelectric properties of optimized InGaN," *Journal of Applied Physics*, vol. 110, no. 12, p. 123709, 2011.

[44] H. Ohta, S. Kim, Y. Mune, T. Mizoguchi, K. Nomura, S. Ohta, T. Nomura, Y. Nakanishi, Y. Ikuhara, M. Hirano, H. Hosono, and K. Koumoto, "Giant thermoelectric Seebeck coefficient of a two-dimensional electron gas in SrTiO3." *Nature materials*, vol. 6, no. 2, pp. 129–134, 2007.

[45] L. Liu and J. Edgar, "Substrates for gallium nitride epitaxy," *Materials Science and Engineering: R: Reports*, vol. 37, no. 3, pp. 61 – 127, 2002.

[46] S. DenBaars and S. Keller, "Metalorganic Chemical Vapor Deposition (MOCVD) of Group III Nitrides," pp. 11 – 37, 1997.

[47] M. Zajac, R. Kucharski, K. Grabianska, A. Gwardys-Bak, A. Puchalski, D. Wasik, E. Litwin-Staszewska, R. Piotrzkowski, J. Z. Domagala, and M. Bockowski, "Basic ammonothermal growth of Gallium Nitride – State of the art, challenges, perspectives," *Progress in Crystal Growth and Characterization of Materials*, vol. 64, no. 3, pp. 63 – 74, 2018.

[48] H.-P. Lee, J. Perozek, L. D. Rosario, and C. Bayram, "Investigation of AlGaN/GaN high electron mobility transistor structures on 200-mm silicon (111) substrates employing different buffer layer configurations," *Scientific Reports*, vol. 6, no. 37588, 2016.

[49] Y. Ni, Z. He, F. Yang, D. Zhou, Y. Yao, G. Zhou, Z. Shen, J. Zhong, Y. Zhen, Z. Wu, B. Zhang, and Y. Liu, "Effect of AlN/GaN superlattice buffer on the strain state in GaN-on-Si(111) system," *Japanese Journal of Applied Physics*, vol. 54, no. 1, p. 015505, 2015.

[50] X. Xu, J. Zhong, H. So, A. Norvilas, C. Sommerhalter, D. G. Senesky, and M. Tang, "Wafer-level MOCVD growth of AlGaN/GaN-on-Si HEMT structures with ultra-high room temperature 2DEG mobility," *AIP Advances*, vol. 6, no. 11, p. 115016, 2016.

[51] O. Ambacher, J. Smart, J. R. Shealy, N. G. Weimann, K. Chu, M. Murphy, W. J. Schaff, L. F. Eastman, R. Dimitrov, L. Wittmer, M. Stutzmann, W. Rieger, and J. Hilsenbeck, "Two-dimensional electron gases induced by spontaneous and piezoelectric polarization charges in N- and Ga-face AlGaN/GaN heterostructures," *Journal of Applied Physics*, vol. 85, no. 6, p. 3222, 1999.

[52] O. Ambacher, J. Majewski, C. Miskys, A. Link, M. Hermann, M. Eickhoff, M. Stutzmann, F. Bernardini, V. Fiorentini, V. Tilak, B. Schaff, and L. F. Eastman, "Pyroelectric properties of Al(In)GaN/GaN hetero- and quantum well structures," *Journal of Physics: Condensed Matter*, vol. 14, no. 13, pp. 3399–3434, 4 2002.

[53] B. Bakeroot, S. You, T.-L. Wu, J. Hu, M. Van Hove, B. De Jaeger, K. Geens, S. Stoffels, and S. Decoutere, "On the origin of the two-dimensional electron gas at AlGaN/GaN heterojunctions and its influence on recessed-gate metal-insulator-semiconductor high electron mobility transistors," *Journal of Applied Physics*, vol. 116, no. 13, p. 134506, 2014.

[54] J. P. Ibbetson, P. T. Fini, K. D. Ness, S. P. DenBaars, J. S. Speck, and U. K. Mishra, "Polarization effects, surface states, and the source of electrons in AlGaN/GaN heterostructure field effect transistors," *Applied Physics Letters*, vol. 77, no. 2, p. 250, 2000.

[55] S. Birner, T. Zibold, T. Andlauer, T. Kubis, M. Sabathil, A. Trellakis, and P. Vogl, "nextnano : General Purpose 3-D Simulations," *IEEE Transactions on Electron Devices*, vol. 54, no. 9, pp. 2137–2142, 2007.

[56] S. Heikman, S. Keller, Y. Wu, J. S. Speck, S. P. Denbaars, and U. K. Mishra, "Polarization effects in AlGaN/ GaN and GaN/AlGaN/GaN heterostructures," *Applied Physics Letters*, vol. 93, no. 12, p. 10114, 2003.

[57] H. Tokuda, J. Yamazaki, and M. Kuzuhara, "High temperature electron transport properties in AlGaN/GaN heterostructures," *Journal of Applied Physics*, vol. 108, no. 10, p. 104509, 2010.

[58] T. T. Mnatsakanov, M. E. Levinshtein, L. I. Pomortseva, S. N. Yurkov, G. S. Simin, and M. A. Khan, "Carrier mobility model for GaN," *Solid-State Electronics*, vol. 47, no. 1, pp. 111–115, 2003.

[59] M. N. Gurusinghe, S. K. Davidsson, and T. G. Andersson, "Two-dimensional electron mobility limitation mechanisms in $Al_xGa_{1-x}N$/GaN heterostructures," *Physical Review B*, vol. 72, no. 4, p. 045316, 2005.

[60] J.-H. Bahk, T. Favaloro, and A. Shakouri, "Thin Film Thermoelectric Characterization Techniques," *Annual Review of Heat Transfer*, vol. 16, no. 30, p. 51, 2013.

[61] Z. Tian, S. Lee, and G. Chen, "Heat Transfer in Thermoelectric Materials and Devices," *Journal of Heat Transfer*, vol. 135, no. 6, p. 061605, 2013.

[62] C. Dames, "Measuring the thermal conductivity of thin films: 3 omega and related electrothermal methods," *Annual Review of Heat Transfer*, vol. 16, p. 7, 2013.

[63] G. Chen, *Nanoscale energy transport and conversion : a parallel treatment of electrons, molecules, phonons, and photons.* Oxford University Press, 2005.

[64] M. T. Dunham, M. T. Barako, S. LeBlanc, M. Asheghi, B. Chen, and K. E. Goodson, "Power density optimization for micro thermoelectric generators," *Energy*, vol. 93, pp. 2006 – 2017, 2015.

[65] A. Sztein, J. E. Bowers, S. P. DenBaars, and S. Nakamura, "Polarization field engineering of GaN/AlN/AlGaN superlattices for enhanced thermoelectric properties," *Applied Physics Letters*, vol. 104, no. 4, p. 042106, 2014.

[66] M. Hou, "Suspended Aluminum Gallium Nitride/Gallium Nitride-on-Silicon Microstructures for High-temperature-tolerant Micro-electromechanical Systems," Ph.D. dissertation, Stanford University, 2017.

[67] M. Hou and D. G. Senesky, "Operation of ohmic Ti/Al/Pt/Au multilayer contacts to GaN at 600°C in air," *Applied Physics Letters*, vol. 105, no. 8, p. 081905, 2014.

[68] Z. H. Liu, S. Arulkumaran, and G. I. Ng, "Temperature dependence of Ohmic contact characteristics in AlGaN/GaN high electron mobility transistors from -50 to 200°C," *Applied Physics Letters*, vol. 94, no. 14, p. 142105, 2009.

[69] B. Song, M. Zhu, Z. Hu, M. Qi, K. Nomoto, X. Yan, Y. Cao, D. Jena, and H. G. Xing, "Ultralow-Leakage AlGaN/GaN High Electron Mobility Transistors on Si With Non-Alloyed Regrown Ohmic Contacts," *IEEE Electron Device Letters*, vol. 37, no. 1, pp. 16–19, Jan 2016.

[70] S. Ganguly, B. Song, W. S. Hwang, Z. Hu, M. Zhu, J. Verma, H. G. Xing, and D. Jena, "AlGaN/GaN HEMTs on Si by MBE with regrown contacts and f_T = 153 GHz," *physica status solidi (c)*, vol. 11, no. 3-4, pp. 887–889, 4 2014.

[71] J.-P. Ao, A. Suzuki, K. Sawada, S. Shinkai, Y. Naoi, and Y. Ohno, "Schottky contacts of refractory metal nitrides on gallium nitride using reactive sputtering," *Vacuum*, vol. 84, no. 12, pp. 1439 – 1443, 2010.

[72] J. Hilsenbeck, W. Rieger, E. Nebauer, W. John, G. Tränkle, J. Würfl, A. Ramakrishan, and H. Obloh, "AlGaN/GaN HFETs with New Ohmic and Schottky Contacts for Thermal Stability up to 400°C," *physica status solidi (a)*, vol. 176, no. 1, pp. 183–187, 11 1999.

[73] E. Monroy, F. Calle, R. Ranchal, T. Palacios, M. Verdú, F. J. Sánchez, M. T. Montojo, M. Eickhoff, F. Omnès, Z. Bougrioua, and I. Moerman, "Thermal stability of Pt- and Ni-based Schottky contacts on GaN and $Al_{0.31}Ga_{0.69}N$," *Semiconductor Science and Technology*, vol. 17, no. 9, p. L47, 2002.

[74] A. Suria, A. Yalamarthy, H. So, and D. Senesky, "DC characteristics of ALD-grown Al_2O_3/AlGaN/GaN MIS-HEMTs and HEMTs at 600°C in air," *Semiconductor Science and Technology*, vol. 31, no. 11, 2016.

[75] A. S. Yalamarthy, H. So, M. M. Rojo, A. J. Suria, X. Xu, E. Pop, and D. G. Senesky, "Tuning Electrical and Thermal Transport in AlGaN/GaN Heterostructures via Buffer Layer Engineering," *Advanced Functional Materials*, vol. 28, no. 22, 5 2018.

[76] A. Sztein, J. E. Bowers, S. P. Denbaars, and S. Nakamura, "Thermoelectric properties of lattice matched InAlN on semi-insulating GaN templates," *Journal of Applied Physics*, vol. 112, no. 8, p. 083716, 2012.

[77] A. Sztein, J. Haberstroh, J. E. Bowers, S. P. DenBaars, and S. Nakamura, "Calculated thermoelectric properties of $In_xGa_{1-x}N$, $In_xAl_{1-x}N$, and $Al_xGa_{1-x}N$," *Journal of Applied Physics*, vol. 113, no. 18, p. 183707, 2013.

[78] J. Zhang, H. Tong, G. Liu, J. A. Herbsommer, G. S. Huang, and N. Tansu, "Characterizations of Seebeck coefficients and thermoelectric figures of merit for AlInN alloys with various In-contents," *Journal of Applied Physics*, vol. 109, no. 5, p. 053706, 2011.

[79] K. Nagase, S. Takado, and K. Nakahara, "Thermoelectric enhancement in the two-dimensional electron gas of AlGaN / GaN heterostructures," *physica status solidi (a)*, vol. 1092, no. 4, pp. 1088–1092, 2016.

[80] J. Cho, Z. Li, M. Asheghi, and K. E. Goodson, "Near-junction thermal management: thermal conduction in gallium nitride composite substrates," *Annual Review of Heat Transfer*, vol. 18, 2014.

[81] H. Ohta, S. W. Kim, S. Kaneki, A. Yamamoto, and T. Hashizume, "High Thermoelectric Power Factor of High-Mobility 2D Electron Gas," *Advanced Science*, vol. 5, no. 1, p. 1700696, 2017.

[82] M. Asheghi, K. Kurabayashi, R. Kasnavi, and K. E. Goodson, "Thermal conduction in doped single-crystal silicon films," *Journal of Applied Physics*, vol. 91, no. 8, pp. 5079–5088, 2002.

[83] I. P. Smorchkova, L. Chen, T. Mates, L. Shen, S. Heikman, B. Moran, S. Keller, S. P. DenBaars, J. S. Speck, and U. K. Mishra, "AlN/GaN and (Al,Ga)N/AlN/GaN two-dimensional electron gas structures grown by plasma-assisted molecular-beam epitaxy," *Journal of Applied Physics*, vol. 90, no. 10, pp. 5196–5201, 2001.

[84] A. Cappella, J.-L. Battaglia, V. Schick, A. Kusiak, A. Lamperti, C. Wiemer, and B. Hay, "High Temperature Thermal Conductivity of Amorphous Al_2O_3 Thin Films Grown by Low Temperature ALD," *Advanced Engineering Materials*, vol. 15, no. 11, pp. 1046–1050, 2013.

[85] M.-H. Bae, Z. Li, Z. Aksamija, P. N. Martin, F. Xiong, Z.-Y. Ong, I. Knezevic, and E. Pop, "Ballistic to diffusive crossover of heat flow in graphene ribbons," *Nat. Commun.*, vol. 4, p. 1734, 2013.

[86] H. R. Shanks, P. D. Maycock, P. H. Sidles, and G. C. Danielson, "Thermal conductivity of silicon from 300 to 1400 K," *Physical Review*, vol. 130, no. 5, pp. 1743–1748, 1963.

[87] D. K. Schroder, *Semiconductor material and device characterization.* John Wiley & Sons, 2006.

[88] A. Schmid, C. Schroeter, R. Otto, M. Schuster, V. Klemm, D. Rafaja, and J. Heitmann, "Microstructure of V-based ohmic contacts to AlGaN/GaN heterostructures at a reduced annealing temperature," *Applied Physics Letters*, vol. 106, no. 5, p. 053509, 2015.

[89] A. Fontsere, A. Pérez-Tomás, M. Placidi, P. Fernández-Martínez, N. Baron, S. Chenot, Y. Cordier, J. C. Moreno, P. M. Gammon, and M. R. Jennings, "Temperature dependence of Al/Ti-based Ohmic contact to GaN devices: HEMT and MOSFET," *Microelectronic Engineering*, vol. 88, no. 10, pp. 3140–3144, 2011.

[90] Y. Liu, X. Yang, D. Chen, H. Lu, R. Zhang, and Y. Zheng, "Determination of Temperature-Dependent Stress State in Thin AlGaN Layer of AlGaN / GaN HEMT Heterostructures by Near-Resonant Raman Scattering," vol. 2015, 2015.

[91] U. Ausserlechner, "Hall effect devices with three terminals: Their magnetic sensitivity and offset cancellation scheme," *Journal of Sensors*, vol. 2016, 2016.

[92] A. S. Yalamarthy and D. G. Senesky, "Strain- and temperature-induced effects in AlGaN / GaN high electron mobility transistors," *Semiconductor Science and Technology*, vol. 31, no. 3, p. 035024, 2016.

[93] Y. K. Koh, Y. Cao, D. G. Cahill, and D. Jena, "Heat-Transport Mechanisms in Superlattices," *Adv. Funct. Mater.*, vol. 19, no. 4, pp. 610–615, 2009.

[94] A. J. H. McGaughey, E. S. Landry, D. P. Sellan, and C. H. Amon, "Size-dependent model for thin film and nanowire thermal conductivity," *Applied Physics Letters*, vol. 99, no. 13, p. 131904, 2011.

[95] T. E. Beechem, A. E. McDonald, E. J. Fuller, A. A. Talin, C. M. Rost, J. P. Maria, J. T. Gaskins, P. E. Hopkins, and A. A. Allerman, "Size dictated thermal conductivity of GaN," *Journal of Applied Physics*, vol. 120, no. 9, p. 095104, 2016.

[96] J. Ohta, H. Fujioka, S. Ito, and M. Oshima, "Room-temperature epitaxial growth of AlN films," *Applied Physics Letters*, vol. 81, no. 13, p. 2373, 2002.

[97] W. Liu and A. A. Balandin, "Thermal conduction in $Al_xGa_{1-x}N$ alloys and thin films," *Journal of Applied Physics*, vol. 97, no. 7, p. 073710, 2005.

[98] J. Zou, D. Kotchetkov, A. A. Balandin, D. I. Florescu, and F. H. Pollak, "Thermal conductivity of GaN films: Effects of impurities and dislocations," *Journal of Applied Physics*, vol. 92, no. 5, pp. 2534–2539, 2002.

[99] E. Ziade, J. Yang, G. Brummer, D. Nothern, T. Moustakas, and A. J. Schmidt, "Thickness dependent thermal conductivity of gallium nitride," *Applied Physics Letters*, vol. 110, no. 3, p. 031903, 2017.

[100] J. Sonntag, "Disordered electronic systems. III. Thermoelectric power in alloys with phase separation," *Physical Review B*, vol. 73, no. 4, p. 045126, 2006.

[101] S. Shimizu, M. S. Bahramy, T. Iizuka, S. Ono, K. Miwa, Y. Tokura, and Y. Iwasa, "Enhanced thermopower in ZnO two-dimensional electron gas," *Proceedings of the National Academy of Sciences*, vol. 113, no. 23, pp. 6438–6443, 2016.

[102] E. Hurwitz, B. Kucukgok, L. Su, A. Melton, Z. Liu, N. Lu, and I. Ferguson, "A Systematic Study of the Thermoelectric Properties of GaN-based Wide Band Gap Semiconductors," *MRS Proceedings*, vol. 1424, pp. 145–147, 2012.

[103] B. Kucukgok, B. Wang, A. G. Melton, N. Lu, and I. T. Ferguson, "Comparison of thermoelectric properties of GaN and ZnO samples," *physica status solidi (c)*, vol. 11, no. 3-4, pp. 894–897, 2014.

[104] J.-G. Kim, C.-H. Hsieh, H. J. Choi, J. Gardener, B. Singh, A. Knapitsch, P. Lecoq, and G. Barbastathis, "Conical photonic crystals for enhancing light extraction efficiency from high refractive index materials," *Optics Express*, vol. 23, no. 17, pp. 22 730–22 739, 2015.

[105] B. W. Schneider, N. N. Lal, S. Baker-Finch, and T. P. White, "Pyramidal surface textures for light trapping and antireflection in perovskite-on-silicon tandem solar cells," *Optics Express*, vol. 22, no. 106, pp. A1422–A1430, 2014.

[106] A. S. Yalamarthy, H. So, and D. G. Senesky, "Enhancement of thermoelectric characteristics in AlGaN/GaN films deposited on inverted pyramidal Si surfaces," *Applied Physics Letters*, vol. 111, no. 2, p. 021902, 2017.

[107] H. So and D. G. Senesky, "Low-resistance gateless high electron mobility transistors using three-dimensional inverted pyramidal AlGaN / GaN surfaces," *Applied Physics Letters*, vol. 108, p. 012104, 2016.

[108] L. Shen, S. Heikman, B. Moran, R. Coffie, N.-Q. Zhang, D. Buttari, I. Smorchkova, S. Keller, S. DenBaars, and U. Mishra, "AlGaN/AlN/GaN high-power microwave HEMT," *IEEE Electron Device Letters*, vol. 22, no. 10, pp. 457–459, 2001.

[109] R. Bhat, E. Kapon, D. M. Hwang, M. A. Koza, and C. P. Yun, "Patterned quantum well heterostructures grown by OMCVD on non-planar substrates: Applications to extremely narrow SQW lasers," *Journal of Crystal Growth*, vol. 93, no. 1-4, pp. 850–856, 1988.

[110] L. Buydens, P. Demeester, M. Van Ackere, A. Ackaert, and P. Van Daele, "Thickness variations during MOVPE growth on patterned substrates," *Journal of Electronic Materials*, vol. 19, no. 4, pp. 317–321, 1990.

[111] B. Reuters, J. Strate, H. Hahn, M. Finken, A. Wille, M. Heuken, H. Kalisch, and A. Vescan, "Selective MOVPE of InGaN-based LED structures on non-planar Si (111) facets of patterned Si (100) substrates," *Journal of Crystal Growth*, vol. 391, pp. 33–40, 2014.

[112] O. Ambacher, B. Foutz, J. Smart, J. R. Shealy, N. G. Weimann, K. Chu, M. Murphy, A. J. Sierakowski, W. J. Schaff, L. F. Eastman, R. Dimitrov, A. Mitchell, and M. Stutzmann, "Two dimensional electron gases induced by spontaneous and piezoelectric polarization in undoped and doped AlGaN/GaN heterostructures," *Journal of Applied Physics*, vol. 87, no. 1, pp. 334–344, 1 2000.

[113] P. M. Asbeck, E. T. Yu, S. S. Lau, G. J. Sullivan, J. Van Hove, and J. Redwing, "Piezoelectric charge densities in AlGaN/GaN HFETs," *Electronics Letters*, vol. 33, no. 14, pp. 1230–1231, 1997.

[114] E. T. Yu, X. Z. Dang, L. S. Yu, D. Qiao, P. M. Asbeck, S. S. Lau, G. J. Sullivan, K. S. Boutros, and J. M. Redwing, "Schottky barrier engineering in III-V nitrides via the piezoelectric effect," *Applied Physics Letters*, vol. 73, no. 13, pp. 1880–1882, 1998.

[115] K. Yao, S. Khandelwal, F. Sammoura, A. Kazama, C. Hu, and L. Lin, "Piezoelectricity-Induced Schottky Barrier Height Variations in AlGaN/GaN High Electron Mobility Transistors," *IEEE Electron Device Letters*, vol. 36, no. 9, p. 902, 2015.

[116] I. Smorchkova, C. Elsass, J. Ibbetson, R. Vetury, B. Heying, P. Fini, E. Haus, S. DenBaars, J. Speck, and U. Mishra, "Polarization-induced charge and electron mobility in AlGaN/-GaN heterostructures grown by plasma-assisted molecular-beam epitaxy," *Journal of applied physics*, vol. 86, no. 8, pp. 4520–4526, 1999.

[117] X. H. Wu, L. M. Brown, D. Kapolnek, S. Keller, B. Keller, S. P. DenBaars, and J. S. Speck, "Defect structure of metal-organic chemical vapor deposition-grown epitaxial (0001) GaN/Al_2O_3," *Journal of Applied Physics*, vol. 80, no. 6, pp. 3228–3237, 1996.

[118] S. Yamaguchi, T. Matsumoto, J. Yamazaki, N. Kaiwa, and A. Yamamoto, "Thermoelectric properties and figure of merit of a Te-doped InSb bulk single crystal," *Applied Physics Letters*, vol. 87, no. 20, p. 201902, 2005.

[119] N. Miller, E. E. Haller, G. Koblmüller, C. Gallinat, J. S. Speck, W. J. Schaff, M. E. Hawkridge, K. M. Yu, and J. W. Ager, "Effect of charged dislocation scattering on electrical and electrothermal transport in n-type InN," *Phys. Rev. B*, vol. 84, p. 075315, Aug 2011.

[120] E. Pop, "Energy dissipation and transport in nanoscale devices," *Nano Research*, vol. 3, no. 3, pp. 147–169, 2010.

[121] C. Herring, "Theory of the thermoelectric power of semiconductors," *Physical Review*, vol. 96, no. 5, pp. 1163–1187, 1954.

[122] D. Cantrell and P. Butcher, "A calculation of the phonon-drag contribution to the thermopower of quasi-2D electrons coupled to 3D phonons. II. Applications," *Journal of Physics C: Solid State Physics*, vol. 20, no. 13, p. 1993, 1987.

[123] J. Zhou, B. Liao, B. Qiu, S. Huberman, K. Esfarjani, M. S. Dresselhaus, and G. Chen, "Ab initio optimization of phonon drag effect for lower-temperature thermoelectric energy conversion," *Proceedings of the National Academy of Sciences*, vol. 112, no. 48, pp. 14 777–14 782, 2015.

[124] T. H. Geballe and G. W. Hull, "Seebeck effect in Germanium," *Physical Review*, vol. 94, no. 5, pp. 1134–1140, 1954.

[125] L. Weber and E. Gmelin, "Transport Properties of Silicon," *Applied Physics A*, vol. 53, pp. 136–140, 1991.

[126] E. Conwell and V. F. Weisskopf, "Theory of impurity scattering in semiconductors," *Physical Review*, vol. 77, no. 3, pp. 388–390, 1950.

[127] G. Wang, L. Endicott, H. Chi, and P. Los, "Tuning the Temperature Domain of Phonon Drag in Thin Films by the Choice of Substrate," *Physical Review Letters*, vol. 111, no. 4, p. 046803, 2013.

[128] H. Takahashi, R. Okazaki, S. Ishiwata, H. Taniguchi, A. Okutani, M. Hagiwara, and I. Terasaki, "Colossal Seebeck effect enhanced by quasi-ballistic phonons dragging massive electrons in $FeSb_2$," *Nature Communications*, vol. 7, p. 12732, 2016.

[129] M. Koirala, H. Wang, M. Pokharel, L. Yucheng, G. Chuanfei, C. Opeil, and Z. Ren, "Nanostructured YbAgCu 4 for Potentially Cryogenic Thermoelectric Cooling," *Nano Letters*, vol. 14, no. 9, pp. 5016–5020, 2014.

[130] J. Sadhu, H. Tian, J. Ma, B. Azeredo, J. Kim, K. Balasundaram, C. Zhang, X. Li, P. M. Ferreira, and S. Sinha, "Quenched phonon drag in silicon nanowires reveals significant effect in the bulk at room temperature," *Nano Letters*, vol. 15, no. 5, pp. 3159–3165, 2015.

[131] Y. Zhang, B. Feng, H. Hayashi, C.-P. Chang, Y.-M. Sheu, I. Tanaka, Y. Ikuhara, and H. Ohta, "Double thermoelectric power factor of a 2D electron system," *Nature Communications*, vol. 9, no. 1, p. 2224, 2018.

[132] I. Pallecchi, F. Telesio, D. Marré, D. Li, S. Gariglio, J. M. Triscone, and A. Filippetti, "Large phonon-drag enhancement induced by narrow quantum confinement at the $LaAlO_3/SrTiO_3$ interface," *Physical Review B*, vol. 93, no. 19, p. 195309, 2016.

[133] M. Pokharel, H. Zhao, K. Lukas, Z. Ren, C. Opeil, and B. Mihaila, "Phonon drag effect in nanocomposite $FeSb_2$," *MRS Communications*, vol. 3, no. 1, pp. 31–36, 2013.

[134] J. Yang and T. Caillat, "Thermoelectric Materials for Space," *MRS Bulletin*, vol. 31, no. March, pp. 224–229, 2006.

[135] C. S. Gorham, J. T. Gaskins, G. N. Parsons, M. D. Losego, and P. E. Hopkins, "Density dependence of the room temperature thermal conductivity of atomic layer deposition-grown amorphous alumina (Al_2O_3)," *Applied Physics Letters*, vol. 104, no. 25, p. 253107, 2014.

[136] I. Stark, M. Stordeur, and F. Syrowatka, "Thermal conductivity of thin amorphous alumina films," *Thin Solid Films*, vol. 226, no. 1, p. 185, 1993.

[137] S. M. Lee, D. G. Cahill, and T. H. Allen, "Thermal conductivity of sputtered oxide films," *Physical Review B*, vol. 52, no. 1, pp. 253–257, 1995.

[138] I. Pallecchi, M. Codda, E. Galleani D'Agliano, D. Marré, A. D. Caviglia, N. Reyren, S. Gariglio, and J. M. Triscone, "Seebeck effect in the conducting $LaAlO_3/SrTiO_3$ interface," *Phys. Rev. B*, vol. 81, no. 8, p. 085414, 2010.

[139] B. E. Foutz, S. K. O'Leary, M. S. Shur, and L. F. Eastman, "Transient electron transport in wurtzite GaN, InN, and AIN," *Journal of Applied Physics*, vol. 85, no. 11, pp. 7727–7734, 1999.

[140] A. Davoody, E. Ramayya, L. Maurer, and I. Knezevic, "Ultrathin GaN nanowires: Electronic, thermal, and thermoelectric properties," *Physical Review B*, vol. 89, no. 11, p. 115313, 2014.

[141] R. Fletcher, V. Pudalov, Y. Feng, M. Tsaousidou, and P. Butcher, "Thermoelectric and hot-electron properties of a silicon inversion layer," *Physical Review B*, vol. 56, no. 19, pp. 12 422–12 428, 1997.

[142] N. S. Sankeshwar, M. D. Kamatagi, and B. G. Mulimani, "Behaviour of diffusion thermopower in Bloch-Grüneisen regime in AlGaAs/GaAs and AlGaN/GaN heterostructures," *physica status solidi (b)*, vol. 242, no. 14, p. 2892, 2005.

[143] J. Cho, Y. Li, W. E. Hoke, D. H. Altman, M. Asheghi, and K. E. Goodson, "Phonon scattering in strained transition layers for GaN heteroepitaxy," *Physical Review B*, vol. 89, no. 11, p. 115301, 2014.

[144] D. T. Morelli and G. A. Slack, "High Lattice Thermal Conductivity Solids," in *High Thermal Conductivity Materials*. Springer, 2006, p. 37.

[145] J. Callaway, "Model for lattice Thermal Conductivity at Low Temperatures," *Physical Review*, vol. 113, no. 4, pp. 1046–1051, 1959.

[146] B. Poudel, Q. Hao, Y. Ma, Y. Lan, A. Minnich, B. Yu, X. Yan, D. Wang, A. Muto, D. Vashaee *et al.*, "High-thermoelectric performance of nanostructured bismuth antimony telluride bulk alloys," *Science*, vol. 320, no. 5876, pp. 634–638, 2008.

[147] H. J. Ryu, Z. Aksamija, D. M. Paskiewicz, S. A. Scott, M. G. Lagally, I. Knezevic, and M. A. Eriksson, "Quantitative determination of contributions to the thermoelectric power factor in si nanostructures," *Physical Review Letters*, vol. 105, no. 25, pp. 15–18, 2010.

[148] S. Shimizu, S. Ono, T. Hatano, Y. Iwasa, and Y. Tokura, "Enhanced cryogenic thermopower in $SrTiO_3$ by ionic gating," *Phys. Rev. B*, vol. 92, no. 16, p. 165304, 2015.

[149] I. Pallecchi, F. Telesio, D. Li, A. Fête, S. Gariglio, J. M. Triscone, A. Filippetti, P. Delugas, V. Fiorentini, and D. Marré, "Giant oscillating thermopower at oxide interfaces," *Nature Communications*, vol. 6, p. 6678, 2015.

[150] J. Antoszewski, M. Gracey, J. M. Dell, L. Faraone, T. A. Fisher, G. Parish, Y. F. Wu, and U. K. Mishra, "Scattering mechanisms limiting two-dimensional electron gas mobility in $Al_{0.25}Ga_{0.75}N$/GaN modulation-doped field-effect transistors," *Journal of Applied Physics*, vol. 87, no. 8, pp. 3900–3904, 2000.

[151] W. Yim and A. Amith, "BiSb alloys for magneto-thermoelectric and thermomagnetic cooling," *Solid-State Electronics*, vol. 15, no. 10, pp. 1141–1165, 1972.

[152] D.-Y. Chung, T. P. Hogan, M. Rocci-Lane, P. Brazis, J. R. Ireland, C. R. Kannewurf, M. Bastea, C. Uher, and M. G. Kanatzidis, "A new thermoelectric material: $CsBi_4Te_6$," *Journal of the American Chemical Society*, vol. 126, no. 20, pp. 6414–6428, 2004.

[153] R. Gambino, W. Grobman, and A. Toxen, "Anomalously large thermoelectric cooling figure of merit in the Kondo systems $CePd_3$ and $Celn_3$," *Applied Physics Letters*, vol. 22, no. 10, pp. 506–507, 1973.

[154] H. Van Daal, P. Van Aken, and K. Buschow, "The seebeck coefficient of $YbAl_2$ and $YbAl_3$," *Physics letters A*, vol. 49, no. 3, pp. 246–248, 1974.

[155] K. Hippalgaonkar, Y. Wang, Y. Ye, D. Y. Qiu, H. Zhu, Y. Wang, J. Moore, S. G. Louie, and X. Zhang, "High thermoelectric power factor in two-dimensional crystals of MoS_2," *Phys. Rev. B*, vol. 95, p. 115407, Mar 2017.

[156] S. J. Pearton, B. S. Kang, S. Kim, F. Ren, B. P. Gila, C. R. Abernathy, J. Lin, and S. N. G. Chu, "GaN-based diodes and transistors for chemical, gas, biological and pressure sensing," *J. Phys. Condens. Matter*, vol. 16, no. 29, p. R961, 2004.

[157] K. Brueckner, F. Niebelschuetz, K. Tonisch, S. Michael, A. Dadgar, A. Krost, V. Cimalla, O. Ambacher, R. Stephan, and M. Hein, "Two-dimensional electron gas based actuation of piezoelectric AlGaN/GaN microelectromechanical resonators," *Applied Physics Letters*, vol. 93, no. 17, p. 173504, 2008.

[158] K. Tonisch, C. Buchheim, F. Niebelschütz, A. Schober, G. Gobsch, V. Cimalla, O. Ambacher, and R. Goldhahn, "Piezoelectric actuation of (GaN/) AlGaN/GaN heterostructures," *Journal of Applied Physics*, vol. 104, no. 8, p. 084516, 2008.

[159] M. Rais-Zadeh, V. Gokhale, A. Ansari, M. Faucher, D. Theron, Y. Cordier, and L. Buchaillot, "Gallium Nitride as an Electromechanical Material," *J. Microelectromech. Syst*, vol. 23, no. 6, p. 1252, 2014.

[160] A. D. Koehler, A. Gupta, M. Chu, S. Parthasarathy, K. Linthicum, J. Johnson, T. Nishida, and S. Thompson, "Extraction of AlGaN/GaN HEMT Gauge Factor in the Presence of Traps," *IEEE Electron Device Letters*, vol. 31, no. 7, p. 665, 2010.

[161] P. J. French and A. G. R. Evans, "Polycrystalline silicon as a strain gauge material," *J. Phys. E*, vol. 19, no. 12, p. 1055, 1986.

[162] C. A. Chapin, H. C. Chiamori, M. Hou, and D. G. Senesky, " Characterization of Gallium Nitride Heterostructures for Strain Sensing at Elevated Temperatures ," in *International Workshop on Structural Health Monitoring (2013)*, vol. 9, 2013, p. 1621.

[163] J. Dzuba, G. Vanko, I. Ryger, M. Vallo, V. Kutis, and T. Lalinsky, "Influence of temperature on the sensitivity of the AlGaN/GaN C-HEMT-based piezoelectric pressure sensor," in *Advanced Semiconductor Devices & Microsystems (ASDAM), 2014 10th International Conference on*. IEEE, 2014, p. 1.

[164] E. Le Boulbar, M. Edwards, S. Vittoz, G. Vanko, K. Brinkfeldt, L. Rufer, P. Johander, T. Lalinskỳ, C. Bowen, and D. Allsopp, "Effect of bias conditions on pressure sensors based on AlGaN/GaN High Electron Mobility Transistor," *Sensors and Actuators A: Physical*, vol. 194, pp. 247–251, 2013.

[165] H. Köck, C. A. Chapin, C. Ostermaier, O. Häberlen, and D. G. Senesky, " Emerging GaN-based HEMTs for mechanical sensing within harsh environments ," in *Proc. SPIE*, vol. 9113, 2014, p. 91130D.

[166] D. J. Chen, K. X. Zhang, Y. Q. Tao, X. S. Wu, J. Xu, R. Zhang, Y. D. Zheng, and B. Shen, "Temperature-dependent strain relaxation of the AlGaN barrier in AlGaNGaN heterostructures with and without Si3N4 surface passivation," *Applied Physics Letters*, vol. 88, no. 10, p. 102106, 2006.

[167] D. Ducatteau, A. Minko, V. Hoel, E. Morvan, E. Delos, B. Grimbert, H. Lahreche, P. Bove, C. Gaquiere, J. De Jaeger *et al.*, "Output power density of 5.1/mm at 18 GHz with an AlGaN/GaN HEMT on Si substrate," *IEEE Electron Device Letters*, vol. 27, no. 1, pp. 7–9, 2006.

[168] R. R. Reeber and K. Wang, "Lattice parameters and thermal expansion of GaN," *Journal of Materials Research*, vol. 15, no. 1, pp. 40–44, 2000.

[169] G. Steude, B. Meyer, A. Göldner, A. Hoffmann, A. Kaschner, F. Bechstedt, H. Amano, and I. Akasaki, "Strain Modification of GaN in AlGaN/GaN Epitaxial Films," *Japanese Journal of Applied Physics*, vol. 38, no. 5A, p. L498, 1999.

[170] S. Figge, H. Kröncke, D. Hommel, and B. M. Epelbaum, "Temperature dependence of the thermal expansion of AlN," *Applied Physics Letters*, vol. 94, no. 10, p. 101915, 2009.

[171] T. Zimmermann, M. Neuburger, P. Benkart, F. Hernandez-Guillen, C. Pietzka, M. Kunze, I. Daumiller, A. Dadgar, A. Krost, and E. Kohn, "Piezoelectric GaN sensor structures," *IEEE Electron Device Letters*, vol. 27, no. 5, p. 309, May 2006.

[172] B. K. Ridley, O. Ambacher, and L. F. Eastman, "The polarization-induced electron gas in a heterostructure," *Semicond. Sci. Technol.*, vol. 15, no. 3, p. 270, 2000.

[173] H. Xiao-Guang, Z. De-Gang, and J. De-Sheng, "Formation of two-dimensional electron gas at AlGaN/GaN heterostructure and the derivation of its sheet density expression," *Chin. Phys. B*, vol. 24, no. 6, p. 067301, 2015.

[174] Q. Yan, P. Rinke, A. Janotti, M. Scheffler, and C. G. Van de Walle, "Effects of strain on the band structure of group-III nitrides," *Phys. Rev. B*, vol. 90, p. 125118, Sep 2014.

[175] Y.-H. Wang, Y. C. Liang, G. S. Samudra, T.-F. Chang, C.-F. Huang, L. Yuan, and G.-Q. Lo, "Modelling temperature dependence on AlGaN/GaN power HEMT device characteristics," *Semicond. Sci. Technol.*, vol. 28, no. 12, p. 125010, 2013.

[176] Y. P. Varshni, "Temperature dependence of the energy gap in semiconductors," *physica*, vol. 34, no. 1, pp. 149–154, 1967.

[177] Q. Yan, P. Rinke, M. Scheffler, and C. G. Van de Walle, "Strain effects in group-III nitrides: Deformation potentials for AlN, GaN, and InN," *Applied Physics Letters*, vol. 95, no. 12, p. 121111, 2009.

[178] V. Bermudez, "Simple interpretation of metal/wurtzite–GaN barrier heights," *Journal of applied physics*, vol. 86, no. 2, pp. 1170–1171, 1999.

[179] M. Miczek, C. Mizue, T. Hashizume, and B. Adamowicz, "Effects of interface states and temperature on the C-V behavior of metal/insulator/AlGaN/GaN heterostructure capacitors," *Journal of Applied Physics*, vol. 103, no. 10, p. 104510, 2008.

[180] S. Grabowski, M. Schneider, H. Nienhaus, W. Mönch, R. Dimitrov, O. Ambacher, and M. Stutzmann, "Electron affinity of $Al_xGa_{1-x}N$ (0001) surfaces," *Applied Physics Letters*, vol. 78, no. 17, pp. 2503–2505, 2001.

[181] L. S. Yu, D. J. Qiao, Q. J. Xing, S. S. Lau, K. S. Boutros, and J. M. Redwing, "Ni and Ti Schottky barriers on n-AlGaN grown on SiC substrates," *Applied Physics Letters*, vol. 73, no. 2, p. 240, 1998.

[182] M. Chu, A. D. Koehler, A. Gupta, T. Nishida, and S. E. Thompson, "Simulation of AlGaN/GaN high-electron-mobility transistor gauge factor based on two-dimensional electron gas density and electron mobility," *Journal of Applied Physics*, vol. 108, no. 10, p. 104502, 2010.

[183] N. G. Nilsson, "An accurate approximation of the generalized einstein relation for degenerate semiconductors," *Phys. Status Solidi A*, vol. 19, no. 1, p. K75, 1973.

[184] M. Farahmand, C. Garetto, E. Bellotti, K. F. Brennan, M. Goano, E. Ghillino, G. Ghione, J. Albrecht, and P. Ruden, "Monte Carlo simulation of electron transport in the III-nitride wurtzite phase materials system: binaries and ternaries," *IEEE Transactions on Electron Devices*, vol. 48, no. 3, p. 535, Mar 2001.

[185] S. Vitanov, V. Palankovski, S. Maroldt, and R. Quay, "High-temperature modeling of AlGaN/GaN HEMTs," *Solid-State Electronics*, vol. 54, no. 10, p. 1105, 2010.

[186] T.-H. Hung, P. S. Park, S. Krishnamoorthy, D. N. Nath, and S. Rajan, "Interface charge engineering for enhancement-mode GaN MISHEMTs," *IEEE Electron Device Letters*, vol. 35, no. 3, pp. 312–314, 2014.

[187] V. E. Dorgan, M.-H. Bae, and E. Pop, "Mobility and saturation velocity in graphene on SiO_2," *Applied Physics Letters*, vol. 97, no. 8, p. 082112, 2010.

[188] H. Ramamoorthy, R. Somphonsane, J. Radice, G. He, C.-P. Kwan, and J. P. Bird, ""Freeing" Graphene from Its Substrate: Observing Intrinsic Velocity Saturation with Rapid Electrical Pulsing," *Nano Letters*, vol. 16, no. 1, p. 403, 2016.

[189] S. E. A. Hosseini and S. E. Hosseini, "Accurate Analytical Model for Current–Voltage and Small-Signal Characteristics of Al(m)Ga(1-m)N/GaN Modulation-Doped Field-Effect Transistors," *Japanese Journal of Applied Physics*, vol. 49, no. 7R, p. 074302, 2010.

[190] S. Vitanov, V. Palankovski, S. Maroldt, R. Quay, S. Murad, T. Rodle, and S. Selberherr, "Physics-based modeling of GaN HEMTs," *IEEE Transactions on Electron Devices*, vol. 59, no. 3, pp. 685–693, 2012.

[191] J.-R. Zhou and D. K. Ferry, "Modeling of quantum effects in ultrasmall HEMT devices," *IEEE Transactions on Electron Devices*, vol. 40, no. 2, pp. 421–427, 1993.

[192] H. Chen, K. Liu, L. Hu, A. A. Al-Ghamdi, and X. Fang, "New concept ultraviolet photodetectors," *Materials Today*, vol. 18, no. 9, pp. 493 – 502, 2015.

[193] E. Monroy, F. Omnès, and F. Calle, "Wide-bandgap semiconductor ultraviolet photodetectors," *Semiconductor Science and Technology*, vol. 18, no. 4, p. R33, 2003.

[194] R. A. Miller, H. So, H. C. Chiamori, A. J. Suria, C. A. Chapin, and D. G. Senesky, "A microfabricated sun sensor using GaN-on-sapphire ultraviolet photodetector arrays," *Review of Scientific Instruments*, vol. 87, no. 9, p. 095003, 2016.

[195] C. O. Chui, A. K. Okyay, and K. C. Saraswat, "Effective dark current suppression with asymmetric MSM photodetectors in Group IV semiconductors," *IEEE Photonics Technology Letters*, vol. 15, no. 11, pp. 1585–1587, Nov 2003.

[196] Y. An, A. Behnam, E. Pop, G. Bosman, and A. Ural, "Forward-bias diode parameters, electronic noise, and photoresponse of graphene/silicon Schottky junctions with an interfacial native oxide layer," *Journal of Applied Physics*, vol. 118, no. 11, p. 114307, 2015.

[197] S. Chang, M. Chang, and Y. Yang, "Enhanced Responsivity of GaN Metal–Semiconductor–Metal (MSM) Photodetectors on GaN Substrate," *IEEE Photonics Journal*, vol. 9, no. 2, pp. 1–7, April 2017.

[198] G. Y. Xu, A. Salvador, W. Kim, Z. Fan, C. Lu, H. Tang, H. Morkoç, G. Smith, M. Estes, B. Goldenberg, W. Yang, and S. Krishnankutty, "High speed, low noise ultraviolet photodetectors based on GaN p-i-n and AlGaN(p)-GaN(i)-GaN(n)structures," *Applied Physics Letters*, vol. 71, no. 15, pp. 2154–2156, 1997.

[199] T. Tut, M. Gokkavas, A. Inal, and E. Ozbay, "$Al_xGa_{1x}N$-based avalanche photodiodes with high reproducible avalanche gain," *Applied Physics Letters*, vol. 90, no. 16, p. 163506, 2007.

[200] W. Yang, T. Nohava, S. Krishnankutty, R. Torreano, S. McPherson, and H. Marsh, "High gain GaN/AlGaN heterojunction phototransistor," *Applied Physics Letters*, vol. 73, no. 7, pp. 978–980, 1998.

[201] L. Liu, C. Yang, A. Patanè, Z. Yu, F. Yan, K. Wang, H. Lu, J. Li, and L. Zhao, "High-detectivity ultraviolet photodetectors based on laterally mesoporous GaN," *Nanoscale*, vol. 9, pp. 8142–8148, 2017.

[202] M. A. Khan, M. S. Shur, Q. Chen, J. N. Kuznia, and C. J. Sun, "Gated photodetector based on GaN/AlGaN heterostructure field effect transistor," *Electronics Letters*, vol. 31, no. 5, pp. 398–400, March 1995.

[203] M. Martens, J. Schlegel, P. Vogt, F. Brunner, R. Lossy, J. Würfl, M. Weyers, and M. Kneissl, "High gain ultraviolet photodetectors based on AlGaN/GaN heterostructures for optical switching," *Applied Physics Letters*, vol. 98, no. 21, p. 211114, 2011.

[204] S. Kumar, A. S. Pratiyush, S. B. Dolmanan, S. Tripathy, R. Muralidharan, and D. N. Nath, "UV detector based on InAlN/GaN-on-Si HEMT stack with photo-to-dark current ratio> 10^7," *Applied Physics Letters*, vol. 111, no. 25, p. 251103, 2017.

[205] Z. Alaie, S. M. Nejad, and M. Yousefi, "Recent advances in ultraviolet photodetectors," *Materials Science in Semiconductor Processing*, vol. 29, pp. 16 – 55, 2015, special Topical Issue on Wide-Bandgap Semiconductor Materials.

[206] M. L. Lee, J. K. Sheu, and Y.-R. Shu, "Ultraviolet bandpass $Al_{0.17}Ga_{0.83}N$GaN heterojunction phototransitors with high optical gain and high rejection ratio," *Applied Physics Letters*, vol. 92, no. 5, p. 053506, 2008.

[207] F. Xie, H. Lu, X. Xiu, D. Chen, P. Han, R. Zhang, and Y. Zheng, "Low dark current and internal gain mechanism of GaN MSM photodetectors fabricated on bulk GaN substrate," *Solid-State Electronics*, vol. 57, no. 1, pp. 39 – 42, 2011.

[208] F. Mireles and S. E. Ulloa, "Acceptor binding energies in GaN and AlN," *Phys. Rev. B*, vol. 58, pp. 3879–3887, Aug 1998.

[209] Z. H. Zaidi and P. A. Houston, "Highly Sensitive UV Detection Mechanism in AlGaN/GaN HEMTs," *IEEE Transactions on Electron Devices*, vol. 60, no. 9, pp. 2776–2781, Sep. 2013.

[210] M. T. Hirsch, J. A. Wolk, W. Walukiewicz, and E. E. Haller, "Persistent photoconductivity in n-type GaN," *Applied Physics Letters*, vol. 71, no. 8, pp. 1098–1100, 1997.

[211] M. Shur, B. Gelmont, and M. A. Khan, "Electron mobility in two-dimensional electron gas in AIGaN/GaN heterostructures and in bulk GaN," *Journal of Electronic Materials*, vol. 25, no. 5, pp. 777–785, 1996.

[212] Z. Z. Bandić, P. M. Bridger, E. C. Piquette, and T. C. McGill, "Minority carrier diffusion length and lifetime in GaN," *Applied Physics Letters*, vol. 72, no. 24, pp. 3166–3168, 1998.

[213] K. Wu, L. Rademaker, and J. Zaanen, "Bilayer excitons in two-dimensional nanostructures for greatly enhanced thermoelectric efficiency," *Physical Review Applied*, vol. 2, no. 5, p. 054013, 2014.

[214] K. Hirakawa and H. Sakaki, "Mobility of the two-dimensional electron gas at selectively doped n -type $Al_xGa_{1-x}As$/GaAs heterojunctions with controlled electron concentrations," *Physical Review B*, vol. 33, no. 12, pp. 8291–8303, 1986.

[215] "Thick and thin GaN simulation codes," https://github.com/ananthy/GaNThick, accessed: 2019-02-07.

[216] "Phonon drag simulation codes," https://github.com/ananthy/PhononDrag, accessed: 2019-02-07.